THE ORIGIN OF THE INFRARED EXCESS OF HERBIG STARS

By

ELISHA FRANCES POLOMSKI

A DISSERTATION PRESENTED TO THE GRADUATE SCHOOL
OF THE UNIVERSITY OF FLORIDA IN PARTIAL FULFILLMENT
OF THE REQUIREMENTS FOR THE DEGREE OF
DOCTOR OF PHILOSOPHY

UNIVERSITY OF FLORIDA

2000

Copyright 2000

by

Elisha Frances Polomski

This work is dedicated to Frances Kelly Ross (1906-2000), a remarkable woman. An independant scientist when it was not socially acceptable in the 1930s, a mother, grandmother and friend.

Frances Ross, center, age 22, hanging out with friends in Boston.

ACKNOWLEDGMENTS

The Digitized Sky Survey was produced at the Space Telescope Science Institute under U.S. Government grant NAG W-2166. The images of these surveys are based on photographic data obtained using the Oschin Schmidt Telescope on Palomar Mountain and the UK Schmidt Telescope. The plates were processed into the present compressed digital form with the permission of these institutions.

The "Second Epoch Survey" of the southern sky was made by the Anglo-Australian Observatory (AAO) with the UK Schmidt Telescope. Plates from this survey have been digitized and compressed by the STScI. The digitized images are copyright (c) 1993-9 by the Anglo-Australian Observatory Board, and are distributed herein by agreement. All Rights Reserved. All material not subject to the above copyright provision is copyright (c) 1999 by the Association of Universities for Research in Astronomy, Inc. All Rights Reserved. Produced under Contract No. NAS5-2555 with the National Aeronautics and Space Administration.

This research made use of the LRS database maintained at the University of Calgary, Canada, and the SIMBAD database at Strasbourg, France.

My graduate studies were partially funded by a NASA Graduate Student Research Fellowship. I thank my advisor, Charlie Telesco, and the entire OSCIR team for many fruitful nights at telescopes in far-off lands. I thank Dr. Robert Piña and the Nyquist Sampling Theorem.

I would like to thank all of Central and South America for the cultivation of coffee and cocoa beans, (in which industries I have made great investments) and Karl Haisch and Beth Holmes who helped me imbibe many caffeinated elixirs. I also want

to thank Dr. Lauren Jones, the astronomy graduate students, the staff and faculty of the astronomy department, and the inmates of 405.

Finally, I thank my friend Stéphane Vennes for steadfast encouragement, support, and inspiration during my entire graduate career.

TABLE OF CONTENTS

ACKNOWLEDGMENTS iv

LIST OF TABLES ix

LIST OF FIGURES x

ABSTRACT xiv

CHAPTERS

1 INTRODUCTION 1

- 1.1 Pre-Main-Sequence Evolution 3
- 1.2 Observational Properties 6
- 1.3 Outline of Presentation 12

2 THE IR EXCESS AND DISKS 13

- 2.1 Herbig Ae/Be Spectral Energy Distributions 14
- 2.2 Disk Models 18
- 2.3 Observational Evidence for Ae/Be Disks 22
- 2.4 Problems With the Disk Model 24
- 2.5 Other Models 25

3 THE MID-INFRARED REGIME 29

- 3.1 Radiative Processes and Dust Grains 29
- 3.2 Mid-IR Spectral Features 33
- 3.3 Mid-IR Observing Techniques 35
- 3.4 Mid-IR Instrumentation 41

4 THE SAMPLE AND OBSERVATIONS 47

- 4.1 General Observational Methodology 47
- 4.2 IRTF Observations 48
- 4.3 CTIO Observations 49
- 4.4 Keck Observations 49
- 4.5 Other Observations 50
- 4.6 Calibration 50
- 4.7 Summary of Object Characteristics 51
  - 4.7.1 LkHα 198 and V376 Cas 52
  - 4.7.2 RNO 1 Complex 52

4.7.3 XY Per 53
4.7.4 AB Aur 53
4.7.5 LkHα 25 54
4.7.6 HD 259431 54
4.7.7 HD 100546 54
4.7.8 HD 97048 55
4.7.9 DK Cha 55
4.7.10 KK Oph 56
4.7.11 Juggler Nebula/AFGL 2136 56
4.7.12 V921 Sco 56
4.7.13 MWC 297 57
4.7.14 AS 310 57
4.7.15 BD +40 4124 Complex 57
4.7.16 LkHα 234 58
4.7.17 MWC 1080 58

5 DATA REDUCTION AND ANALYSIS 63

5.1 File Structure 63
5.2 Data Reduction Procedure 64
5.2.1 Airmass Correction 65
5.2.2 Flat Fielding 67
5.2.3 Sky Variations 67
5.3 Image Artifacts 68
5.4 Image Analysis Tools 70
5.4.1 Gaussian Smoothing 70
5.4.2 Histogram Tool 71
5.4.3 Photometry Tools 72
5.4.4 FWHM tool 72

6 MID-IR IMAGES AND PHOTOMETRY 73

6.1 Imaging 73
6.1.1 LkHα 198 and V376 Cas 73
6.1.2 RNO 1 Complex 74
6.1.3 XY Per 75
6.1.4 AB Aur 76
6.1.5 LkHα 25 76
6.1.6 HD 97048 77
6.1.7 HD 100546 77
6.1.8 DK Cha 78
6.1.9 V 921 Sco 79
6.1.10 KK Oph 80
6.1.11 MWC 297 82
6.1.12 Juggler Nebula/AFGL 2136 82
6.1.13 BD +40 4124 Complex 83
6.2 Photometry 85
6.3 Color Corrections 87
6.4 Origin of IR Excess 90
6.5 Mid-IR SEDs 92
6.5.1 XY Per A/B 92
6.5.2 DK Cha 94
6.5.3 V 921 Sco 94
6.5.4 V 1318 Cyg N/S 96

- 6.6 Spectral Indices 98
- 6.7 Embedded Companions 105
- 6.8 Mid-IR Colors and YSO Classes 118

7 COLOR TEMPERATURES AND OPTICAL DEPTHS 124

- 7.1 Color Temperatures of Unresolved Sources 125
- 7.2 Narrow Band Colors 127
- 7.3 Temperature and Optical Depth of Resolved Sources 128
  - 7.3.1 RNO 1C 128
  - 7.3.2 HD 100546 128
  - 7.3.3 V921 Sco 129
  - 7.3.4 MWC 297 132
  - 7.3.5 AFGL 2136 134

8 CORE SOURCES 135

- 8.1 Mid-IR Morphology 135
  - 8.1.1 HD 259431 135
  - 8.1.2 AS 310 136
  - 8.1.3 LkHα 234 138
  - 8.1.4 MWC 1080 140
- 8.2 Photometry 142
- 8.3 Variability 143
- 8.4 Spectral Energy Distributions 145
- 8.5 Color Temperatures and Optical Depths 148
  - 8.5.1 HD 259431 153
  - 8.5.2 AS 310 154
  - 8.5.3 LkHα 234 156
  - 8.5.4 MWC 1080 157
- 8.6 Summary 157

9 SUMMARY AND CONCLUSIONS 160

- 9.1 Suggestions for Future Work 163
  - 9.1.1 Mid-IR Observations 164
  - 9.1.2 SIRTF Observations 164
  - 9.1.3 Millimeter Observations 165

A APPENDIX: IDL CODE 167

- A.1 Photometry Tool 167
- A.2 Color Temperature Code 169

REFERENCES 173

BIOGRAPHICAL SKETCH 185

LIST OF TABLES

3-1 OSCIR Characteristics at Various Telescopes 45

4-1 Observation Log 60
4-2 Ae/Be Star Sample 61
4-3 Calibration Stars 62

6-1 OSCIR and Literature Photometry 86
6-2 Color Corrected N Band Flux Densities 89
6-3 Percentage of Mid-IR Flux External to Primary Star 91
6-4 Narrow Band Photometry 97
6-5 Hillenbrand Spectral Indices 100
6-6 New or Changed Hillenbrand Groups 101
6-7 Embedded Companions 117
6-8 Mid-IR Colors 120

7-1 N/18 μm Temperatures of Unresolved Sources 126

8-1 Multi-aperture Fluxes (Jy) 143
8-2 MWC 1080 Positions and Fluxes (mJy) Keck 1999 144
8-3 Positions and Fluxes (mJy) of Mid-IR Companions 151
8-4 Infrared Fluxes in Literature 152

LIST OF FIGURES

1-1 Theoretical pre-main-sequence tracks in the H-R diagram 6

1-2 United Kingdom Schmidt Sky Survey image of AS 310 7

1-3 MWC 1080 Optical Spectrum 8

1-4 HD 259431 SED 11

2-1 Optical to far-IR SED of LkHα 2334 15

2-2 The SEDs of Group I, II, and III Herbig Ae/Be stars 17

2-3 Geometry of a flat optically thick disk 18

2-4 Optically thick disk models 21

2-5 Geometry of a flared disk 28

3-1 Scattering efficiency, $Q_s(\lambda)$ in the mid-IR 29

3-2 Absorption efficiency, $Q_a(\lambda)$, of astronomical silicate 31

3-3 Mid-IR blackbody curves 31

3-4 Mid-IR spectra of PAH features 35

3-5 Mid-IR absorption due to atmospheric gases. 36

3-6 Atmospheric transmission in the mid-IR 36

3-7 Chopping and nodding technique 38

3-8 Airy Pattern for the IRTF 40

3-9 Relative response of the four survey channels of IRAS. 42

3-10 Transmission of OSCIR broad N filter. 44

3-11 Transmission of OSCIR long wavelength filters. 44

3-12 Transmission of OSCIR narrow-band filters. 44
3-13 OSCIR quantum efficiency 45
3-14 The OSCIR Mid-IR Camera/Spectrometer. 46

4-1 Cohen Model of Alpha Lyra. 51

5-1 Data reduction of chopped, nodded observations 66
5-2 Image of the fully illuminated OSCIR array 68
5-3 The Hammer effect 69
5-4 Channel 8 artifact 70
5-5 Chopping into a mid-IR source 71

6-1 The profile of RNO 1C at 18 μm 75
6-2 The profile of HD 100546 at 11.7 μm 78
6-3 Detail of a broadband, optical (0.2-1.0 μm) coronagraphic image of HD 100546 79
6-4 The KK Oph companion 81
6-5 Deconvolved 18 μm image of KK Oph 82
6-6 The profile of BD +40 4124 at 18 μm. 84
6-7 The SEDs for the A and B components of the XY Per system. 93
6-8 Mid-IR SED of DK Cha. 95
6-9 IRAS spectrum of DK Cha 95
6-10 IRAS spectrum of V 921 Sco 96
6-11 Mid-IR SED of V 921 Sco 96
6-12 Mid-IR SEDs forthe north and south components of the V 1318 Cyg system 98
6-13 Histogram of Hillenbrand spectral indices 99
6-14 Surface brightness of LkHα 198, LkHα 198 mm, V376 Cas, and RNO 1 107

6-15 Same as Figure 6-14 for RNO 1, XY Per, AB Aur, and HD 259431. RNO 1 . . . 109

6-16 Same as Figure 6-15 for LkHα 25, HD 97048, HD 97048 N, and HD 100546 . . . 111

6-17 Same as Figure 6-16 for DK Cha, V921 Sco, KK Oph, and MWC 297 113

6-18 Same as Figure 6-17 for AFGL 2136, AS 310, BD +40 4124, and V 1318 Cyg . . . 115

6-19 Same as Figure 6-18 for LkHα 234 and MWC 1080 . . . 116

6-20 Johnson mid-IR colors for main sequence stars (Johnson 1966). . . . 119

6-21 IRAS colors for main sequence stars . . . 119

6-22 V-N color excess . . . 121

7-1 V 921 Sco 7.9/18 μm color-temperature and optical depth maps . . . 130

7-2 V 921 Sco 9.8/18 μm color-temperature and optical depth maps . . . 131

7-3 V 921 Sco 12.5/18 μm color-temperature and optical depth maps . . 132

7-4 MWC 297 color-temperature and optical depth maps . . . 133

8-1 R band image of AS 310 . . . 137

8-2 N band image of LkHα 234 . . . 138

8-3 LkHα 234 companion . . . 140

8-4 Keck 11.7 μm surface brightness of MWC 1080 . . . 141

8-5 Optical to millimeter SED of HD 259431 . . . 147

8-6 Optical to millimeter SED of AS 310 . . . 148

8-7 Optical to millimeter SED of LkHα 234 . . . 149

8-8 Optical to millimeter SED of MWC 1080 . . . 150

8-9 HD 259431 11.7/18.2 μm color temperature and optical depth maps . 154

8-10 AS 310 7.9/18.2 μm and 9.8/18.2 μm color temperature maps 155

8-11 LkHα 234 9.8/18.2 μm color temperature and optical depth maps . . 156

8-12 MWC 1080 11.7/18.2 μm color temperature and optical depth maps . 158

Abstract of Dissertation Presented to the Graduate School
of the University of Florida in Partial Fulfillment of the
Requirements for the Degree of Doctor of Philosophy

THE ORIGIN OF THE INFRARED EXCESS OF HERBIG STARS

By

Elisha Frances Polomski

December 2000

Chairman: Dr. Charles M. Telesco
Major Department: Astronomy

The recent discoveries of extrasolar planets have spurred investigations of pre-main sequence stars and their environments. Theory suggests that planets form in dusty circumstellar disks around young stars. Many young stars exhibit large excesses of infrared emission that have been attributed to circumstellar disks. In the case of the lower mass stars such as the T Tauri and Vega classes, the association of the IR excess with a disk has been confirmed by direct imaging of disks. However, no disks have been convincingly detected around intermediate mass stars, the Herbig Ae/Be stars. My study involves high spatial resolution multi-wavelength mid-IR imaging of these objects. I show that in many cases the mid-IR emission is not dominated by emission from a circumstellar disk, but arises in other physical phenomena. Many Herbig stars are members of multiple systems and the companions contribute a large portion of the mid-IR emission. In addition some systems exhibit large-scale extended emission from dust shells. Other objects show evidence of tiny dust grains that emit preferentially in the mid-IR. My research shows that mid-IR imaging can directly impact models

of the circumstellar environments of these young stars. No circumstellar disks were detected in my sample. Disks may not be present around these stars, or the disks of Herbig stars may be too close to the central star to be resolved with the telescopes used in this study.

CHAPTER 1
INTRODUCTION

Ae/Be stars were first noted in catalogues that collected early spectral type (O-A) stars with hydrogen emission lines (Merrill & Burwell 1933). Some Ae/Be stars also first appeared in publications by Hubble (1922) who was seeking to understand the difference between spiral nebulae (galaxies) and galactic nebulae (planetary nebulae and star-forming regions). Hubble noted that diffuse galactic nebulae were associated with emission line stars and classified several of these stars, including the now well known Ae/Be star HD 259431, as peculiar B stars. The Mount Wilson Catalogue (MWC) of B and A stars with hydrogen emission lines was compiled by Merrill and Burwell between 1913 and 1951 (Merrill 1913; Merrill & Burwell 1950; Miller & Merrill 1951). The authors noted that these early type emission line stars were associated with clusters and generally located in the galactic plane. However, theories concerning early stellar evolution (Schwarzschild 1958) and the internal structure and nuclear processes of stars (Chandrasekhar 1939) were just emerging and no attempt was yet made to link observational characteristics with the physical processes inherent to these stars. In addition, these early emission line catalogues included a heterogenous mix of objects, some of which, such as η Carinae, actually belonged to a distinctly different and substantially more evolved class of stars than the Ae/Be stars.

The first study to identify the Ae/Be stars as a distinct class of objects was published in 1960 by George Herbig who listed 26 objects of this type (Herbig 1960). Herbig was searching for the higher mass analogs of the solar-mass pre-main-sequence

T Tauri stars. T Tauri stars were first recognized as young stellar objects by Ambartsumian (1947) who noted their association with short-lived massive OB stars in dark clouds. Herbig predicted that the high mass analogs of the T Tauris would possess many similar observational characteristics but would be of an earlier spectral type. He identified the Ae/Be stars using the following criteria: stars were of spectral type A or earlier, exhibited optical emission lines, were located in an obscured region, and illuminated bright nebulosity in their vicinity. Both classes of objects have been found to possess large excesses of infrared emission compared to main sequence stars of the same spectral type. Since Herbig's original study, the list of Ae/Be stars has grown to more than 100 (Thé et al. 1994), and their pre-main-sequence status has become widely accepted.

Like the T Tauri stars, the infrared emission of Herbig stars has been ascribed to thermal emission from dusty circumstellar disks. However, while direct imaging has confirmed the link between the IR excess and disks around T Tauri stars and other somewhat more evolved pre-main-sequence stars (McCaughrean et al. 1996, Jaywardhana et al. 1998), no disks have been conclusively detected around Ae/Be stars and most evidence for their presence is indirect. Because theory suggests that planets form in dusty circumstellar disks around young stars it is important to know whether the IR emission of Ae/Be stars originates in disks or other processes. The recent discoveries of extrasolar planets (Marcy & Butler 2000) have shown that planet formation is not unusual around late type (F-M) stars, but it is unknown whether the environments of Ae/Be stars possess the appropriate physical conditions for planetary formation. The presence or absence of disks around Ae/Be stars has important consequences for the formation of planets and the frequency of planets around stars. In the following thesis, I discuss the evolutionary status of Ae/Be stars and their observational characteristics. I then present new high-resolution observations of their mid-IR emission and discuss the consequences of these observations for the origin of the IR excess and the presence of disks around Ae/Be stars.

1.1 Pre-Main-Sequence Evolution

Pre-main-sequence stars develop within the confines of a cool (T=30 K) giant molecular cloud. A cloud is perturbed from equilibrium and contracts isothermally under the influence of gravitational (Hayashi 1966) and magnetic (Shu et al. 1999) pressures. Central regions of the cloud collapse faster than outer parts, and a hydrostatic core forms (Palla 1993). As infalling material accretes onto this core, it creates a strong initial accretion shock that cools the forming star and inhibits formation of a large stellar radius. Theoretical models suggest that a circumstellar disk is required to transport matter to the stellar surface. The rapidly rotating material from the collapsing molecular cloud must lose angular momentum before it can be directly accreted onto the protostar. Most models suggest that material is first accreted onto a rotating circumstellar disk. Angular momentum can then be transported outward while the material moves inward toward the protostar (Hartmann 1998; Bodenheimer 1995). Evolutionary models with accretion rates of $\dot{M} = 1 \times 10^{-5} M_{\odot}\ yr^{-1}$ agree well with the observed locations of pre main sequence stars in the H-R diagram (Palla & Stahler 1993). Accretion rate and the initial mass of the protostar play important roles in the subsequent evolution of pre-main-sequence stars. For low mass ($M<2.5M_{\odot}$) stars the duration of accretion is much shorter than the gravitational contraction time $t_{KH}=GM^2{}_*/R_*L_{surf}$. Higher mass, Ae/Be stars sustain accretion for most of their pre-main-sequence lifetimes.

The accretion phase of low mass stars includes a period of deuterium burning. Core contraction leads to a temperature rise that ignites deuterium ($T \sim 10^6$ K) (Palla 1999). Luminosity gradients within the contracting object cause the star to become convectively unstable. As the deuterium is transported to the core by convection the core temperature rises and the stellar radius expands; deuterium burning slows the contraction of the star. As the stellar mass grows through accretion, gravity increases and eventually counteracts the growing stellar radius. When accretion ceases, the deuterium supply is exhausted and the outer layers of the star cool. The star's internal luminosity now decreases because it is no longer provided by accretion. The star now contracts quasi-statically and homologously along a nearly vertical Hayashi track. As the core temperature rises due to contraction, convection ceases and a radiative core develops. The effective temperature and luminosity of the star now increase slightly and it moves on an almost horizontal track toward the Zero Age Main Sequence (ZAMS). When temperatures rise to $\sim 1 \times 10^7$ K hydrogen fusion via the CNO bi-cycle begins. Since this reaction is very temperature sensitive, a temperature gradient is established in the core and it once again becomes convective (Bowers and Deeming 1984). Convection halts any further gravitational contraction and the star experiences a slight drop in luminosity because of the energy expended in convection. Finally, the core carbon supply is exhausted and core temperatures rise again and hydrogen fusion begine via the pp chain. Because this reaction can occur over a wider range of temperatures the gradient of temperature and reaction rate is reduced, the core becomes radiative, and enters the ZAMS (Bowers & Deeming 1984; Stahler et al. 1980). This sequence of evolution is believed to be characteristic of the low-mass T Tauri stars.

For successively more massive stars, such as the Herbig Ae/Be stars, the initial period of deuterium burning shortens. The evolutionary tracks of these stars do not include a phase of Hayashi contraction. As shown in Figure 1-1, stars more massive than ~ 2 $M_\odot$ proceed nearly horizontally toward the ZAMS along radiative tracks from the stellar birthline. These stars experience higher accretion rates and evolve more rapidly than low mass stars. For $M_\odot > 2.5$ the core temperature rises during contraction until convection halts at a layer within the star and a radiative barrier forms. This barrier prevents fuel from reaching the core. The core deuterium supply is quickly exhausted and the core contracts because of heat loss. As deuterium piles up at the barrier because of continuing accretion, the temperature rises, shell burning begins, and the stellar radius swells. These stars contract non-homologously; stellar radii expand simultaneously with a contracting core. As the core temperature rises, the radiative core increases in size and the convective layer shrinks toward the surface; this process is called thermal relaxation. After the star is thermally relaxed, gravitational contraction proceeds homologously and stellar luminosity rises. Accretion of material slowly lessens because of outflows and winds, and the star clears away its placental material and appears on the stellar birthline. The star then evolves horizontally toward the ZAMS (Palla 1999). Gravitational contraction leads to an increase in core temperature, hydrogen ignites, and the star moves onto the ZAMS similarly to lower mass stars.

More massive objects (greater than 4 $M_\odot$) have higher internal temperatures, are fully radiative, and do not undergo a phase of thermal relaxation (Palla & Stahler 1993). Fully radiative stars contract more quickly than lower mass stars under the influence of their greater gravity but follow an evolutionary sequence similiar to the lower mass stars during their final contraction and hydrogen ignition phase. At protostellar masses above $8M_\odot$ the duration of accretion exceeds the duration of the contraction phase. Rapid gravitational contraction leads to hydrogen ignition while these stars are still accreting material, and this ignition halts gravitational contraction. These stars are only visible as infrared sources during their pre-main-sequence evolution because they are still veiled by accreting material. High-mass stars first become optically visible after they have already joined the main sequence, and thus the stellar birthline for these objects overlaps the ZAMS (Palla & Stahler 1993).

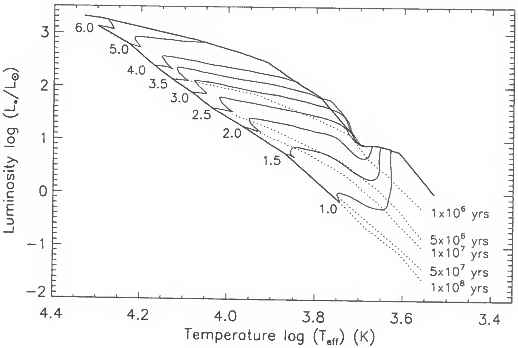

Figure 1-1: Theoretical pre-main-sequence tracks in the H-R diagram. Each track is labeled by the corresponding stellar mass, in units of $M_{\odot}$. Selected isochrones are shown by the dotted lines. For each track, the evolution starts at the birthline (light solid line), and ends at the ZAMS, also indicated (Palla & Stahler 1999).

1.2 Observational Properties

Although Ae/Be stars were first discovered in optical surveys such as the Lick Hα (LkHα) and Mount Wilson Catalogue (MWC) surveys, they have been studied at wavelengths from radio to x-ray. The unifying characteristic of these stars at all wavelengths is that they exhibit phenomena associated with the presence of circumstellar material.

In the optical (λ 3000-9000 Å) these objects show heavily reddened spectra, usually with abundant emission lines of hydrogen, helium, and iron (Figure 1-3), and some photospheric absorption lines. However, some objects lack the photospheric absorption lines used as indicators of spectral type because of strong emission from

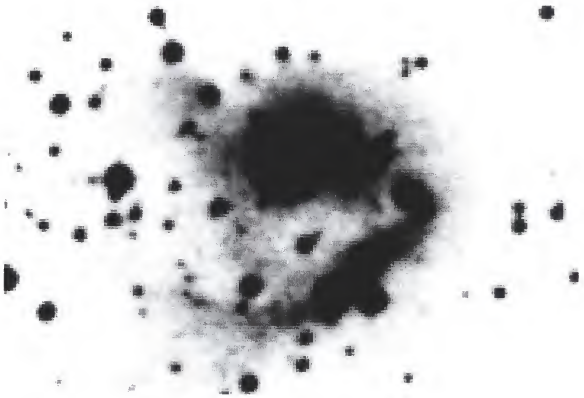

Figure 1-2: United Kingdom Schmidt Sky Survey image of AS 310, 3′×2′ field, $\lambda_{\rm eff}$=6500Å

surrounding nebulosity. Optical observations also indicate variability in spectral profiles, velocity widths, and photometry, of up to several magnitudes (Finkenzeller & Mundt 1984; Shevchenko et al. 1993; Herbst & Shevchenko 1999). Optical images of Ae/Be star-forming regions from the Digitized Sky Survey show bright emission and reflection nebulae as well as dark obscuring dust clouds (Figure 1-2).

The optical emission lines are produced in hot extended chromospheres and stellar winds (Finkenzeller & Mundt 1984). Many objects exhibit P-Cygni profiles (for example Figure 1-3) in their emission lines. These profiles are produced by a spherical stellar wind and are characterized by a blue-shifted absorption feature with a broad emission feature at its red edge. The stellar wind directly between the observer and the star produces the absorption line with a blue shift corresponding to the wind velocity. Wind along other lines of sight produces the broad emission

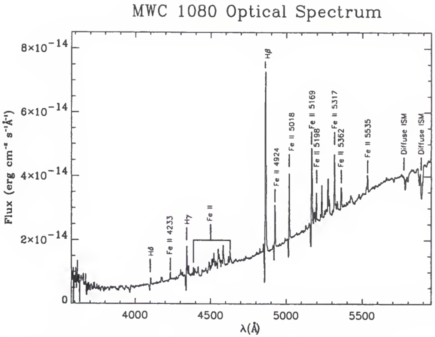

Figure 1-3: MWC 1080 optical spectrum from MDM observatory showing emission features, some with P Cygni profiles.

feature. An excellent discussion of the geometric considerations and physics of P Cygni lines can be found in Emerson (1996). Variability in the spectral features and photometry has been attributed to variable winds, accretion events, and obscuration from orbiting dust clouds (Herbst & Shevchenko 1999; de Winter et al. 1999).

Few objects have been observed in the ultraviolet (λ1000-3000) because of heavy extinction and limited access to this regime from orbiting observatories. Spectra from the International Ultraviolet Explorer (IUE) show narrow circumstellar absorption lines, broad photospheric absorption, high excitation emission lines, and P Cygni features (Hu et al. 1991; Grady et al. 1996b). The ultraviolet emission is believed to be produced in a hot (15,000 K) dense chromosphere that extends to a few stellar radii (Catala & Bertout 1990; Catala 1988). Some objects show a UV excess that is attributed to an accretion disk (Blondel & Tjin A Djie 1994). As in the optical, variability is common with some spectral variability and UV color changes attributed to variable obscuration and accretion events (Grady et al. 1996a; Grady et al. 1995).

High energy x-ray (0.2 to 10 Kev) surveys of pre-main-sequence stars have been conducted with Einstein, Roentgen satellite (ROSAT), and the Advanced Satellite for Cosmology and Astrophysics (ASCA) observatories. Late type (F-M) main sequence stars have magnetic dynamos that drive convective envelopes and a hot corona that produces x-ray emission. More luminous main sequence stars, the B-F classes, lack x-ray emission entirely because they do not possess magnetic dynamos and coronae. The earliest spectral types, O-B, possess strong stellar winds and their x-ray emission is believed to be produced by wind shock instabilities. Analagous mechanisms are believed to apply to pre-main-sequence stars and thus, Ae/Be stars were not expected to be x-ray sources since they lack convective atmospheres, magnetic dynamos and thus coronae. However, in a recent ROSAT survey of 21 Ae/Be stars, 11 were detected (Zinnecker & Preibisch 1994) and the Einstein and ASCA satellites have detected an additional 9 sources (Hamaguchi et al. 2000; Damiani et al. 1994). There is considerable disagreement concerning the origin of this emission. Some authors suggest that an unseen late type T Tauri companion may be producing the x-ray emission. Although many Ae/Be stars do possess binary companions, current x-ray instrumentation does not have sufficient spatial resolution to determine which object is the source of the emission. In addition, some researchers argue that the spectral shape of the emission and the large x-ray luminosity argue against a T Tauri origin (Zinnecker & Preibisch 1994). Correlation between the x-ray and bolometric luminosities of Ae/Be stars has prompted other authors to favor a shock heating wind model for the origin (Damiani et al. 1994; Zinnecker & Preibisch 1994). P-Cygni line profiles have indicated that Ae/Be stars have wind velocities up to 500 km/s (Finkenzeller & Mundt 1984) and therefore support this model. Finally, a few authors propose that Ae/Be stars do possess magnetic dynamos that are produced by a shearing effect from the young stars intially rapid rotation. The magnetic flux is then dissipated at the stellar surface and heats coronal gasses producing the observed x-ray emission (Tout & Pringle 1995; Skinner & Yamauchi 1996). Observations with the new Chandra x-ray telescope which can achieve spatial resolutions of less than 1″ and is 100 times more sensitive than Einstein may help resolve some of these questions.

The infrared to radio (1 μm to 6 cm) emission from Ae/Be stars predominantly arises in thermal processes. In the IR and millimeter, short wavelength ultraviolet photons are absorbed by dust grains and gas molecules in the young star's environment. Vibrational transitions in dust grains and rotational and vibrational transitions in molecules arise and the photon is re-emitted at longer wavelengths, i.e. in the infrared and millimeter. Such emission is characterized by dust temperatures ranging from 1500 K (in the near-IR) to 10 K (in the millimeter). Because grains are usually assumed to be in thermal equilibrium, grain temperature is proportional to distance from the star. Millimeter continuum emission is usually assumed to be optically thin, and with appropriate assumptions concerning grain characteristics, dust masses can be derived. Ae/Be stars are strong sources of infrared emission and often appear brighter in the infrared than at optical wavelengths. Millimeter emission from cool molecular gases such as CO, CS, and HCN is also observed around Ae/Be stars. In some cases, maps of molecular emission and spectral observations have indicated large-scale (0.1 pc) outflows (Mitchell & Matthews 1994; Staude & Elsässer 1993).

Ae/Be stars usually exhibit large excesses of infrared and millimeter emission over that observed from main sequence stars of similar spectral types (Figure 1-4), indicating the presence of large masses of circumstellar material. Mass estimates from millimeter observations range between $\sim 10^{-3}$ and $\sim$10 $M_\odot$ (Waters & Waelkens 1998). Many authors have assumed that this emission arises in circumstellar disks and have modeled the properties of the disks accordingly. However, as I will show in Chapter VI, other phenomena can account for a large percentage of the thermal emission and may call for a reexamination of current disk models.

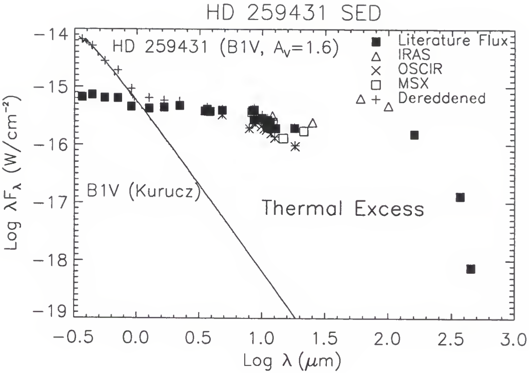

Figure 1-4: HD 259431 SED. Data compiled from the literature, OSCIR observations, and observations by the IRAS and MSX satellites as indicated by symbols. Data were also corrected for interstellar extinction and plotted as crosses. Solid line is a Kurucz model for a B1V main sequence star. HD 259431 exhibits a large excess flux in the IR and millimeter compared to a main sequence star.

Radio emission from Ae/Be stars is produced by thermal processes such as cool blackbody emission from dust, stellar winds, shocks, and H II regions (Skinner et al. 1993; Altenhoff et al. 1994) but includes collimated water maser emission as well. Maser emission is produced when molecules are excited to higher energy levels resulting in a population inversion; more molecules exist in the higher energy state than in a ground state. Interaction with a photon then stimulates the emission of a maser photon. In the case of water maser emission, pumping energy is provided by shocks associated with high velocity outflows (Elitzur et al. 1989). Water masers are detected among the more embedded and younger Ae/Be stars and are associated with molecular outflows and possibly circumstellar disks (Slysh et al. 1999; Rodriguez et al. 1987; Palla & Prusti 1993).

1.3 Outline of Presentation

As discussed above, much of the emission from Ae/Be stars originates in thermal processes or phenomena due to circumstellar material. In particular, one of the defining characteristics of this class of stars is their thermal excess in the infrared. I focus on the study of the mid-IR (4 to 20 μm) excess and the specific processes and physical structures in which it originates. In Chapter II, I briefly discuss the properties of the infrared excess and the various theories of its origin in Ae/Be star environments. In Chapter III, I focus on characteristics of the mid-IR regime in particular, the physical processes operating in this regime, and the specialized instrumentation used for this study. Chapter IV presents the sample, their classification, and information concerning the observations. Chapter V discusses data reduction and image analysis techniques used for this research. In Chapter VI, I show the overall mid-IR properties of my sample derived from my observations, their distribution in V-N, N-18 colors, the variation of their SED slope with Herbig star class, and the percentage of the mid-IR excess originating in their circumstellar regions. In Chapter VII I examine the mid-IR color temperatures and emission optical depths of these objects. Finally, Chapter VIII discusses the detailed properties of a subsample of four objects for which I have the most extensive data. A summary of the presentation and conclusions is in Chapter 9.

CHAPTER 2
THE IR EXCESS AND DISKS

The IR excesses of pre-main-sequence stars were first discovered by Mendoza (1966). In low-mass pre-main-sequence stars such as T Tauri and Vega class stars, an infrared excess is firmly linked with the presence of a circumstellar disk. Observations made with the IRAS satellite were the first to indicate that the well known Vega and β Pic systems possessed IR excesses. Later high-resolution imaging revealed a disk of circumstellar material around β Pic (Aumann et al. 1984; Smith & Terrile 1984; Mouillet et al. 1997). More recently, ground-based mid-IR observations of the star HR 4796, a Vega class star, clearly revealed the presence of a dust disk about 100 AU in extent (Jayawardhana et al. 1998) and HST observations of low-mass stars in the Orion star-forming region showed disks extending as much as 500 AU that are coincident with infrared excess sources (McCaughrean, & O'Dell 1996).

By analogy, many researchers have associated the IR excesses of Ae/Be stars with circumstellar disks. However, Herbig Ae/Be stars present a more complicated problem than the late type low-mass pre-main-sequence stars. Early spectral type stars such as the Ae/Be stars are less common than later types and thus relatively few objects are located at close distances. The problem then becomes one of spatially resolving disk structure. If we assume that an Ae/Be disk extends the same radial distance as the disk of a low mass star, ($\sim$500 AU) then the disk would span only $1''$ at the typical distance of an Ae/Be star (500 pc). Until recently most infrared instruments were unable to resolve structure of such scale. In contrast, some low-mass star-forming regions are at distances of $\sim$100 pc or less and such a disk would span $5''$. However, since Ae/Be stars are intrinsically much more luminous than T

Tauri stars, they can heat dust out to much greater radii, and may possess larger disks than the less luminous low-mass pre-main-sequence stars.

Ae/Be stars generally have larger IR excesses and larger millimeter fluxes than the T Tauri stars (Lada & Adams 1992; Hillenbrand et al. 1992), implying that they are embedded in more circumstellar material. For example, in the Lada & Adams (1992) sample, most T Tauri stars cluster around a J-H color of ~1, while Ae/Be stars are scattered across a range extending to J-H=2.2. The greater intrinsic luminosity of Ae/Be stars can also excite energetic emission processes in their star-forming regions that can veil the emission from a disk at near-IR wavelengths.

2.1 Herbig Ae/Be Spectral Energy Distributions

Despite these problems, many researchers have fit circumstellar disk models to the infrared SEDs of Ae/Be stars. Because early type stars emit little infrared emission, it is clear from these SEDs that a significant amount of material surrounds Ae/Be stars. SEDs corrected for interstellar extinction appear to fit stellar models well at optical wavelengths and diverge from main-sequence stellar models at wavelengths of ~1μm (Figure 2-1). Ae/Be SEDs often exhibit excess emission into the millimeter and radio regime. In the near-IR (1-3 μm) many Ae/Be SEDs show a dip and subsequent emission peak. Models of this feature include emission from transiently heated grains in a dust nebula (Hartmann et al. 1993), and a hole in a circumstellar disk (Hillenbrand et al. 1992). Transiently heated grains, such as polycyclic aromatic hydrocarbon grains (PAHs), are not in thermal equilibrium and have a known emission feature at 3.29 μm. These grains are heated by ultraviolet photons to temperatures of ~1000 K and then re-emit near infrared continuum and line emission as they cool. This feature is not usually observed in T Tauri SEDs because it requires a high-luminosity star to produce a large population of ultraviolet photons. A circumstellar disk hole is created when dust close to the star is destroyed

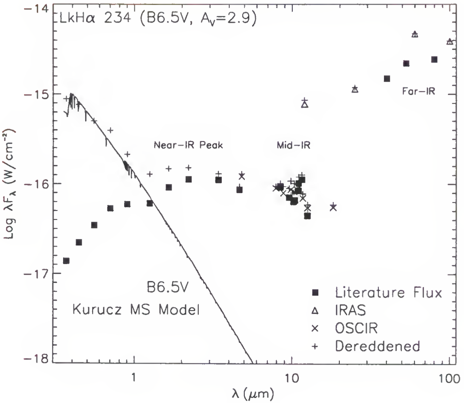

Figure 2-1: Optical to far-IR SED of LkHα 234. Data points from the literature, OSCIR, and the IRAS satellite are indicated by symbols shown in the key. Points corrected for interstellar extinction are indicated by crosses. Solid line indicates Kurucz main-sequence model of B6.5 star

by the stellar radiation at temperatures of $\sim$ 2000 K. Hillenbrand et al. propose that a disk will exhibit a deficit of radiation inside the dust evaporation radius that is seen as a dip in the SED at short wavelengths (λ <3 μm). The SED then rises to a local peak because of emission produced by disk accretion. This model is controversial and several authors have commented that the proposed accretion rates are unrealistic and that hot gas within disk holes would emit significant infrared radiation (Hartmann et al. 1993).

Mid-IR (4 to 20 μm) emission has been attributed to dust within a disk. The mid-IR portion of many Ae/Be SEDs have been successfully fit with disk models having slopes of $F_\lambda \propto \lambda^{-7/3}$. I discuss the properties of these models in detail in Section 2.2.

In the far-IR (60 to 200 μm) to millimeter regime many Ae/Be SEDs exhibit a broad maximum. Various emission mechanisms such as a cold dust envelope, outer disk emission, and deeply embedded companions have been suggested to explain this feature. Most observations in this regime are from the Infrared Astronomical Satellite (IRAS) which could not spatially resolve the source of this emission. In a few cases, Kuiper Airborne Observatory (KAO) observations resolve the emission and show that it originates in both embedded companions and dust envelopes (Di Francesco et al. 1994). High spatial resolution far-IR observations with SIRTF may finally be able to disentangle the components of this emission.

Based on the slope of the IR excess, Lada (1987) first proposed a classification system for pre-main-sequence stars. He divided the stars into three groups depending on whether the SEDs at wavelengths > 2 μm were rising (Class I), flat or decreasing (Class II), or showed no IR excess (Class III). Hillenbrand et al. (1992) built on this classification system and proposed a similar system for Ae/Be stars. Both classification systems are currently used for Ae/Be stars, which often results in confusion because the numerical sequence in the Hillenbrand scheme is different than in the Lada scheme. In the Hillenbrand et al. system, Ae/Be stars whose SEDs at $\lambda \gtrsim 2.2$ μm have slopes similar to those expected from a circumstellar disk ($F_\lambda \sim \lambda^{-7/3}$) are classified as Group I objects. These objects are equivalent to Lada Class II objects and exhibit falling SED slopes between L (3.5 μm) and N (10.6 μm). Group II (Lada Class I) objects have SEDs that are flat or rising toward the far-IR and exhibit flat or rising slopes between L and N. Group II SEDs are believed to originate in systems involving an envelope of dust as well as a disk. Group III (Lada Class III) objects have small IR excesses and SEDs that can be modeled by free-free emission from a wind or a gaseous disk (Figure 2-2). Hillenbrand et al. have defined a characteristic

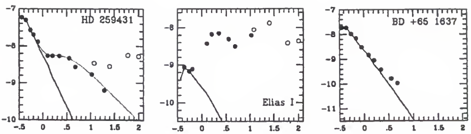

Figure 2-2: The SEDs of Group I, II, and III Herbig Ae/Be stars (Hillenbrand et al. 1992). Kurucz models of main sequence stars are plotted as solid lines. For HD 259431 an optically thick, geometrically thin disk model is also shown as a fainter dotted line.

index for Ae/Be SEDs; $\alpha = \log \frac{\lambda_L F_{\lambda_L}}{\lambda_N F_{\lambda_N}}$. The expected index for a disk is $\alpha \sim 0.64$. Group II objects have smaller indices, and Group III objects whose SEDs are of the form $\lambda F_\lambda \sim \lambda^{-3}$ are expected to have indices ~1.44. A plot of the frequency distribution of the α index for their sample of 47 objects shows that Group I objects that are expected to have circumstellar disks, cluster around $\alpha \sim 0.64$ (Hillenbrand et al. 1992).

Both Lada and Hillenbrand et al. propose an evolutionary scheme within this classification system. The IR excess of pre-main-sequence stars is believed to diminish as a young star disperses its circumstellar material through mass-loss phenomena such as stellar winds and outflows. In addition, some material may coalesce into larger bodies such as protoplanets (Malfait et al. 1998). Objects with the largest IR excesses, and therefore the most circumstellar material, are assumed to be the youngest; and objects with the smallest IR excesses tend to have the least circumstellar material and are the oldest. The evolutionary sequence shows a progressive decrease in the IR excess and the amount of circumstellar material from Group II → Group I → Group III.

There is some evidence that the IR excess evolves differently in early spectral type and late spectral type Ae/Be stars. Both Hillenbrand et al. (1992) and Fuente et al. (1998) note that Group II objects are predominantly the later type (B5-A5) Herbig stars, while Group I objects are dominated by early (B0-B5) spectral types. Fuente et al. (1998) conducted a survey of Herbig Ae/Be stars at millimeter wavelengths and found a correlation with evolutionary state, the amount of circumstellar material, and spectral type. They suggest a bimodal evolution where early-type stars evolve from Group I to Group III on their way to the main sequence, while late-type stars evolve from Group II to Group I.

2.2 Disk Models

The key feature of the IR excess is that it implies the presence of a circumstellar disk. Disk models used for T Tauri stars have been successfully fit to many Ae/Be stars SEDs. The simplest disk models assume a flat disk composed of grains in thermal equilibrium. The disk is considered to be optically thick at infrared wavelengths and absorbs short wavelength stellar radiation and remits in the infrared.

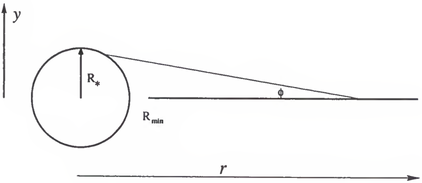

Figure 2-3: Geometry of a flat optically thick disk with a central hole of radius R_{min}. X axis is perpendicular to the plane of the paper, R_* indicates stellar radius, and ϕ is the angle between the disk plane and the stellar surface.

An excellent discussion of the simple blackbody disk model appears in Beckwith (1999). In this model the stellar radiation absorbed by a point at radius r in the disk is given by integrating over the stellar surface seen by the disk (Figure 2-3).

Stellar radiation is approximated by a blackbody Planck function and the disk radius is assumed to be large so that the stellar diameter subtends a small angle (ϕ). Assuming the small angle approximation such that sin$\phi \approx \left(\frac{y}{r}\right)$ the absorbed flux as a function of r is:

$$F_{ab}(r) \approx \frac{1}{r^2}\int_0^{R_*} 2\,sin\phi \int_0^{\sqrt{R_*^2-y^2}} \sigma T_*^4\,dx\,dy \tag{2-1}$$

$$\approx \frac{2}{3}\left(\frac{R_*}{r}\right)^3 \sigma T_*^4 \tag{2-2}$$

Where F_{ab}(r) is the absorbed flux as a function of radius in the disk, R_* is stellar radius, T_* is stellar temperature, and σ is the Stefan-Boltzmann constant.

Assuming thermal equilibrium, the disk radiates like a blackbody and the disk temperature profile as function of distance, r, from the star may be solved by equating the absorbed flux F_{ab}(r) to the radiated flux F_{rad}(r):

$$\frac{2}{3}\left(\frac{R_*}{r}\right)^3 \sigma T_*^4 = \sigma T^4(r) \tag{2-3}$$

$$\text{where } F_{rad} = \sigma T^4(r) \tag{2-4}$$

$$T(r) \approx \left(\frac{2}{3}\right)^{1/4} T_* \left(\frac{r}{R_*}\right)^{-3/4} \tag{2-5}$$

Finally, the observed spectral energy distribution of the simple thin disk may be solved by integrating the disk Planck function over inner and outer radii assuming a distance for the star, D; an inclination angle θ for the disk; and the temperature profile as derived above.

$$B_\nu = \frac{2h\nu^3}{c^2}\frac{1}{e^{\frac{h\nu}{kT(r)}} - 1} \tag{2-6}$$

$$F_\nu = \frac{1}{D^2}\int_{R_{in}}^{R_{out}} \cos\theta\, B_\nu(T(r))\, 2\pi r\, dr \tag{2-7}$$

$$= \frac{1}{D^2}\frac{4\pi h\nu^3}{c^2}\left(\frac{kT_o}{h\nu}\right)^{8/3} R_{in}^2 \cos\theta \int_{x_{min}}^{x_{max}} \frac{x\,dx}{\exp(x^{3/4})-1} \tag{2-8}$$

$$T_o \equiv T(R_{min}) \tag{2-9}$$

Where ν is frequency, c is the speed of light, k is the Boltzmann constant, h is the Planck constant, B_ν is the Planck function, R_{out} and R_{in} are the outer and inner disk radii respectively. The function is evaluated at R_{out} and R_{in} which correspond to x_{max} and x_{min} after a change of variables.

$$x_{min} \equiv \left(\frac{h\nu}{kT(R_{in})}\right)^{\frac{4}{3}} \tag{2-10}$$

$$x_{max} \equiv \left(\frac{h\nu}{kT(R_{out})}\right)^{\frac{4}{3}} \tag{2-11}$$

As mentioned previously Ae/Be disk models usually require an inner hole at the dust sublimation radius in order to account for the near-IR dip in the observed SED. In Figure 2-4 I show several SEDs calculated from disk models with a range of inner holes heated by a B0 star. An additional modification to disk models involves adding realistic grain absorption and emission efficiencies. Most models assume small ($\sim 0.01\,\mu$m) grains of astronomical silicate such that the emissivity, $Q_{em}(\lambda)$, depends on the optical properties of the grain as described by Mie theory. Grain optical properties as a function of wavelength and grain size were determined by Draine & Lee (1984). However, young star-forming regions and disks are likely regions of grain growth; grain radii are probably larger than 0.01 μm, and an emissivity of $Q_{em}(\lambda) \propto \frac{1}{\lambda}$ may be more appropriate (Lynch & Mazuk 2000; Gorti & Bhatt 1993).

Some Ae/Be stars have IR excesses that are too large to be explained by passive disks alone and models of these objects include the impact of accretion on the disk SED (Hillenbrand et al. 1992; Hartmann et al. 1993; Di Francesco et al. 1994; Lada & Adams 1992). In an excellent overview of the subject, Kenyon (1999) describes how, during accretion, material from the disk is transported inward

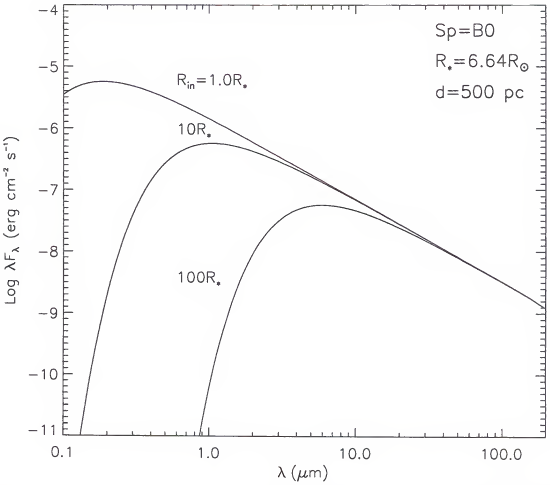

Figure 2-4: Optically thick disk models for a B0 illuminating star, with inner holes of radii 1, 10, and 100 R_*. Inclination angle, θ is assumed to be 0, i.e. face-on viewing and the system distance is 500 pc.

toward the star. Frictional forces created during the mass flow heat the disk. As the material approaches the star it may encounter magnetic field lines that channel it onto the the stellar surface where it releases gravitational potential energy. Accretion theory involves the estimation of viscosity forces and their interaction with angular momentum transfer between disk particles, which is not fully understood at present. In the well known α-disk model, Shakura & Sunyaev (1973) have calculated the temperature profile of the simple geometrically thin, steady state, optically thick accretion disk with dust particles in Keplerian orbits. They find that the accretion disk temperature profile has the same spectral shape as that of a passive non-accreting disk; $T_{acc} \propto r^{-3/4}$. Thus, adding accretion luminosity to the simple disk model raises the flux level, but does not change the shape of the IR SED. The rate of accretion ($\dot{M}$) can be estimated by comparing the observed IR excess to that expected from a passive disk. It then becomes crucial to understand the physical processes producing the IR excess and what portion of it pertains to the disk or other phenomena. I shall discuss below some of the problems with disk models of the IR excess and how other models may be more realistic explanations of the observations.

2.3 Observational Evidence for Ae/Be Disks

Unlike the lower mass stars most evidence for disks around Ae/Be stars is indirect. Many researchers have searched for the signatures of disks around Ae/Be stars by studying spectral features that are believed to be linked to disk phenomena in the lower mass T Tauri stars. For example, many T Tauri stars exhibit blue shifted optical forbidden lines which are believed to be produced by a spherical wind. The absence of red shifted lines has been interpreted as evidence for a disk which is occulting the receding component of the wind (Appenzeller et al. 1984). Corcoran & Ray (1997) have searched for this feature in a sample of 56 Ae/Be stars and have found asymmetric blue shifted lines in half of their sample. However, to illustrate the heterogeneity of the Herbig stars as a class, a previous study by Böhm & Catala (1994) of 33 objects found only one object with blue shifted emission. In addition, four stars in their sample which overlap with Corcoran & Ray's sample show variability in the emission feature which resulted in the absence of any blue shift at the time of the Böhm & Catala observations. Corcoran & Ray also find a correlation with the velocity structure of the lines and the Hillenbrand classes. High-velocity blue shifted forbidden lines are only found in Group II objects, while low-velocity, and unshifted forbidden lines were found in Group I objects.

Other authors have suggested that the large IR excesses and millimeter fluxes of Ae/Be stars imply large masses of circumstellar material which must be aligned in disk-like structures or it would completely occult the star at optical wavelengths (Lada & Adams 1992; Hillenbrand et al. 1992; Mannings & Sargent 2000). Some Ae/Be stars exhibit high polarization in the infrared due to scattering of stellar radiation by dust grains. Maps of polarizations vectors have shown a centro-symmetric pattern which has been modeled as scattering by dust grains within a flattened disk structure (Bastien & Ménard 1990). The presence of an infrared silicate absorption feature in some Ae/Be stars can also imply a disk. Silicate absorption can be produced when large column depths of grains are veiling the central star as might occur if the star were viewed through an edge-on disk of dust (Boss & York 1996; Gürtler et al. 1999).

Finally, millimeter wavelength observations which trace emission from cold molecular gases also provide supporting evidence for disks around Ae/Be stars. Velocity-resolved maps of the gas around several objects, notably, LkHα 234, show large-scale collimated outflows (Mitchell & Mathews 1994). Disks are inferred as the geometric structures needed to collimate these outflows (Bachiller 1996; Sargent 1994). Some of the most direct evidence for disks comes from high-spatial-resolution millimeter maps of Ae/Be stars. For a few of the closest objects, such as MWC 480, and AB Aur, maps of CO emission have resolved blue and red shifted gas in Keplerian rotation around the star (Mannings, Koerner, & Sargent 1997; Mannings & Sargent 1997). This technique requires resolutions of $1''$ or less which is currently only obtainable at a few observatories such as the Owens Valley Radio Observatory and the Institut de RadioAstronomie Millimétrique (OVRO, and IRAM); most objects studied so far have been the nearby ($\sim$ 100 pc), later type, less embedded members of the Herbig star class. The new millimeter array being constructed on Mauna Kea, the SubMillimeter Array (SMA) (Wilner 1999), will achieve sub-arcsecond resolutions enabling this technique to be applied to more distant objects.

2.4 Problems With the Disk Model

Several inconsistencies with the simple disk model of the IR excess have called into question its validity. This model has consistently underestimated the far-IR flux; Hillenbrand et al. (1992) give this regime less weight when fitting disk models to Herbig star SEDs. Most far-IR observations were obtained with the IRAS observatory, which had a pixel scale of $\sim 2'$ at 60 μm. Thus, the large beam sizes may be contaminated by emission from sources other than the circumstellar environment. However, when higher resolution observations from the KAO are obtained, many objects do not exhibit the slope expected from a circumstellar disk (Evans & Di Francesco 1995). An analogous problem has long been recognized in T Tauri SED modeling (Kenyon & Hartman 1987). Even worse, KAO observations indicate that the far-IR emission of *both* Group I and Group II objects may originate in large-scale envelopes rather than disks (Di Francesco et al. 1994)

Even ground-based infrared observations have beam sizes on the order of $\sim 10''$ and, when converted to radial distances from the star in AU, they encompass regions far larger than the regime in which a disk might exist. In a study of Ae/Be star SEDs Lorenzetti et al. (1994) compiled a histogram of SED indices for a similar sample to that studied by Hillenbrand et al. (1992). They find that most Group I objects have slopes that are flatter than expected from disk models and exhibit more 3 to 20 μm emission that would be expected for either a passive or accreting disk. They suggest that alternate models for the geometry of the emission, such as a spherical distribution of dust can fit the observations just as well as disk models.

Finally, one common objection to the simple disk model is that it predicts accretion rates for many Ae/Be stars that are not realistic. Several authors have shown that the accretion rates cited by Hillenbrand et al. (1992) are too large and that excess emission should be observed in the ultraviolet (Hartmann et al. 1993; Natta et al. 1993a). In addition, this model requires that the disk hole region be optically thin, but the high accretion rates proposed by Hillenbrand et al. would cause this region to become optically thick. Magnetic fields have been suggested as a mechanism for directing the accretion stream across the disk inner hole, but no observational evidence for the large fields required has yet been found (Hartmann et al. 1993).

As I shall show in a later chapter, most ground-based observations overestimate the IR excess of Ae/Be star systems and in many cases the mid-IR emission is not dominated by disk emission.

2.5 Other Models

Circumstellar disks are not the only possible mechanism that may explain the large IR excesses of Ae/Be stars. Several authors have suggested a composite model involving both a dusty envelope and a disk (Di Francesco et al. 1994; Berrilli et al. 1992). Natta et al. (1992; 1993a) have presented observational evidence that the far-IR fluxes of Ae/Be stars originate in a disk/envelope combination. In their model, the disk passively reprocesses stellar radiation, which then heats an external dust envelope producing the far-IR flux. They suggest that a dust envelope alone can fit the far-IR emission but cannot reproduce the observed fluxes in the mid-IR. Calvet et al. (1994) also show radiative transfer calculations of a disk/envelope model in which a rotating envelope is accreted onto an interior disk. They find that these models can successfully reproduce the mid to far-IR excesses of objects with flat SEDs.

However, other authors are able to model the same objects without the need for a disk. Prior envelope models utilized dust grain properties characteristic of the interstellar medium. These grains are small (0.01 μm) and have absorption efficiencies $\propto \lambda^{-2}$ at long wavelengths. However, there is evidence that the grains in star-forming regions are larger than those in the interstellar medium and have absorption efficiencies more like λ^{-1} (Gorti & Bhatt 1993; Mannings & Emerson

1994; Weintraub, Sandell, & Duncan 1991). Pezzuto et al. (1997) show that envelope models using larger grains, and a correspondingly lower dust absorption coefficient, can successfully fit the entire optical to millimeter range of Herbig star SEDs, as well as reproduce the observed total visual extinction (A_v). Henning et al. (1998) have also shown that a spherical envelope model can fit observations if it utilizes larger grains.

Emission from transiently heated grains, such as very small grains (VSGs) and polycyclic aromatic hydrocarbons (PAHs), is becoming recognized as an important component of Ae/Be star environments. These grains can be as small as 50 atoms, and undergo thermal spiking from ultraviolet photons in Ae/Be environments. Since they can emit infrared radiation independent of their distance from the star, they can produce more infrared flux than larger classical grains in thermodynamic equilibrium. Transiently heated grains have several known emission features in the near and mid-IR, and can contribute to the IR excess (Brooke et al. 1993; Natta et al. 1992; Hartmann et al. 1993). In particular, Brooke et al. (1993) have conducted observations of the 3 μm feature in 24 Ae/Be stars and have detected extended emission around six objects. In addition they find that these grains can contribute as much as 60% of the far-IR luminosity. Prusti, Natta, & Palla (1994) have also found extended emission from transiently heated grains, in the mid-IR, around three Herbig stars and suggest that for some objects the emission is dominated by PAHs and VSGs. Natta et al. (1993b) have modeled the possible contributions of VSGs and PAHs to the infrared SEDs of Ae/Be stars. They find that although they cannot account for all of the mid-IR excess, they could diminish the need for high accretion rates in some disk models.

Hamann & Persson (1992) and Hartmann et al. (1993) have suggested that some of the near-IR excess might be due to embedded binary companions. Recently, several infrared surveys of Ae/Be stars have focused on the search for companions to the Ae/Be stars and their influence on the SED. Li et al. (1994) discovered many new companions to Ae/Be stars, but found that near-IR fluxes are little affected by companions. Pirzkal et al. (1997) conducted a high spatial resolution search for close bright companions at 2.2 μm. As in the Li survey, they find that with the possible exception of three objects, infrared companions make little contribution to the near-IR excess. However, mid-IR observations are beginning to show that embedded companion stars can contribute a large percentage of the total mid-IR flux. The mid-IR companion of LkHα 198 is responsible for ~30% of the total mid-IR emission at 12 μm (Lagage et al. 1993); a close companion of LkHα 234 dominates the SED at wavelengths longer than 10 μm (Cabrit et al. 1997; Polomski et al. 2000); and, as I shall show from my own observations, companions of MWC 1080 and V1318 Cyg can greatly influence the slope of the SED.

Finally, more realistic models of disks may provide a better fit to observations. A flared disk model was proposed by Hartmann et al. (1993) to explain the flat SEDs of T Tauri stars. In this model the disk scale height, H(r), increases with radial distance (Figure 2-5). A disk will naturally tend to flare if it is in vertical hydrostatic equilibrium. In outer regions of the disk gravitational forces are too weak to confine the dust to a plane, and thermal motions will cause it to expand in a flared shape (Beckwith 1999).

Hartmann et al. (1993) have shown that for an internal temperature distribution of $T \approx R^{-3/4}$ the disk scale height increases as $H(r) = H_0(r/R_*)^{9/8}$. An optically thick disk with a flared profile intercepts a larger fraction of the stellar radiation and will exhibit a flatter temperature profile and a larger IR excess than a simple flat disk. The observed temperature profile of the disk depends upon the specifics of the star temperature and the magnitude of the flaring, but for a T Tauri star, with modest flaring, $T \propto R^{-3/5}$, and the SED is of the form $\lambda F_\lambda \propto \lambda^{-2/3}$ (Hartmann et al.

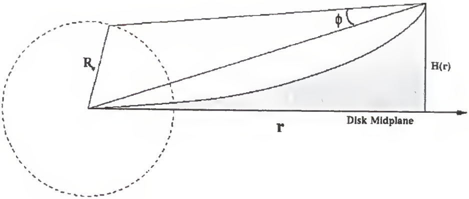

Figure 2-5: Geometry of a flared disk. Dotted circle represents stellar surface with radius R_*, shaded area represents the disk. Disk scale height is H(r), ϕ is the angle between a point on the disk surface and incident stellar radiation.

1993). Building on Hartmann et al.'s results, Chiang & Goldreich (1997) have incorporated radiative transfer calculations of flared disks with optically thin outer layers and optically thick interiors. They find that their models can be adjusted to fit most observed disk SEDs. The flared disk model has some direct observational support; HST images of T Tauri silhouette disks in the Orion Nebula do show flared shapes (McCaughrean, M. & O'Dell 1996). As I shall show in this thesis, while these new disk models may present more realistic representations of the physical environments of Herbig stars, mid-IR imaging shows that other processes may still contribute to the IR excess and disks may not be required to produce the observed SEDs.

CHAPTER 3
THE MID-INFRARED REGIME

3.1 Radiative Processes and Dust Grains

The mid-IR is generally accepted as the wavelength regime between 4 and 25 μm and is dominated by emission from dust grains. Mie theory modeling of dust grains suggests that the scattering efficiency of dust, $Q_s(\lambda)$ decreases towards longer wavelengths such that $Q_s(\lambda) \propto \lambda^{-4}$ (Evans 1994). As shown in Figure 3-1 scattered radiation is negligible in the mid-IR; this regime is dominated by thermal emission from dust grains.

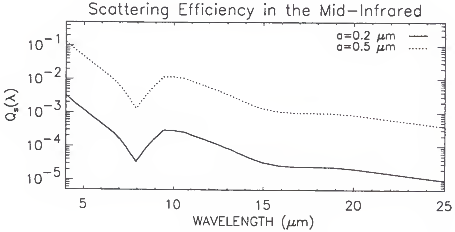

Figure 3-1: Scattering efficiency, $Q_s(\lambda)$ for two grains sizes, a=0.2 μm, and a=0.5 μm Weingartner & Draine 2000).

In solid grains energy is absorbed through vibrations of the crystalline lattice. Under conditions of thermal equilibrium the radiation absorbed by a dust grain is equal to the radiation emitted. Assuming a spherical dust grain with radius a, heated by radiation from a star, the radiation absorbed and emitted are as follows:

$$\int_0^\infty B_\nu(T_*)\pi a^2 Q_a(a,\nu)d\nu = \int_0^\infty 4\pi a^2 Q_e(a,\nu)B_\nu(T_d)d\nu \tag{3-1}$$

Where T_* and T_d are the star and dust temperature respectively, Q_a and Q_e are the absorption and emission efficiencies respectively, B_ν is the Planck function, and ν is frequency.

Most authors suggest that these dust grains are composed of "astronomical silicate", a term used to denote silicate grains, of uncertain chemical composition which give rise to the observed thermal emission in the infrared (Draine & Lee 1984; Gillett et al. 1975; Mathis 1990). Modeling of the UV to IR emission from dust grains has indicated that it may consist of a mix of graphite and silicate grains (Draine & Lee 1984) with silicate dominating the IR emission. The absorption and emission efficiencies, Q_a and Q_e, of astronomical silicate depend on the precise grain composition, size, and wavelength of the radiation. Under conditions of thermal equilibrium Q_a and Q_e should be equal and are proportional to $1/\lambda$ for grains which are small in comparison to the wavelength, and approach 1.0 for grains which are large in comparison to the wavelength of the radiation. Most studies of circumstellar grains are based upon research that has been done concerning the properties of grains in the interstellar medium (ISM). Interstellar grains are assumed to be a mix of small grains, ($a<0.25$ μm) and to have a size and composition distribution as described by Mathis, Rumpl & Nordsiek (1977).

Detailed calculations of grain properties have been done by Draine & Lee (1984), Laor & Draine (1993), and Weingartner & Draine (2000) for spherical grains of astronomical silicate using Mie theory. The authors constructed dielectric functions in the mid-infrared by using observations of thermal emission from the Trapezium star-forming region. I show in Figure 3-2 Q_a for 0.2 and 0.5 μm grains as calculated by Weingartner & Draine (2000).

Grain temperatures in the mid-IR are usually a few hundred Kelvin. Assuming that the grains radiate like blackbody Planck functions, it is easy to calculate the temperature at which a grain radiates when its peak intensity occurs at a specific

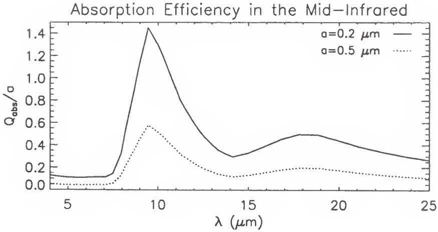

Figure 3-2: Absorption efficiency, $Q_{abs}(\lambda)$, of astronomical silicate, weighted by grain size, a, for two grain radii; a=0.2 μm, and a=0.5 μm (Weingartner & Draine 2000).

wavelength. The Wien displacement law states that

$$\lambda_{max} T_{Wien} = 2890 \, \mu m \, K \tag{3-2}$$

Thus, a blackbody which peaks at 10 μm has a temperature of 289 K. I show in Figure 3-3 plots of $\lambda \, B_\lambda(T)$ versus λ for several blackbodies characteristic of the mid-IR regime. Note that $\lambda \, B_\lambda(T)$ is power per unit area and the power function peaks at $\lambda_{max} T = 3669 \, \mu m \, K$.

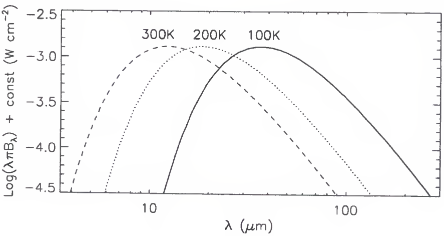

Figure 3-3: Mid-IR blackbody curves calculated for thermal equilibrium from the Planck function.

An estimate of dust temperature as a function of distance from a star, may be derived assuming thermal equilibrium, and some knowledge of Q_a. A Planck-averaged efficiency is defined as:

$$\langle Q(T,a)\rangle = \frac{\int B_\nu(T) Q_{\nu,a} d\nu}{\int B_\nu(T) d\nu} \tag{3-3}$$

Where B_ν is the Planck function, and $Q_{\nu,a}$ is monochromatic emissivity at frequency ν for grain size, a. Next we recall that:

$$\int_0^\infty B_\nu(T)\, d\nu = \frac{\sigma T^4}{\pi} \tag{3-4}$$

and we estimate from observations that the monochromatic efficiency in the infrared, $Q_{\nu,a} \propto \nu^n$, where n is approximately 1 (other values may be more appropriate at longer wavelengths) (Lynch & Mazuk 2000). The Planck-averaged efficiency now becomes

$$\langle Q(T,a)\rangle = \frac{2h\pi}{c^2}\frac{k^{4+n} T^n}{h^{4+n}} \int \frac{x^{3+n}}{e^x - 1} dx, \quad x = \frac{h\nu}{kT} \tag{3-5}$$

Where k is the Boltzmann constant, h is the Planck constant, and c is the speed of light. The integral is a constant of the form

$$\int \frac{x^{3+n}}{e^x - 1} dx = (n+3)!\,\zeta(n+4) \tag{3-6}$$

Thus, we find that

$$\langle Q(T,a)\rangle \propto T^n \tag{3-7}$$

Finally, we equate energy absorbed with energy emitted, using $\langle Q_a\rangle \propto T_*$ and $\langle Q_e\rangle \propto T_d$:

$$\frac{L_* \pi a^2}{4\pi r^2}\langle Q_a\rangle = \sigma T_d^4 \langle Q_e\rangle 4\pi a^2 \tag{3-8}$$

$$r = \left[\frac{L_*}{16\pi\sigma T_d^4}\frac{T_*}{T_d}\right]^{1/2} \tag{3-9}$$

Where L_* is stellar luminosity, T_* is stellar temperature, T_d is dust temperature, a is dust grain radius, and r is distance from star. For a B0 Herbig star, ($L_* \sim 20{,}000\ L_\odot$, and T_*=36,000 K; Gray 1992) we find that dust 1300 AU from the star will radiate at mid-IR temperatures (300 K).

3.2 Mid-IR Spectral Features

As can be seen in Figure 3-2 astronomical silicate grains exhibit broad absorption and emission features peaking at 9.7 and 18 μm. These features have been attributed to the stretching and bending of the Si-O bonds in silicate grains (Mathis 1990), however the precise chemical composition of these features is still controversial. Laboratory observations of the properties of olivine, amorphous olivine smoke, and radiation damaged olivine have shown close, but not perfect fits to observations (Draine & Lee 1984) and the term "olivine" itself refers to a large class of minerals which have differing optical constants (Lynch & Mazuk 2000).

Models of the silicate features generally utilize small, compact grains ($a<0.25\mu$m) characteristic of the ISM. However, many studies of the infrared emission from Ae/Be stars have indicated that circumstellar grains are larger than those present in the ISM and may even be porous (Gorti & Bhatt 1993; Yamashita et al. 1989; Reimann et al. 1997; Hanner et al. 1994a; Pezzuto et al. 1997). Recent high resolution mid-IR spectra by the Infrared Space Observatory (ISO) have indicated that some Ae/Be stars have dust mixtures that include crystalline silicates (Malfait et al. 1998; Waelkens et al. 1996). These spectra appear similar to that of comets which are characterized by porous, dust grain aggregates (Hanner et al. 1994b; Hage & Greenburg 1990). Model fits to Herbig star SEDs using large porous grains and comparison of Herbig star spectra with comet spectra appear to support a porous grain model (Henning et al. 1998; Sitko et al. 1999). However, as always there are some objects which appear to be exceptions to the rule and are better fit by grain models of compact amorphous silicate grains (Hanner et al. 1998).

As mentioned briefly in the previous chapter, other grains, not in thermal equilibrium may make important contributions to the IR excess. IRAS spectra were among the first to show sharp emission features superimposed upon the mid-IR spectra of pre-main-sequence stars. These features at 6.2, 7.7, 8.6 and 11.3 μm have come to be known as the Unidentified Infrared Bands (UIBs) (Figure 3-4). The precise composition of the grains giving rise to these features is still under debate, but many authors have attributed this emission to polycyclic aromatic hydrocarbons (PAHs) (Léger & Puget 1984; Allamandola et al. 1989). For ease of reference I will refer to these grains as PAHs in all future discussions of the UIB features. These tiny grains are composed of hexagonal rings of carbon and may be as small as 50 atoms. PAHs are small enough to be considered large molecules and have both electronic and vibrational energy levels. As described in Allamandola et al. (1989) and Evans (1994) an ultraviolet photon initially excites a PAH grain to a higher electronic energy level. Unlike a normal grain, which would then cascade back to the ground electronic state, the PAH grain then undergoes an "internal conversion" to a vibrationally excited state of the ground electronic state. This type of transition occurs when the transition probability for spontaneous downward electronic transition is less than that for the internal conversion transition. No emission or absorption of energy occurs during the transition. The grain then cascades down the vibrational levels of the ground state with the emission of infrared photons (IR fluorescence). The timescale for cooling by IR fluorescence is short compared to the interval between photon absorption events and the grain appears to be hotter than its surrounding media (Puget & Léger 1989; Jourdain de Muizon et al. 1990). Observational evidence has indicated that PAH emission can contribute up to 60% of the mid and far-IR emission of Herbig stars (Brooke et al. 1993; Zavagno et al. 1992). As I shall show in the following chapters, most Herbig stars exhibit PAH emission in their mid-IR spectra and in some cases, this emission can dominate the temperature distribution of Herbig environments.

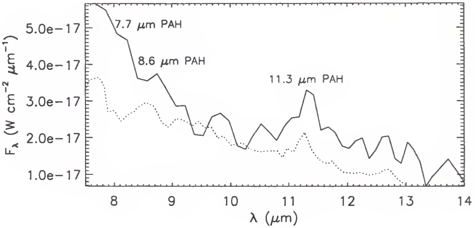

Figure 3-4: Mid-IR spectra of PAH features. IRAS (solid line) and ground based (dotted line; Wooden 1994) spectra of the Herbig star HD 259431 showing PAH emission features.

3.3 Mid-IR Observing Techniques

The mid-IR is a challenging regime for observations. The atmosphere is not completely transparent at these wavelengths, and thermal emission from the atmosphere and the telescope usually dominates over any astrophysical source. Space-based observations have great advantages over ground-based ones, because they are not hampered by the earths atmosphere. However, space observatories have short lifetimes, since it is not technically or economically feasible to refill the cryogens needed for mid-IR detectors. The main atmospheric components which hinder mid-IR transmission are water vapor, carbon dioxide and ozone (Figure 3-5). Earth-based observatories capable of conducting observations in the mid-IR are usually located at high altitudes, above some of the precipitable water vapor, or at extremely dry sites, to limit the impact of water in the atmosphere. One of the best sites in the world is Mauna Kea volcano in Hawai'i. Because the scale height of water vapor is

~ 2 km, at 4.2 km, Mauna Kea is above most of the precipitable water vapor (Allen 1973)(Figure 3-6).

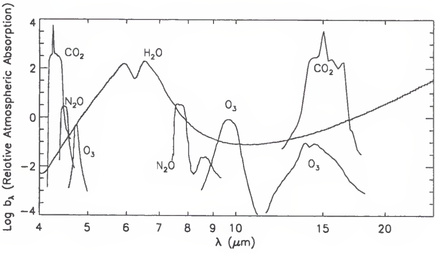

Figure 3-5: Mid-IR absorption due to atmospheric gases.

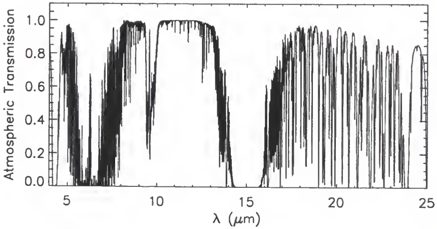

Figure 3-6: Atmospheric transmission in the mid-IR as measured at Mauna Kea (Allen 1973).

Thermal emission from the earths atmosphere also interferes with mid-IR observing. At 10 μm the brightness of the night sky is estimated to be ~ -2 magnitudes (Beckwith 1994). In addition, the observatory dome, telescope, and optics radiate at about the same temperature as a 10 μm blackbody and contribute to the mid-IR emission. Specialized observing techniques known as chopping and nodding have been developed to remove emission from the sky and the telescope. As in the near-IR, sky images are taken in order to subtract the sky background emission from that of the science object. However, the brightness of the sky at mid-IR wavelengths, and the short timescale of sky variability (tenths of a second), requires that many short exposures of the sky and the science object be coadded and subtracted from each other to produce a final image. "Chopping" entails moving the telescope secondary mirror rapidly from an object position to a sky position with exposure times on the order of 10 milliseconds. An additional technique, "nodding", is utilized to remove thermal emission from the telescope optics and structure. The thermal emission from the telescope structure and optics is slightly different along the two beam paths involved in chopping. Nodding involves physically slewing the telescope to a sky position $\sim$10$''$ offset from the science object. In one technique, chopping and nodding are combined, by setting the chop throw and nod throw to the same offset. As shown in Figure 3-7 the procedure involves two sky positions. Chopping in Beam A will produce a positive sky-subtracted image which still includes telescope thermal emission. Chopping in Beam B will produce a negative image (sky - object) with remnant telescope emission. A final product is produced by subtracting Beam B from Beam A to remove the telescope emission. In a typical observation with the University of Florida mid-IR camera, OSCIR, frame times are about 10 milliseconds, and the chop frequency is about 5 Hz. Frames are coadded and sky subtracted to produce a saved image about every 2 seconds. After 20 seconds the telescope is slewed to Beam B and the procedure is repeated. Frame times and chop and nod frequencies are adjusted to reflect weather conditions and for maximum efficiency. An on-source time of 0.5 minutes may take almost 2 minutes due to time spent on the sky and overheads associated with chopping and slewing the telescope.

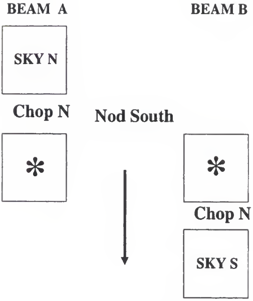

Figure 3-7: Chopping and nodding technique for removing thermal emission from the sky and telescope structure.

Because the mid-IR is dominated by background radiation, different photon statistics apply to this regime than to the optical. In general, the signal-to-noise ratio, SNR, depends upon both instrumental noise, and noise associated with the signal itself:

$$SNR = \frac{Qn_s t}{(\sigma_s^2 + 2\sigma_b^2 + 2\sigma_d^2 + 2p\sigma_R^2)^{1/2}} \tag{3-10}$$

In this case σ_R is the read noise associated with an individual pixel, p is the number of pixels, σ_d is the dark noise, $\sigma_b = \sqrt{Qn_b t}$ is the background sky noise, σ_s is the Poisson noise associated with the signal itself, Q is the quantum efficiency of the detector, n_s is the source flux, and t is the exposure time. In the mid-IR regime background sky noise dominates over all other factors and the equation may be simplified to:

$$S/N \propto \frac{n_s\sqrt{Qt}}{\sqrt{2b}} \tag{3-11}$$

One of the great advantages of the mid-IR regime is that observations are "diffraction limited". At shorter wavelengths atmospheric turbulence can distort images by altering the index of refraction of the air. As light from a point source passes through atmospheric cells it may be refracted and blurred by turbulent motions in the atmosphere (Léna 1988). This variation of the size and shape of a point source is called "seeing". The size scale of the atmospheric cells within which the motions are coherent depends upon wavelength; $r_\lambda \propto \lambda^{6/5}$. At mid-IR wavelengths the atmospheric cells are large and turbulence is minimized. Because seeing is minimized, the optics of the telescope itself will restrict the size of the image and the observation is called diffraction-limited. The intensity distribution of a point source for a particular optical system is called the point-spread-function (PSF). The PSF produced by a perfect optical system with a circular aperture is called the Airy Function and is described by a series of Bessel functions (Equation 3-12).

$$I(r) = \frac{4J_1^2(\rho)}{\rho^2} \tag{3-12}$$

I(r) is intensity, J_1 is a first-order Bessel function, ρ is $\frac{\pi}{\lambda}D sin(r)$, D is the diameter of the telescope aperture, and r is angular distance in radians. This function is oscillatory and has a ring-like structure; I show in Figure 3-8 (solid line) the Airy pattern for a 3 meter telescope at 10.8 μm. Under perfect conditions, the highest resolution achievable in the mid-IR is determined by the Sparrow criteria. The Sparrow criteria is defined mathematically such that $\frac{\partial^2}{\partial r^2}I(r) = 0$. Quantitatively, the minimum separation between two sources that is resolvable according to the Sparrow criteria is $0.95\frac{\lambda}{D}$. A more commonly used resolution criteria is the Rayleigh criteria, defined as the separation between two point sources, such that the center of one point source is superimposed upon the first dark airy ring of the other source. The Rayleigh criteria is $1.22\frac{\lambda}{D}$, this is also the radius of the Airy disk; the bright central maxima of the Airy pattern. For real telescopes, with obscured central apertures, the situation is somewhat more complicated, and the intensity is the sum of several Bessel functions:

$$I(r) = \frac{1}{(1-\epsilon^2)^2}\left[\frac{2J_1(\rho)}{\rho} - \epsilon^2\left(\frac{2J_1(\epsilon\rho)}{\epsilon\rho}\right)\right]^2 \tag{3-13}$$

ϵ = the ratio of the diameter of the occulted aperture to the total diameter. I show in Figure 3-8 the Airy pattern for an unobscured aperture (solid line) compared with the pattern for the obscured aperture telescope, the IRTF (dotted line).

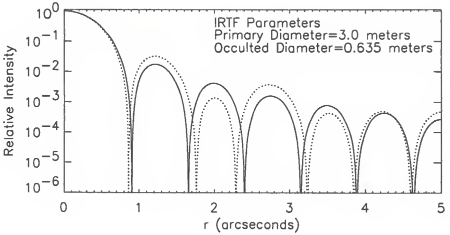

Figure 3-8: Airy pattern for the IRTF (dotted line) compared to Airy pattern for unobscured 3 meter telescope (solid line). Function was calculated at 10.8 μm. The obscured aperture creates a slightly narrower Airy pattern.

Finally, an important consideration in diffraction-limited observing is the encircled energy as a function of radial distance. In a perfect optical system the energy enclosed within a certain radius can be derived by integrating over the intensity and normalizing by the total energy (see Towne 1967 for a detailed derivation):

$$\varepsilon(\rho)/\varepsilon(\infty) = 1 - J_0^2(\rho) - J_1^2(\rho) \tag{3-14}$$

Where $\epsilon(\rho)$ is the enclosed energy at radius ρ, and $\epsilon(\infty)$ is the enclosed energy for an infinitely large aperture. The relative energy enclosed by the Airy disk is 0.838 or 83.8%. In a system with an obscured aperture the function is more complicated; details are discussed in Schroeder (1987) and I show below the final equation:

$$\varepsilon(\rho)/\varepsilon(\infty) = \frac{1}{1-\epsilon^2}\Big[1 - J_0^2(\rho) - J_1^2(\rho)\epsilon^2(1 - J_0^2(\epsilon\rho) - J_1^2(\epsilon\rho)) \\ -2\epsilon \int_0^\rho J_1(\epsilon\rho)\frac{2J_1(\rho)}{\rho}\,d\rho\Big] \tag{3-15}$$

These functions become relevant when determining the correct aperture size for photometric measurements. Aperture sizes should be chosen based upon the size of the Airy disk at the chosen wavelengths and the percentage of the encircled energy.

3.4 Mid-IR Instrumentation

Unlike CCDs in which the photon detecting material and readout array are combined on a single piece of silicon, most modern mid-IR detectors are a hybrid of an infrared photoconducting material and a multiplexer layer which reads out the array. The multiplexer chip contains a unit cell of electronics for each detector as well as circuitry to transfer charges to external electronics. The detectors are usually composed of Si:As doped semi-conductors. Mid-IR detectors absorb light by elevating an electron from a lower to higher energy level within the semiconductor substrate (Beckwith 1994; Rieke 1994). The energy difference between the two bands is called the bandgap. When a photon is absorbed it creates a free electron in the upper band and a matching electron hole in the lower band. A doped detector has an internal electric field. Under the influence of this field the electron and electron hole migrate in opposite directions. Photoabsorption produces a voltage across the detector and charges are accumulated in a capacitor. Current mid-IR detectors also incorporate a "blocked-impurity-band" (BIB) layer which discriminates against low-energy thermally generated charges within the detector (Beckwith 1994; Rieke 1994). The photosensitive layer of BIB type detectors can be more highly doped, increasing its sensitivity to low-energy infrared photons, however, internally produced thermal charges, i.e. the dark current of the detector, are filtered out by the BIB layer.

The first mid-IR instrument to completely survey the sky was the satellite observatory IRAS. IRAS was launched in January 1983 and operated until November 1983. The observatory consisted of a 60 cm telescope cooled by liquid helium to a temperature of 5 K. A detailed description of the mission and instrumentation has been published in the Explanatory Supplement to the IRAS Catalogs (Beichman et al. 1988) and a short summary can be found in (Neugebauer et al. 1984). The survey instruments included a scanning photometer as well a low-resolution ($\lambda/\Delta\lambda$= 20-60) 8 to 22 μm spectrometer. The instrument had four broad photometric filters covering the 12, 25, 60, and 100 μm bands (Figure 3-9). IRAS made pointed observations as well as a survey of the entire sky in all four bandpasses. The survey array included 62 infrared detectors of 3 types; Si:As detectors sensitive to the 8-15 μm bandpass, Si:Sb detectors sensitive to the 19-30 μm bandpass, and two Ge:Ga detectors sensitive to the 40-80 and 83-120 μm bandpasses. The average 1σ sensitivity in the 12 and 25 μm bandpasses was $\sim$ 70 and 65 mJy respectively. Detectors for each bandpass were arranged in columns on the array such that during a scan an object would pass over the 100, 12, 25, 60, 12, 25, 60, and 100 micron detectors sequentially. Thus, every source crossing the field of view would be detected at least twice in each bandpass. The spatial scale of the survey data is $\sim$1.5′ per pixel. Because the detector apertures were rectangular, the IRAS PSF is not circular. In addition, the exact shape of the PSF is influenced by the geometry of the scan for an individual observation. Raw data, that has not been processed with deconvolution techniques, has resolutions of 1'×5', 1'×5', 2'×5' and 4'×5' at 12, 25, 60 and 100 microns, respectively. However,

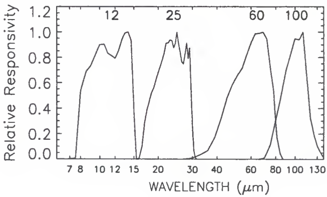

Figure 3-9: Relative response of the four survey channels of IRAS.

archived sky survey data has been smoothed to the 100 μm resolution, (approximately 4'×5') in all bands.

OSCIR (Observatory Spectrometer Camera for the InfraRed) is a mid-IR camera/spectrometer developed by the University of Florida Infrared Astrophysics Group. The OSCIR detector consists of a 128x128 Si:As doped BIB imaging array optimized for the mid-IR regime. Each pixel spans 75 μm on the array which translates to an angular size of $0.223''$ when used with a 3 meter telescope. The detector array is enclosed within a canister cooled to ~10 K by liquid nitrogen and liquid helium dewars. Light enters the cryostat via a potassium crystal window transparent to infrared emission. It then passes through a filter wheel and slit wheel and is focused on the detector array by a series of mirrors (Figure 3-14). Unlike optical detectors, which can have detective quantum efficiencies approaching 100%, mid-IR quantum efficiencies are usually around 50-80%.

The OSCIR filter set includes 10 mid-IR filters spanning the 4 to 21 μm range, and one 2.2 μm filter used for engineering purposes (Figures 3-10, 3-12, 3-11). OSCIR's 1σ sensitivity for 10.8 μm imaging at the Infrared Telescope Facility (IRTF) 3 meter is ~ 1 mJy in 1 hour of chopped integration for a point source. OSCIR is also capable of low-resolution (R ~100) 7 to 13 μm spectroscopy and has six slits of various widths which can be used to achieve a wide range of spectral resolutions. The spectroscopic capabilities of OSCIR were not utilized for this thesis. I show in Figure 3-13 a plot of OSCIR's quantum efficiency over the mid-IR regime.

OSCIR has been utilized as a visitor instrument at the IRTF, CTIO, and Keck observatories. It is currently the facility mid-IR instrument at the newly commissioned Gemini Observatory in Hawaii. I show in Table 3-1 the telescope characteristics, plate scale, field of view, and theoretical radius of the Airy disk for each of the above telescopes.

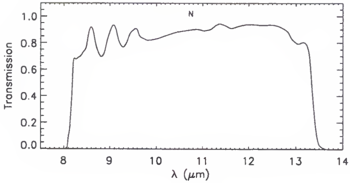

Figure 3-10: Transmission of OSCIR broad N filter.

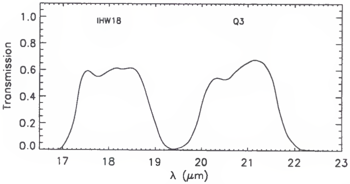

Figure 3-11: Transmission of OSCIR long wavelength filters.

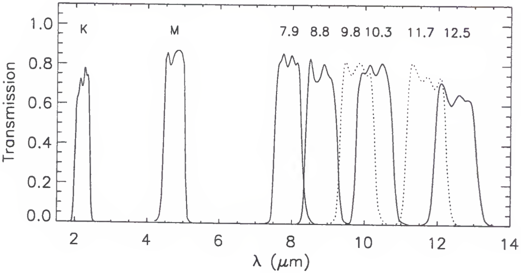

Figure 3-12: Transmission of OSCIR narrow-band filters.

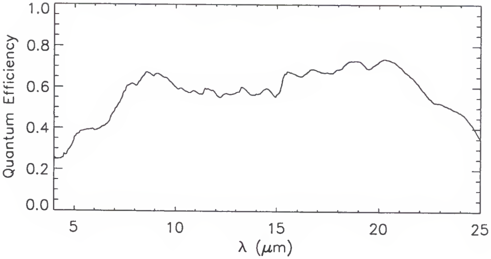

Figure 3-13: OSCIR quantum efficiency.

Table 3-1: OSCIR Characteristics at Various Telescopes

Telescope	D (m)	O (m)	Scale($''$/pixel)	FOV($''$)	Airy Disk Radius($''$)
IRTF	3	0.64	.223	28.5x28.5	0.86
CTIO	4	1.5	.183	23.4x23.4	0.60
Gemini N	8.1	...	.089	11.4x11.4	0.34
Keck	10	1.8	.062	7.9x7.9	0.26

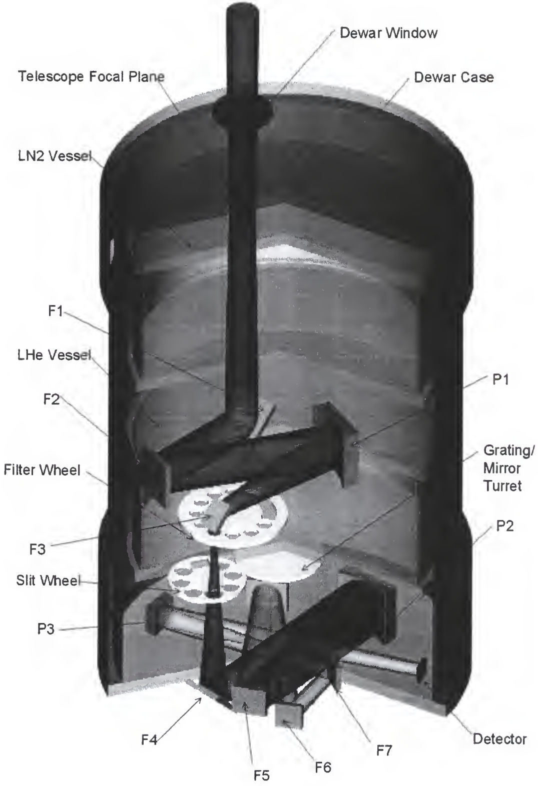

Figure 3-14: The OSCIR Mid-IR Camera/Spectrometer.

CHAPTER 4
THE SAMPLE AND OBSERVATIONS

Sample objects were initially chosen from the Hillenbrand et al. (1992) and Thé et al. (1994) lists of Herbig stars. Objects were selected for their luminosity, and potential to illuminate dust to large radial distances. Additional objects were added to the sample which possessed PAH emission features in their IR spectra. Finally, several objects were added that had spectroscopic features suggestive of circumstellar disks and/or were nearby, increasing the possibility of resolving extended emission. Most of the sample consists of objects that fall into the Hillenbrand Group I class which have been interpreted as objects possessing circumstellar disks. However, the sample also includes several unclassified objects and a few Group II objects. The observing log for the entire data set is presented in Table 4-1.

4.1 General Observational Methodology

Observations were made over a period of three years at three different telescope facilities. The general observation methodology involved observing a flux calibration star followed by a PSF star, an astrometry star, and the science object. This sequence was repeated throughout the observing run. Telescope focus was checked and adjusted about once an hour, and careful notation was made of humidity and weather. Most observations were conducted at airmasses less than 1.5 to minimize the effects of atmospheric extinction.

Flux calibration stars were usually chosen from a set of standard stars for which calibrated infrared models were available. However, the paucity of mid-IR standards required that in some cases flux calibrators were chosen from stars that simply had existing mid-IR photometry. If possible, flux calibrators were observed throughout a range of airmasses in order to determine any needed corrections for atmospheric extinction. The calibration procedure will be described in detail in section 4.6.

Astrometry stars were needed to accurately locate the objects in the small OSCIR field-of-view. Some objects were not optically visible and offsetting from nearby stars was important to locate them. In addition, the telescope coordinate system often drifted a few arcseconds during large slew maneuvers. The procedure for locating a science target involved zeroing the telescope coordinate system on an astrometry star located within a few arcminutes of the science target. Then a small slew was performed to the location of the science target. Astrometry stars were chosen from the Positions and Proper Motions (PPM) catalogue (Röser & Bastian 1988). These stars were bright (m_v<10) stars in the vicinity of the science targets with high precision coordinates and proper motions.

PSF stars were compared to the radial profile of science objects in order to determine whether extended emission was present. In addition, these sources were used in later analysis to convolve science targets to a desired spatial resolution. PSF stars were bright (m_v<5), solitary, K or M class stars chosen from the PPM catalogue. These stars were located as near as possible to the science targets, but in some cases were as much as a few degrees distant. Exposure times for these objects ranged from 0.5 to 1.0 minutes.

4.2 IRTF Observations

The IRTF is an infrared optimized telescope located at 13,670 feet elevation on the summit of Mauna Kea volcano in Hawai'i at a latitude of 19 degrees. The observatory and telescope structure were designed to minimize their contribution to background infrared emission. For mid-IR observing, the IRTF 3 meter primary mirror is paired with a 0.24m f/35 chopping secondary. Observing runs using OSCIR at the IRTF occurred in December 1995, December 1996, September 1997, and November 1999. In all cases, a chopping secondary throw of 30″ N-S was used. Frame times were adjusted according to observing conditions, but generally ranged between 10-20 milliseconds. The estimated 1σ detection level at 10.8 μm in 1 hour of chopped integration at the IRTF is 1 mJy for a point source, or 0.25 mJy/pixel.

4.3 CTIO Observations

The CTIO Blanco 4 meter telescope is located in a very arid area near La Serena, Chile at an elevation of 7300 feet and a latitude of -30 degrees. For mid-IR observing, the CTIO primary mirror is paired with a ~0.38m f/30 chopping secondary. The observatory is not optimized for infrared observations and has a higher thermal background and thus achieves the same detection sensitivity as the smaller IRTF telescope. OSCIR observing runs at CTIO occurred in July 1998, November 1998, and August 1999. In all cases a chopping secondary throw of 23″ N-S was used and frame times ranged between 10 to 30 milliseconds.

4.4 Keck Observations

In May 1999 OSCIR was a Visitor Instrument at the Keck II telescope. Keck II is one of a pair of twin 10 meter telescopes located on the summit of Mauna Kea volcano in Hawai'i. The 10 meter diameter primary mirror consists of 36 hexagonal 1.8 meter diameter segments. The segments are operated in concert to function as a single mirror, using a computer-controlled system of sensors and actuators. Due to the hexagonal shape of the mirrors, the point-spread-function of the system appears hexagonal, rather than circular. For mid-IR observing, the Keck primary is paired with a f/40 secondary. During the May 1999 observing run a chopper throw of 10″

N-S was used and frame times ranged from 10 to 25 milliseconds. The telescope is not optimized for infrared observing and the estimated 1σ detection level at 10.8 μm in 1 hour of chopped integration at the Keck II is 0.172 mJy for a point source, and 0.022 mJy/pixel.

4.5 Other Observations

Much of the analysis of Herbig stars depends upon knowledge of their optical properties. However in some cases the optical counterpart to the mid-IR source may be unknown or uncertain. In collaboration with Dr. Stéphane Vennes of UC Berkeley/ANU I obtained R band imaging of AS 310 to better relate optical companions to objects seen in the mid-IR. Observations were conducted 17 June 2000 with the Monash 2048x4096 CCD imager. Images were binned for a final plate scale of 0.364″/pixel. The field was not sky subtracted or flat-fielded, and flux calibration was performed with a nearby field star; GSC 05120-00160, for which the US Naval Observatory catalogue lists a Cousins R magnitude of 12.0.

4.6 Calibration

Zero magnitude fluxes of the OSCIR filter set were established by utilizing models of the atmospheric transmission at Mauna Kea, transmission curves of the filters, a model of α Lyra (Cohen et al. 1999), and spectra of the various calibration stars (Cohen et al. 1999; Hauschildt et al. 1999; IRAS LRS database) (Figure 4-1).

Bandpass-normalized fluxes for the OSCIR filter set were calculated as follows:

$$\nu_{eff} = c \int_{\lambda 1}^{\lambda 2} \frac{T_{filter}(\lambda)\, T_{atm}(\lambda)}{\lambda^2} d\lambda \tag{4-1}$$

$$F_\nu = c\, \frac{\int_{\lambda 1}^{\lambda 2} F_\nu(\lambda) \frac{T_{filter}(\lambda)\, T_{atm}(\lambda)}{\lambda^2} d\lambda}{\Delta \nu_{eff}} \tag{4-2}$$

Where F_ν is the calculated flux in Jy, $F_\nu(\lambda)$ is the model flux at wavelength λ, ν_{eff} is defined as the effective frequency of the filter, $\Delta\nu_{eff}$ is the effective bandwidth

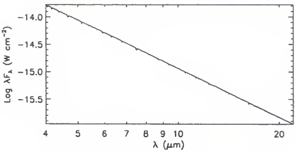

Figure 4-1: Cohen Model of Alpha Lyra.

of the filter, c is the speed of light, T_{filter} is the filter transmission, and T_{atm} is the atmospheric transmission. Flux standards were generally observed for 0.25-0.50 minutes. The data was subsequently reduced, small variations in the background were fit and subtracted, and the total analog-digital-units (ADUs) were measured within an appropriate aperture. A calibration factor was then determined by dividing the predicted flux in millijanskies by the observed ADUs. If observations were obtained at more than a single airmass, the data were used to solve for the calibration factor as a function of airmass, and the science target fluxes were subsequently corrected for the effects of airmass. More details of the data reduction process are presented in Chapter 5. OSCIR fluxes for all mid-IR standards used in this research are tabulated at the end of this chapter.

4.7 Summary of Object Characteristics

In the following I briefly describe some of the important characteristics of each object discussed in this thesis. Vital statistics for the entire data set, including estimated spectral type, distance, age, and Hillenbrand Group number, are shown in Table 4-2.

4.7.1 LkHα 198 and V376 Cas

LkHα 198 and V376 Cas are Group II Ae/Be stars located within a small star forming region at 900 pc. V376 Cas is located approximately 35″ north of LkHα 198. V376 Cas is associated with a bipolar nebula in the optical and near-IR and exhibits the largest linear polarization found in any Herbig star (Leinert et al. 1991; Asselin et al. 1996). Analysis of polarization maps implies that this star may be viewed through an edge-on disk (Asselin et al. 1996).

Recently, mid-IR and millimeter companions were found at separations of 6″ and 21″ from LkHα 198 (Lagage et al. 1993; Hajjar & Bastien 2000). The mid-IR companion, LkHα 198-IR, possesses a silicate absorption feature; corrected for absorption the source may be as luminous as the primary and has been classified as a Herbig star (Lagage et al. 1993; Leinert et al. 1997). Ground-based spectra of the primary show a silicate emission feature and 11.3 μm PAH feature (Hanner et al. 1998).

Hajjar & Bastien suggest that the millimeter companion, LkHα 198 C, may be an extreme Lada Class I object, transitional between the heavily embedded Lada Class 0 objects, which cannot be detected at infrared wavelengths, and the less embedded Class I objects, which may be viewed through an edge-one disk. This classification would correspond to the Hillenbrand Group II to Group I class range. A bipolar molecular outflow and several HH objects and jets also occur in the vicinity of LkHα 198 (Canto et al. 1984; Corcoran et al. 1995). Hajjar & Bastian (2000) argue that the outflow originates from Lkhα 198 C and they interpret molecular maps as the signatures of a large-scale molecular disk.

4.7.2 RNO 1 Complex

The RNO 1 region is located within the dark cloud L1287 at a distance of ~850 pc. This region contains a bipolar molecular outflow, as well as at least five protostellar sources visible in the near-IR (Weintraub & Kastner 1993; Yang et al. 1991) Both RNO 1B and RNO 1C have been classified as FU Orionis pre-main-sequence stars, while RNO 1 may be a Herbig star (Persi et al. 1988; Mookerjea et al. 1999). Weintraub et al. (1996) have found several polarimetric peaks which indicate the positions of two deeply embedded sources. In one case the peak is coincident with the position of an IRAS far-IR source. The region is also associated with a radio continuum source, several water masers, and methanol maser emission (Fiebig et al. 1996; Wouterloot et al. 1993; Szymczak et al. 2000). Analysis of the velocity structure of the maser emission suggests an origin in a circumstellar disk (Fiebig et al. 1996). Finally, Graham & Chen (1991a) have detected a 3.1 μm ice absorption feature around RNO 1B; such a feature could be formed within a dense circumstellar disk.

4.7.3 XY Per

XY Per is a binary Herbig star system with a separation of 1.2″ located at ∼ 160 pc. The system exhibits strong 3.29 μm emission (Brooke et al. 1993) and may possess weak PAH emission at 11.3 μm (Hanner et al. 1998). In addition, XY Per is one of only three systems in which the 3.4 μm PAH feature is detected (Brooke et al. 1993). The system is located near a CO peak (Kutner et al. 1980) and is a strong IRAS source ($F_{12\mu m}$=3.9 Jy).

4.7.4 AB Aur

AB Aur is the archetype and optically brightest member of the Ae/Be star class. This nearby, 160 pc, Group I Herbig star shows the 9.7 μm silicate feature in emission, as well as mid-IR features attributed to PAH grains (van den Ancker et al. 2000a). Marsh et al. (1995) find extended emission in deconvolved mid-IR images that they interpret as a circumstellar disk inclined at 85 degrees. Mannings & Sargent (1997) detect CO emission extended to 450 AU, at an inclination of ∼

76 degrees. Their observations also indicate a Keplerian velocity gradient for the emission which suggests a rotating disk of gas. Grady et al. (1999) also find spectral features indicating gaseous accreting material in the ultraviolet. However, the nature of the circumstellar material of this object is still uncertain, since recent near-IR interferometry suggests a ring of material rather than a disk, and an inclination of less than 45 degrees (Millan-Gabet 1999).

4.7.5 LkHα 25

LkHα 25 was classified by Hillenbrand et al. (1992) as a Group II object and is located at a distance of ~800 pc in the young cluster NGC 2264. The object exhibits a 9.7 μm silicate emission feature (Rydgren & Vrba 1987) as well as PAH emission at 3.29 μm (Brooke et al. 1993). LkHα 25 possesses a large IR excess and an E(B-V) color indicative of extinction from large grains (Sitko et al. 1984).

4.7.6 HD 259431

HD 259431 is a bright Group I Herbig star located at ~800 pc. This object has been found to be a source of both 3 μm and mid-IR PAH emission (Brooke et al. 1993; Wooden 1994). IRAS spectroscopy and ground-based observations by Berrilli et al. (1992) have indicated a 10 μm silicate absorption feature. Recent observations suggest that HD 259431 may have 1 or more companions (Corporan & Lagrange 1999; Ciardi et al. 1999). The object is a source of emission ranging from radio to x-ray wavelengths (Damiani et al. 1994, Skinner et al. 1993).

4.7.7 HD 100546

HD 100546 is a nearby, ~100 pc, Group II Herbig star. The object exhibits a strong IR excess and variable ultraviolet absorption, yet is not associated with any known star forming region (Grady et al. 1997). Its age, and isolation suggest that it may be in an evolutionary class between the youngest embedded stars and more evolved main-sequence objects such as Beta Pic. Its infrared spectra shows the well known 3.29, 7.7, and 11.3 μm PAH features, as well as two little understood emission features at 3.45 and 3.52 μm. Comparison of its spectrum to that of the comet Hale-Bopp suggests that the mid-IR emission arises in a dusty cometary cloud (Malfait et al. 1998). Shorter wavelength observations indicate that the star itself may be accreting giant protocomets (Grady et al. 1997).

4.7.8 HD 97048

HD 97048 is a Group I Herbig star located at 140 pc in the Chameleon star forming region. The infrared spectrum of this object shows the 3.29, 8.6, and 11.3 μm PAH features as well as the lesser understood features at 3.4 and 3.5 μm (Blades & Whittet 1980; Aitken & Roche 1981). Prusti et al. (1994) and Henning et al. (1998) found extended emission in the mid-IR and millimeter respectively. A ROSAT x-ray source is located within 25″ of the optical position of HD 97048 (Fiegelson et al. 1993) and a strong 1.3 mm source is found within 6″ (Henning et al. 1998).

4.7.9 DK Cha

DK Cha, better known as IRAS 12496-7650, is a heavily embedded Herbig star located in the Chameleon II star forming region at distance of ~200 pc. This object is classified in the Hillenbrand Group II evolutionary class (Pezzuto et al. 1997). IRAS 12496-7650 is extremely faint optically (V=18.66) but has a far-IR flux more than twice that of any other source in the region (Hughes et al. 1991). The object is also associated with an OH maser (Gaylard & Whitelock 1988), several HH objects, and far-IR and CO outflows (Hughes et al. 1989; Knee 1992). IRAS spectra exhibit a 9.7 μm silicate absorption feature (Hughes et al. 1991) and near-IR spectra show an absorption feature due to ice at 3.1 μm (Graham & Chen 1991b). A millimeter continuum peak occurs within 7″ of the optical location (Henning et al. 1998) and observations with the ASCA x-ray telescope detected a source within 1′ of the optical position, and well within ASCA pointing errors (Yamauchi et al. 1998).

4.7.10 KK Oph

KK Oph is a Group I Herbig star located at 310 pc near the B59 dark cloud (Herbig 1960; Hipparcos catalog). KK Oph possesses a close optical/near-IR companion, with a separation of 1.61″ which may be a T Tauri star (Leinert et al. 1997; Pirzkal et al. 1997). A radio continuum source lies within 1.57″ of the primary, but is not coincident with the companion (Skinner et al. 1993). Berrilli et al. (1992) find a 9.7 μm silicate emission feature. Grady et al. (1996a) find accreting gas in UV and optical spectra of KK Oph. The star is also a large amplitude variable (Herbst & Shevchenko 1999).

4.7.11 Juggler Nebula/AFGL 2136

The Juggler Nebula contains the mid-IR source AFGL 2136 located at a distance of 2000 pc in a dense molecular cloud (Kastner et al. 1992). AFGL 2136 is associated with OH, H_2O, and methanol masers (Allen et al. 1977; Dinger et al. 1979; Caswell et al. 1995). A large scale bipolar CO outflow is coincident with the position of AFGL 2136 (Kastner et al. 1994). AFGL 2136 has a deep absorption feature due to ice at 3.1 μm as well as a 9.7 μm absorption feature (Willner et al. 1982). Kastner et al. (1992) have detected a high degree of polarization in the near-IR and have mapped three main sources at 2.2 μm and 28 additional fainter objects within 50″. The above authors argue that the observed polarization, in conjunction with the observation of the ice feature is caused by a nearly edge-on circumstellar disk.

4.7.12 V921 Sco

V921 Sco has been classified as a Group I Herbig star and is located at a distance of 160 pc (Hillenbrand et al. 1992). IRAS and ground-based spectra show emission from PAHs at 3.29, 7.7, and 11.3 μm (Jourdaine de Muizon et al. 1990; Brooke et al. 1993; Benedettini et al. 1998). Berrilli et al. (1992) have found a mid-IR silicate absorption feature and Natta et al. (1993a) detect extended far-IR emission.

Henning et al. (1998) have mapped extended millimeter continuum emission and a strong millimeter peak that does not coincide with the optical position of the star.

4.7.13 MWC 297

MWC 297 is a bright Group I object located at 250 pc in the Aquila Rift (Herbig 1960; Drew et al. 1997). Berrilli et al. (1992) find a mid-IR silicate absorption feature, but IRAS observations appear to show a featureless spectrum (Volk & Cohen 1989). MWC 297 is a strong radio and millimeter source (Skinner et al. 1993; Henning et al. 1994). The object is also coincident with water maser emission (Han et al. 1998). Hamaguchi et al. (2000) recently detected a powerful x-ray flare from this star.

4.7.14 AS 310

AS 310 is a Group I Herbig star located in the Sharpless 2-61 HII region (Sharpless 1959) for which a kinematic distance of 2500 pc was estimated by Georgelin & Georgelin (1970). AS 310 is centered on a CO emission peak in this region (Hunter et al. 1990) and has several optical and near-IR companions (Bastian & Mundt 1979; Finkenzeller & Mundt 1984; Ageorges et al. 1997). The source is associated with strong mid-IR and 3 μm PAH emission (Brooke et al. 1993). Mid-IR observations show an emission feature at 10 μm from silicate grains (Cohen 1974). However, more recent observations by Berrilli et al. (1992) indicate a featureless spectrum. A double-lobed radio source detected by Cohen et al. (1982) is located within 8$''$ of the optically visible primary.

4.7.15 BD +40 4124 Complex

The BD +40 4124 complex contains the Herbig stars BD +40 4124, LkHα 224, and V1318 Cyg as well as numerous other near-IR sources, and is located at a distance of ~1000 pc in the Cygnus Arm (Palla et al. 1995). Hillenbrand et al. (1992) classified both BD +40 4124 and LkHα 224 as Group I sources and Aspin et al.

(1994a) suggest that V 1318 Cyg may also be a Group I object. Near-IR and mid-IR imaging of the region has shown that V1318 Cyg is actually a double source and the southern component is coincident with a water maser, a 10 μm absorption feature, and a CO outflow (Palla et al. 1995; Aspin et al. 1994a). V1318 Cyg is also a large amplitude variable in the optical (Herbst & Shevchenko 1999). Skinner et al. (1993) have observed radio emission in this region, but were unable to conclusively identify it with a specific source. Recent ISO spectroscopy of the three objects has shown that BD +40 4124 exhibits PAH features at 3 μm and in the mid-IR, LkHα 224 is relatively featureless, and the presence of the 10 μm absorption feature is confirmed in V1318 Cyg (van den Ancker et al. 2000b).

4.7.16 LkHα 234

LkHα 234 is one of several pre-main-sequence stars located in the NGC 7129 reflection nebula at a distance of ~1000 pc. LkHα 234 has been classified as a Group I source and has numerous companions, including a mid-IR source associated with strong near-IR elliptical polarization (Weintraub et al. 1994; Cabrit et al. 1997; Leinert et al. 1997; Li et al. 1994). Mid-IR observations indicate a 9.7 μm silicate feature, as well as PAH emission in IRAS spectra (Bechis et al. 1978; Berrilli et al. 1987). LkHα 234 is associated with at least six H_2O masers (Tofani et al. 1995; Cabrit et al. 1997), radio emission (Skinner et al. 1993), a CO outflow (Bechis et al. 1978; Mitchell & Mathews 1994) and an optical/near-IR jet (Ray et al. 1990).

4.7.17 MWC 1080

MWC 1080 is a well known Group I Herbig star. The spectral type and distance of this object are uncertain, but most authors propose a distance of ~2500 pc and classify the object as an early B or A star (Canto et al. 1984; Dibai 1969; Yoshida et al. 1992). MWC 1080 has at least four companions including a 0.8″, companion, an eclipsing binary companion, a 4.7″ near-IR companion, and a more distant, 10″ companion (Leinert et al. 1997; Shevchenko et al. 1994; Pirzkal et al. 1997; Cohen & Kuhi 1979). MWC 1080's IRAS spectrum shows emission at 7.7 and 11.3 μm which has been attributed to PAH grains (Zavagno et al. 1992) and ground-based mid-IR observations have indicated a 10 μm silicate feature and extended emission at 8.8 μm (Deutsch et al. 1995). The object is also associated with a bipolar outflow at millimeter wavelengths (Yoshida et al. 1991).

Table 4-1: Observation Log

Name	Telescope	Date	Exposure(s)										Airmass
			M	7.9	8.8	9.8	10.3	11.7	12.5	N	18.2	20.8	
LkHα 198	IRTF	12/96	...	...	...	...	...	...	...	240	240	...	1.43-1.47
LkHα 198	IRTF	11/99	...	...	...	...	...	...	...	180	120	...	1.29-1.31
V376 Cas	IRTF	12/96	...	...	...	...	...	...	...	360	180	...	1.62-1.81
LkHα 198 mm	IRTF	12/96	...	...	...	...	...	...	...	180	...	...	1.92
AB Aur	IRTF	11/99	...	...	...	...	...	...	...	180	360	360	1.05-1.26
LkHα 25	IRTF	9/97	...	...	...	...	...	...	...	90	90	...	1.17-1.14
LkHα 25	CTIO	11/98	...	...	...	...	...	...	...	300	300	...	1.33-1.36
XY Per	IRTF	11/99	120	180	120	180	120	180	180	180	180	...	1.06-1.12
DK Cha	CTIO	7/98	...	...	60	60	...	60	...	180	180	...	1.56-1.63
RNO 1B	IRTF	11/99	...	...	...	...	...	...	...	180	540	...	1.39-1.43
RNO 1	IRTF	11/99	...	...	...	...	...	...	...	180	180	...	1.40-1.41
HD 259431	IRTF	9/97	...	...	...	...	...	...	...	180	120	...	1.23-1.17
HD 259431	IRTF	11/99	180	180	120	180	120	180	240	180	390	...	1.21-1.05
HD 97048	CTIO	7/98	...	...	...	...	...	...	...	60	60	...	1.61-1.62
HD 97048 N	CTIO	7/98	...	...	...	...	...	...	...	60	...	...	1.63
HD 100546	CTIO	7/98	...	...	...	...	...	240	...	240	240	...	1.36-1.46
V921 Sco	CTIO	7/98	...	...	180	...	180	...	...	660	480	...	1.07-1.41
V921 Sco	CTIO	8/99	180	180	180	180	180	180	180	180	180	...	1.21-1.69
AS 310	IRTF	9/97	...	180	180	180	180	180	180	360	360	...	1.10-1.33
MWC 297	IRTF	9/97	...	...	...	...	...	...	...	180	180	...	1.09-1.10
Juggler	CTIO	7/98	...	...	...	...	...	...	...	180	120	...	1.78-1.93
Juggler	CTIO	7/98	...	...	...	...	...	...	...	120	...	...	1.84
KK Oph	CTIO	7/98	...	...	...	...	...	...	...	240	120	...	1.78-1.93
BD +40 4124	IRTF	9/97	...	...	...	...	...	...	...	210	240	...	1.12-1.19
V1318 Cyg	IRTF	9/97	...	90	90	90	90	330	90	360	90	...	1.09-1.26
V1318 Cyg	IRTF	11/99	...	...	...	...	...	...	...	360	360	...	1.25-1.36
LkHα234	IRTF	9/97	90	180	90	90	90	90	90	360	210	...	1.45-1.61
LkHα234	IRTF	11/99	180	300	...	...	...	...	...	180	60	60	1.45-1.63
MWC 1080	IRTF	12/95	...	...	...	...	...	...	...	240	...	120	1.82-1.86
MWC 1080	IRTF	12/96	180	...	...	...	...	...	...	180	360	...	1.39-1.62
MWC 1080	IRTF	9/97	...	60	60	60	60	60	60	120	120	...	1.45-1.69
MWC 1080	Keck	5/99	...	...	...	...	...	300	60	420	300	...	1.73-1.60

Table 4-2: Ae/Be Star Sample

Name	RA(J2000)	Dec(J2000)	Sp[a]	d(pc)	A_v	Age(My)	Group
LkHα 198 N/S	00 11 27	58 49 50	B3+A-B	600	5.0	...	II
V376 Cas	00 11 26	58 50 03	F0	600	2.9	6	II
RNO 1	00 37 23	63 29 29	F5III	800	3.6	...	...
RNO 1B	00 36 46	63 28 54	F8II	800	9.2	...	I[b]
XY Per A/B	03 49 36	38 58 55	A2II+B6	350	2.3	2	...
AB Aur	04 55 46	30 33 05	A0V	144	0.5	2	I
HD 259431	06 33 05	10 19 20	B1	800	1.6	.05	I
LkHα 25	06 40 45	09 48 02	B7	800	5.0	.2	II
HD 97048	11 08 03	-77 39 18	B9-A0	180	1.2	>2	I
HD 100546	11 33 25	-70 11 41	B9V	103	0.3	>10	II
DK Cha	12 53 16	-77 07 02	A-F:	200	5.0	.04-2	II
V921 Sco	16 59 07	-42 42 08	B4-B5:	500:	3.7	...	I
KK Oph	17 10 08	-27 15 19	A6	160	2.7	>10	I
MWC 297	18 27 40	-03 49 52	B1.5	250	2.9	.03:	I
AFGL 2136	18 22 30	-13 29 40	B5	2000	41:	<.04	...
AS 310	18 33 21	-04 58 07	B1I:	2500	3.4	...	I
BD +40 4124	20 20 28	41 21 51	B2	1000	3.0	<1	I
LkHα 224	20 20 29	41 21 28	A7	1000	3.0	<1	I
V1318 Cyg N/S	20 20 31	41 21 29	A-F:	1000	7.3		I
LkHα 234	21 43 07	66 06 55	B6-B7	1000	2.9	.1-.5	I
MWC 1080	23 17 26	60 50 45	A0I-B0V	2500	4.4-5.4	<1	I

Distances, spectral types, extinctions, and ages cited in the following references: van den Ancker et al. (1998), Fuente et al. (1998), Hamann & Persson (1992), Damiani et al. (1994), Drew et al. (1997), Hillenbrand et al. (1992), Testi et al. (1999), Natta et al. (1997), Kastner et al. (1992), Staude & Neckel (1991), Hughes et al. (1989), Pezzuto et al. (1997), Berrilli et al. (1992), Henning et al. (1993), Canto et al. (1984), Hunter & Massey (1990), Finkenzeller & Mundt (1984), van den Ancker et al. 2000b).

[a] For binaries, spectral types refers to primary, usually derived from optical data.

[b] Henning et al. (1998) classifies as Lada class II which is equivalent to Hillenbrand Group I.

Table 4-3: Calibration Stars

Name	M	7.9	8.8	9.8	10.3	11.7	12.5	N	18.2	Q3	Calibration[a]
α Lyr	158	59	50	40	37	28	25	38	12	9	Cohen model
α Ari	255	113	96	81	75	59	52	75	25	19	Cohen model
α Tau	2042	871	750	640	600	485	425	601	200	156	Cohen model
α Her	4127	1859	1609	1377	1289	1041	917	1291	456	343	Engelke
γ Aql	159	106	90	77	73	57	51	72	24	19	Cohen model
μ Cep	...	985	1184	1828	1820	1244	977	1321	947	795	IRAS
β Peg	1183	513	441	376	351	282	248	352	122	92	Cohen model
β And	822	357	303	265	249	200	176	246	84	64	Cohen model
η Sgr	...	320	255	217	206	168	146	206	64	49	IRAS
γ Cru	2700	1277	1058	893	847	687	602	851	286	220	Cohen model
α Sco	7809	3396	2924	2492	2329	1872	1645	2335	814	611	Engelke
β Gru	...	1570	1327	1091	1012	794	685	1029	335	254	IRAS
σ Lib	...	248	207	180	169	139	125	170	64	60	IRAS
α Boo	2356	1038	883	727	674	525	460	683	219	168	Cohen model
τ4 Eri	415	194	166	135	126	102	90	129	43	33	Hauschildt model
μ UMa	290	124	108	94	88	72	63	88	30	23	Cohen model
β Gem	434	180	151	122	112	88	77	116	37	28	Cohen model

[a] Fluxes determined from Cohen spectral models, Hauschildt spectral models, IRAS spectra normalized to narrow band photometry cited in van der Bliek, Manfroid, & Bouchet (1996) and ratio of Engelke functions which scale spectra of nearest spectral type for which a Cohen model exists.

CHAPTER 5
DATA REDUCTION AND ANALYSIS

5.1 File Structure

OSCIR observations are recorded in six-dimensional FITS (Flexible Image Transport System) files. The structure of a mid-IR observation utilizing chopping and nodding techniques was diagrammed in Chapter 3. Individual elements of the observational sequence are saved in the six dimensions of the FITS file. The first two FITS dimensions contain the x and y dimensions of the array. The third dimension contains the number of chop beams, which is always two, and consists of a source position, and a sky or reference position. A single exposure frame may have an exposure time of only 10 milliseconds, but as many as 30 of these frames are subsequently coadded. The term "saveset" signifies the pair of images produced by coadding a number of sky frames into a final image and coadding a number of source frames into a final image for each nod position. The fourth dimension of the FITS file contains the number of savesets per nodsets, where a nodset consists of observations made in two nod positions. The fifth dimension contains the number of nod positions, which is two if the telescope is nodding. The sixth dimension contains the number of nodsets per observation. Other information contained within the OSCIR data file includes the individual frame time, the airmass, and the exposure time. An example of a FITS header listing the relevant parameters for an observation of α Tau is shown below.

```
Object - Alpha_Tau
Filter - IHW18 (19000)

Obsmode  = chop-nod
Savesets = 10
Nodsets  = 4
```

```
NAXIS   =                    6 /
NAXIS1  =                  128 /X dimension of array
NAXIS2  =                  128 /Y dimension of array
NAXIS3  =                    2 /Number of chop positions
NAXIS4  =                   10 /Number of savesets per nod phase
NAXIS5  =                    2 /Number of nod positions
NAXIS6  =                    4 /Number of nod sets
DATE    = '1999-11-10'         / Creation date (CCYY-MM-DD) of FITS header
INSTRUME= 'oscir   '           /
COMPSTAT= 'normal  '           /Completion status
FILTER  = 'IHW18 (19000)'      /Filter (motor position)
SLIT    = 'OpenHole (-13199)'  /Aperture Slit (motor position)
GRATING = 'Mirror (-1499)'     /Grating/Mirror (motor position)
OBSMODE = 'chop-nod'           /Observing mode
FRMTIME =              20.0980 /Frame time - ms
SAVEFREQ=             0.497562 /Save frequency - Hz
OBJTIME =              1.06614 /On-source time  - min
CHPFREQ =              4.97562 /Chop frequency  - Hz
NODTIME =              20.0980 /Nod time   - sec
EXPTIME =              3.48365 /Elapsed time (min)
TOTFRMS =                  160 /# of coadded frames saved
OBJECT  = 'Alpha_Tau'          /
EPOCH   = 'B1950   '           /Epoch of coordinates
RA      = '04 33 02.9'         /hr mn sc
DEC     = '16 24 37'           /dg mn sc
FOCUS   = '-0.92   '           /telescope focus readout
LONGITUD= '155 28 56.0000'     /observatory west long. (dg mn sc)
LATITUDE= '19 49 56.0000'      /observatory lat. (dg mn sc)
UTDATE1 = '10/11/1999'         /Starting UT Date - dy/mn/yr
UTDATE2 = '10/11/1999'         /Ending UT Date - dy/mn/yr
UTTIME1 = '14:23:16'           /Starting UT Time - hr:mn:sc
UTTIME2 = '14:26:44'           /Ending UT Time - hr:mn:sc
LST1    = '7:20:55 '           /Starting LST Time - hr:mn:sc
LST2    = '7:24:24 '           /Ending LST Time - hr:mn:sc
HA1     = '+2:45:0 '           /Starting HA - hr:mn:sc
HA2     = '+2:48:30'           /Ending HA - hr:mn:sc
JD1     = '2451493.1'          /Starting JD number
JD2     = '2451493.1'          /Ending JD number
AIRMASS1= '1.29035 '           /Starting airmass
AIRMASS2= '1.30575 '           /Ending airmass
```

5.2 Data Reduction Procedure

Files are manipulated using a series of specialized IDL routines developed by Dr. Robert Piña. The standard data reduction technique involves reading the FITS file into an IDL structure containing the sky, source, savesets, and nodsets. Initial data reduction involves running a "movie" of the entire series of savesets, using the IDL routine f6movie.pro. F6movie automatically displays the sky-subtracted subexposures contained within each nodset. Sets with instrumental artifacts, or bad seeing are excluded from further data reduction. The data reduction routine f6get.pro is then used to coadd individual elements of an exposure. First, the reference beam is subtracted from the source beam for each series of observations for a particular nod position. For example, an observation with 2 source exposures and 2 sky exposures for EACH nod beam would produce 2 differenced observations (diffsets) for each nod beam. Next, the first "diffset" for beam A is coadded with the first "diffset" for beam B to to subtract the telescope thermal emission and produce an exposure called the "sig". The preceding step is repeated for each pair of diffsets and the entire procedure is repeated for EACH nodset. Next, all good sigs are coadded into one image per nodset. Individual images are then mosaicked and coadded using the IDL routines mosref.pro and mosdrift.pro. An example of the process of differencing and coadding frames from the nod beams is shown in Figure 5-1 for the Herbig star HD 259431.

5.2.1 Airmass Correction

After a reduced product is created, the image is flux calibrated. Observations of flux calibration stars spanning a range of airmasses are tabulated and fit with a second order polynomial to derive the calibration constant as a function of airmass. In general, broad N band observations are little affected by airmass. In all cases N and 18.2 μm observations were corrected for the effects of airmass. Insufficient observations of the flux calibrators in the narrow band filters precluded applying any airmass corrections directly. In all cases, excluding the 1999 August observations of V921 Sco and the Keck observations of MWC 1080, the flux calibrator star was observed within 0.2 airmasses of the science object. Imaging experiments conducted in November 1999 have indicated that the correction for extinction at 7.9, 8.8, 10.3, 11.7, and 12.5 μm is negligible. During this observing run, flux calibration stars were observed throughout a range of airmass to study the dependence of instrumental flux

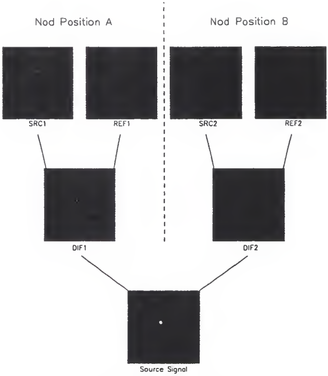

Figure 5-1: Data reduction of chopped, nodded observations. Observations of the object and sky (src1, ref1) are made in Nod Position A. The process is repeated in Nod Position B. The two diffsets are coadded to produce the final image; Source Signal.

on atmospheric extinction. In the above filters less than a 3% change in the calibration factor occurred when airmass changed by 0.1. However, significant variation was seen for observations in the M and 9.8 μm filters. No linear trend of calibration factor with airmass was able to be determined from the existing 9.8 μm observations. This filter spans an atmospheric ozone feature; variability in the strength of this feature may be affecting the observations. I estimate a 10% uncertainty in the calibration factor at 9.8 μm. Observations of flux standards in the M filter show also show large variability with no obvious trend. I estimate a 15% uncertainty in the calibration factor at 4.8 μm.

Airmass corrections were performed for all Keck N and 18 μm observations. The remaining Keck observations were made in the narrow 11.7 and 12.5 μm filters. As discussed above, I assume that any airmass correction is small at these wavelengths.

V 921 Sco was observed in 1999 August as well as 1998 July. During the 1999 observations, the flux calibrator star was within 0.2 airmasses of the science for all observations except the 7.9, 9.8, and 11.7 μm observations. For this data the airmass of the calibrator was within 0.3-0.4 airmasses of the science object. As discussed above, observations made at 9.8 μm appear to be especially sensitive to airmass, thus I estimate a 10% uncertainty in the fluxes at this wavelength.

In summary, I adopt 5% uncertainties for the narrowband filters, with the exception of the 9.8 and M filters for which I adopt uncertainties of 10photometric uncertainties are discussed in Chapter 6.

5.2.2 Flat Fielding

Figure 5-2 shows a 10 μm image of the detector under uniform illumination. There are approximately 10 dead pixels distributed across the array and about the same number of hot pixels with significantly different responsivity than the mean. The lower right corner shows a small degree of vignetting, but the response of the array is in general very flat; the flat-field varies by ~5%. The vertical structure seen in Figure 5-2 is fixed and is removed during the chop-nod process.

5.2.3 Sky Variations

Small variations in the background due to variations in sky transparency are sometimes present in OSCIR images. If no extended emission inherent to the source is present, the science target is masked out, and the background is fitted with a 2 dimensional polynomial using the skyfit.pro routine, developed by Dr. Robert Piña, and subtracted from the image. The subsequent product is then flux calibrated.

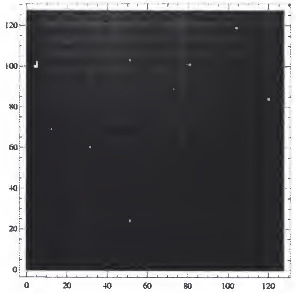

Figure 5-2: Image of the fully illuminated OSCIR array. Bright and black spots are pixels with significantly different responsivity than the rest of the array.

5.3 Image Artifacts

Occasionally, detector glitches may produce artifacts in the image. The most common artifact inherent in OSCIR images is nicknamed the "*Hammer Effect*". When a very bright mid-IR source is observed, the detector responsivity may change within the pixels that are hit by the high flux. This effect has been estimated to induce less than a 2% change in the total flux measured for a particular source. However, the Hammer Effect can create artificial structure in an image; it usually results in a sharp drop in flux for pixels which are read out subsequent to the pixel receiving the high flux. For example see Figure 5-3; a 10 μm image of the bright mid-IR source α Tau. In many cases the bright source also produces a small ghost image due to internal reflections as can be seen in the upper left of Figure 5-3**a**. The Hammer Effect can be predicted and corrected to some extent by fitting an exponential function to the observed flux and predicting the effect on subsequent pixels within the array. When possible, I used an IDL routine developed by Dr. Robert Piña to correct

OSCIR data for the Hammer Effect. A corrected image of α Tau is presented below in Figure 5-3b.

(a) (b)

Figure 5-3: The "Hammer" effect. 10 μm image of α Tau. **a**:The sharp drop of flux on the right side of the image is due to the Hammer Effect. The bright source on the upper left is an artifact produced by internal reflections. **b**:Partial correction for Hammer Effect.

Another instrumental artifact that rarely occurs involves transient dead pixels. OSCIR data is read out in 16 pixel blocks. Occasionally channel 8 of each block becomes insensitive. When this occurs, horizontal lines of dead pixels will appear on an image (Figure 5-4a). However, it is possible to use Fourier analysis to correct for this problem. First, the image is transformed to Fourier space (Figure 5-4b). Here all the dead pixels are grouped in a discrete location on the image. Usually, the bad pixels appear as high frequency structure in Fourier space, while the good data appears as low frequency structure. The bad pixels are then masked out and the image is cleaned by inverse transforming it back to data space (Figure 5-4c).

A final image "artifact" is produced when a mid-IR source is unexpectedly present in the sky beam. Chopping into the source will result in a negative image of the source in the final reduced data. The negative source's offset from the primary

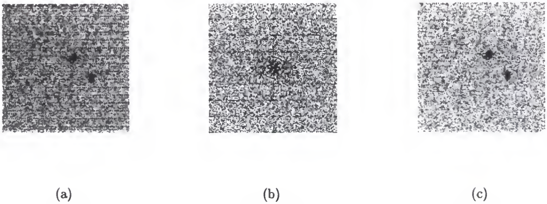
(a) (b) (c)

Figure 5-4: Channel 8 artifact. 18 μm image of RNO 1B+C showing artifacts removed with Fourier transforms. **a**:Image showing problem with channel 8. **b**: The same image transformed to Fourier space. **c**: After masking out the horizontal and vertical structure in image **b**, the image is cleaned by inverse Fourier transforming it back to data space.

target can be determined from its position on the array, and the chop direction can be changed to avoid placing the source in the sky beam. Figure 5-5 shows an image of the Herbig star V376 Cas, the Herbig star LkHα 198 is positioned in the reference beam and appears as a negative image on the reduced image.

5.4 Image Analysis Tools

All image analysis was performed using software written in IDL. The IDL software package provides many precompiled procedures for general statistical analysis of images. Dr. Robert Piña has also written much software that has been incorporated into the standard OSCIR data reduction package. In addition, I have written a few simple tools to measure fluxes and manipulate data. I discuss below the main analysis tools used with OSCIR data.

5.4.1 Gaussian Smoothing

Reduced data is sometimes smoothed by convolving it with a Gaussian function of width, N. The Gaussian smoothing operation will reduce the background

Figure 5-5: Chopping into a mid-IR source. Image of V376 Cas. In the lower left corner, a negative image of LkHα 198 is produced since it is positioned in the reference beam.

noise, and reduce the spatial resolution, but conserve the total flux. In particular, a Gaussian smoothing operation of width N, will reduce the standard deviation, σ, by a factor of $\sqrt{N}$. The width of the resulting PSF is a quadrature sum of the width of the unsmoothed PSF and the width of the Gaussian function; $S^2 = \mathrm{PSF}^2 + \mathrm{Gaussian}^2$. The mfilter.pro IDL routine was used to conduct the Gaussian smoothing. All contour maps of OSCIR data presented in this thesis have been Gaussian smoothed for clarity.

5.4.2 Histogram Tool

The interactive tool, histogram.pro, available in the OSCIR data reduction set, calculates the mean, median, sigma, and displays a histogram of the selected data. When an estimate of the 1σ level for a data set is required, the user selects an area of the background on the image and the tool displays a histogram of the data values and a table of the mean, median, and σ values.

5.4.3 Photometry Tools

As mentioned previously, an important consideration in analysis of mid-IR images is the width of the PSF. Multi-aperture photometry should be performed with the appropriate aperture size. For imaging data, two techniques are applied to conduct aperture photometry. In the case of an unresolved point source, the routine srcflux.pro, written by Dr. Robert Piña, estimates the sky background, and grows an aperture around a point source, until the increase in flux is equal to or less than the measured background flux. This technique was used to measure fluxes for flux calibration stars, PSF stars, and a few science targets which were unresolved.

Extended sources present a more complicated problem. For consistency, an aperture was chosen that would encompass at least 90% of the energy of a point source at the diffraction limit of the telescope/filter configuration. I developed a simple interactive tool, aphot.pro, which takes as an input the appropriate aperture size, and the flux calibrated image. The user selects the source on the image she wishes to measure, the tool calculates the midpoint of the source, and outputs the flux within the aperture. The tool also provides for interactive adjustment of the aperture location. The code for aphot.pro is listed in the Appendix.

5.4.4 FWHM tool

Measurements of the Full Width Half Maximum (FWHM) size of objects were needed to evaluate the seeing. FWHM is defined as the diameter of a source where the flux is equal to one half the maximum flux. The tool FWHM.pro, written by Dr. Robert Piña, determines the width of a source by measuring the peak flux and growing an aperture until it reaches a contour level that is equal to half of the peak flux.

CHAPTER 6
MID-IR IMAGES AND PHOTOMETRY

6.1 Imaging

Twenty-one different fields were imaged for this research, and 34 individual sources were detected. Some objects were only detected in one filter, and some fields contain more than one source. I show in Figures 6-14-6-19, flux calibrated 10 and 18 μm surface brightness maps of each object in the data set. The standard deviation for each image was derived as explained in Chapter 5. The lowest contour on all images is equal to 3σ and all contours are multiples of the 1σ value. Below I briefly discuss the morphology of each object. I obtained the most extensive and repeated observations of four core objects; HD 259431, AS 310, LkHα 234, and MWC 1080. I defer a detailed discussion of the results for these objects to Chapter 8. The results of the analysis presented in Chapter 8 will also be submitted for publication to the Astronomical Journal.

6.1.1 LkHα 198 and V376 Cas

The mid-IR observations show the binary recently detected by Lagage et al. (1993) at the position of LkHα 198 as well as a single mid-IR source at the position of V376 Cas. I find that the more southern component of the LkHα 198 binary is the brighter source in the mid-IR and observations by other authors indicate that it remains the dominant source in the near-IR also (Lagage et al. 1993; Leinert et al. 1997). The northern companion exhibits a silicate absorption feature indicating up to 35 magnitudes of extinction at V and a luminosity of $\sim$100 $L_\odot$ which implies it is also an Ae/Be star (Lagage et al. 1993). Comparison of the two objects to 10 and 18 μm PSF stars shows that both sources are unresolved; no extended emission is detected. Additional observations were conducted at the position of a millimeter source detected by Hajjar & Bastien (2000). I detect this source at 10 μm at a signal to noise of ~ 6. The source was not detected at 18.2 μm; however background levels were higher than at 10 μm and the observation did not achieve the same signal to noise level as the observation at 10 μm.

6.1.2 RNO 1 Complex

The RNO 1B region is found to contain at least three sources at 10 μm and an additional three at 18 μm. I identify two sources with the 3 μm DLIRIM 1 and DLIRIM 3 sources (weintraub et al. 1996). The near-IR sources RNO 1, RNO 1B, RNO 1C, and RNO 1F are also detected at 10 μm. One of the key questions concerning this region is the source of the outflow and the identity of the associated IRAS source. The IRAS Point Source Catalog (PSC) lists a mid-IR source, IRAS 00338+6312 located $\sim$40″ southeast of RNO 1 in the vicinity of RNO 1C. Several authors have suggested that this source is probably a luminous far-IR object, and that it powers the strong bipolar molecular outflow seen in this region (Yang et al. 1991; Snell et al. 1990). However the position of the IRAS source is almost 6″ offset from RNO 1C. Weintraub et al. suggest that it may instead be associated with another more deeply embedded source. My mid-IR images reveal several additional sources in this region which coincide with the locations of polarimetric peaks in Weintraub & Kastner's (1993) maps. In addition, near-IR imaging by Weintraub et al. (1996) shows that these peaks are associated with faint 3 μm sources.

The mid-IR source DLIRIM 1 is located near a radio continuum source, as well as a water maser (Weintraub et al. 1996). This object is positioned within 1.6″ of the PSC catalogue position of IRAS 00338+6312. DLIRIM 1 may be the source of the IRAS emission and the bipolar outflow. Far-IR mapping with sensitive instrumentation that will soon be available on SIRTF may help clarify the nature of this region, and reveal other deeply embedded sources.

RNO 1B and RNO 1C show very different profiles at 10 and 18 μm. RNO 1C appears more diffuse than RNO 1B and is clearly extended at 18 μm when compared with a PSF star (see Figure 6-1), while RNO 1B is not. The extended emission appears to be most prominent along a position angle of ~145 degrees. Neither object appears extended at 10 μm. RNO 1, which was only observed at 10 μm, exhibits no extended emission when compared to a PSF star.

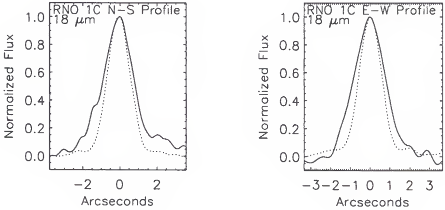

(a) (b)

Figure 6-1: The profile of RNO 1C at 18 μm. **a**: Profile along the N/S axis (solid line) compared to that of the point source, SAO 21609 (dotted line). **b**: Same as a, but along the E/W axis. All profiles have been smoothed by a Gaussian function of width 2 pixels.

6.1.3 XY Per

Multiwavelength (4-18 μm) observations of XY Per resolve the close binary at all wavelengths. No extended emission was apparent around this source. The small binary separation caused source confusion when photometry was conducted. In order to estimate the flux of each individual component, I first measured the flux within the core nine pixels of each component. I assume that these regions are relatively uncontaminated by flux from the neighbor star and that the ratio of these fluxes is equal to the ratio of the fluxes of the individual components. Individual fluxes were then estimated by measuring the total flux of the binary system, and using the ratio to solve for each star; FluxB $= \frac{Total}{1+ratio}$. In this case the southern source, component A, is brighter at all wavelengths except 4.8 μm. K band imaging by Pirzkal et al. (1997) shows that the northern source, component B, continues to dominate the flux at wavelengths shorter than 4 μm.

6.1.4 AB Aur

This well known archetype of the Herbig star class, shows no extended emission at 10, 18, or 20 μm in 3, 6, and 6 minute exposures respectively, at the IRTF. Since this object is relatively nearby (144 pc) most of the mid-IR emission must be originating from within the unresolved core within ~125 AU of the star. The source increases in brightness at longer wavelengths, rising from 0.66 magnitudes at 10 μm to -1.16 magnitudes at 20.8 μm, implying large amounts of cool dust. IRAS observations confirm this trend and show that the star continues to increase in brightness to -6.3 magnitudes at 100 μm (Hillenbrand et al. 1992). AB Aur is an excellent candidate for observation with the Gemini 8m telescope which will be able to resolve details within 0.7″ (~100 AU) of the star.

6.1.5 LkHα 25

This source, long suspected as a prime circumstellar disk candidate shows no sign of extended emission at either 10 or 18 μm in deep coadded 6.5 minute exposures from the IRTF and CTIO. Paradoxically, Margulis et al. (1989) find extended emission in IRAS 12 and 25 μm scans of this object. However, their identification may be questionable; the IRAS fluxes they cite are several orders of magnitude larger than what is observed for LkHα 25. Mid-IR photometry shows that the object's SED rises steeply from 10 to 18 μm. Hillenbrand et al. (1992) classified LkHα 25 as a

Group II source; these sources are expected to be more deeply enshrouded in dust, and thereby possess more dust emission than other classes of Herbig stars.

6.1.6 HD 97048

OSCIR mid-IR images have revealed a second, fainter, source ~35″ to the north of HD 97048. I identify this object with the near-IR source DENIS-P J1108.1-7738 which Cambrésy et al. (1998) suggest is a T Tauri star. Based upon Cambrésy et al.'s K flux and my N-band photometry, this source appears to have a declining mid-IR SED, similar to Hillenbrand Group I objects. Cambrésy et al. note that this object has also been detected by ISO in the LW2 and LW3 filters. This source could contribute to reports that HD 97048 itself exhibits extended emission (Prusti et al. 1994). HD 97048 shows no evidence of any extended emission at either 10 or 18 μm when compared to the PSF star PPM 370783. The northern companion was only observed at 10 μm, and is also an unresolved point source when compared to the PSF star.

6.1.7 HD 100546

HD 100546 appears as a bright compact source at 10, 11.7, and 18 μm. However, careful comparison with observations of point spread function stars shows that it is marginally extended with respect to a point source. Three 0.5 minute exposures were conducted of the point spread function star PPM 358988, in each wavelength cited above. HD 100546 was compared to each individual observation, and then to the final summed exposures for each wavelength. HD 100546 appears marginally extended in the east-west at 11.7 μm when compared with either the individual exposures of the 11.7 μm PSF star, or the coadded exposure. I show below (Figure 6-2) a line cut through the east-west axis of HD 100546 and the same for the summed exposure of PPM 358988. Measurements of the FWHM of HD 100546 (1.03″) and

PPM 358988 (0.84″) at 11.7 μm also show evidence of extended emission. Quadrature subtraction of these measurements yields the intrinsic source size at 11.7 μm; 0.60″, or ~60 AU.

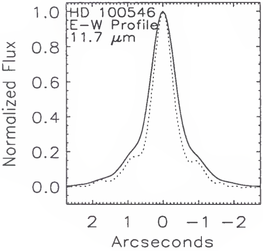

Figure 6-2: The profile of HD 100546 at 11.7 μm. Profile along the E/W axis (solid line) compared to that of the point source, PPM 358988 (dotted line).

HD 100546 is known to exhibit strong emission in the 11.3 μm PAH feature (Malfait et al. 1998). The slight extended emission present in the 11.7 μm image could be related to emission from the PAH grains. This emission could also be related to a circumstellar disk. Recent Hubble Space Telescope (HST) imaging (Grady et al. 2001) shows that this object possesses a disk with major axis along PA~137 degrees (Figure 6-3).

6.1.8 DK Cha

This deeply embedded (A_v= 11-17) young star shows no sign of extended emission when compared to a nearby PSF star. The object shows a nearly flat SED between 8 and 18 μm, in agreement with its classification as a Group II source. However, it is somewhat puzzling that no extended emission was detected, since Group II objects are expected to possess more dust than Group I objects. In addition,

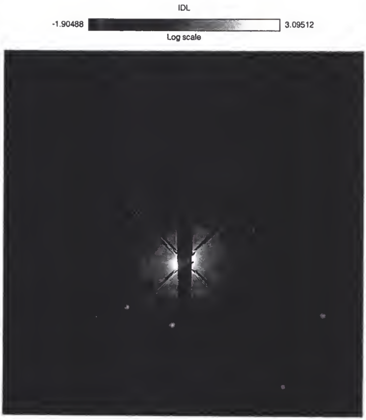

Figure 6-3: Detail of a broadband, optical (0.2-1.0 μm) coronagraphic image of HD 100546 obtained with HST STIS (Grady et al. 2001). The field of view extends ±12.5" from the star with the vertical coronagraphic image oriented at PA=17.35°. The STIS data reveal an inner disk with spiral dark lanes and outer radius≈350 AU, together with a diffuse envelope extending 1000 AU from the star and material apparently associated with DC 296.2-7.9. Six HH objects as well as a faint cloud of emission appear in the image as well. The large vertical and horizontal hatch marks are due to the coronagraph and the narrow X is an artifact of the PSF.

Li et al. (1994) find that in the near-IR Group II sources have extended emission more often than Group I objects. The object's nearby location (~200 pc), implies that the mid-IR emission originates within the unresolved core, within 120 AU of the star.

6.1.9 V 921 Sco

I find large scale extended emission at both 10 and 18 μm centered on the bright core star. Mosaicked images of the region show two arcs of emission encompassing the central star in a bubble. The northeast and southwest segments of the bubble are brightest, but fainter emission is visible connecting the segments. Several authors have noted that this object appears to be undergoing extensive mass-loss; arcs of emission attributed to this process have been detected in the optical and the mid-IR emission may result from similar processes (Hutsemekers & van Drom 1990). A bright companion star (V 921 Sco NE) is also located near the northeast segment. This source has no known counterpart in any published studies or catalogs of this region. The flux density of the primary star in this system declines between 10 and 18 μm, while that of the companion shows a rise towards longer wavelengths.

6.1.10 KK Oph

I marginally resolve the close companion of KK Oph at 10 μm. A line cut across a PA of ~248 degrees shows a broad shoulder that can be attributed to the companion (Figure 6-4a). In addition, I show below (Figure 6-4b) the PSF subtracted 10 μm image which clearly shows the second source, at a separation of 1.57″ and position angle of 248 degrees, in excellent agreement with measurements by Leinert et al. (1997).

KK Oph B is not resolved in the 18 μm image and PSF subtraction does not reveal the companion. However, the image is of sufficiently high signal to noise to apply an image deconvolution algorithm. I utilized a "Pixon" based algorithm called the "discrete multi-resolution method", developed by Dr. R. Piña and Dr. R. Puetter for deconvolution. A detailed discussion of Pixon deconvolution methods is presented in Puetter & Yahil (1999). Pixons are the smallest resolution elements of an image given the signal-to-noise of the data. The method works by modeling the input image as a set of Pixon elements with a level of noise associated with each element. The data model is convolved with the PSF of a point source to match the PSF of the input data. The data model is then compared to the input data and updated to obtain a closer agreement. The algorithm iterates until a minimum χ^2 solution is obtained for the data model. This method is dependent on the signal-to-noise of the data and the the quality of the PSF star observation. In this case the observation was of excellent quality and PSF was diffraction limited.

I show below the result of the deconvolution using PPM 295532 as the PSF star (Figure 6-5). The deconvolution was iterated for 15 cycles. The sources are now cleanly separated and I measure separations and position angles of 1.56″ and 246 degrees, in excellent agreement with all previous results. Since deconvolution conserves flux, this technique can also be used to determine the fluxes of each component of the system at both 10 and 18 μm. Utilizing this method I find that the ratio of the fluxes of the two objects remains fairly constant with respect to wavelength implying that they have similar spectral shapes, and thus are in the same evolutionary class; Group I.

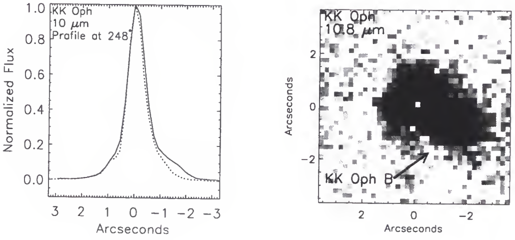

(a)

(b)

Figure 6-4: The KK Oph companion. (a) The profile of KK Oph at 10 μm. Profile along position angle of 248 degrees (solid line) compared to that of the point source, PPM 295532 (dotted line). (b) PSF subtracted 10 μm image of KK Oph. Compared with Figure 6-17 the close companion becomes clearly resolved.

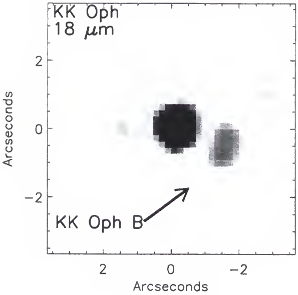

Figure 6-5: Deconvolved 18 μm image of KK Oph and companion star. A Discrete Multiresolution Method deconvolution routine was utilized and the result was obtained after 15 iterations.

6.1.11 MWC 297

The mid-IR maps show an arc of emission extending from the primary to a companion, MWC 297B, 24″ southwest. Since the companion is at the edge of the field I can only estimate a lower limit to its flux. I identify the companion with the optical source USNO 0825-12279170. This source can be seen on near-IR maps of the region (i.e. Testi et al. 1998; Henning et al. 1998), but has never been previously identified. This object may be associated with the H II region SH2-62. 18 μm observations also show extended emission associated with the primary, but the images do not include the region around the secondary. Additional mid-IR observations are needed of this nearby Herbig star to more completely map the dust emission.

6.1.12 Juggler Nebula/AFGL 2136

AFGL 2136 was observed at 10 μm on two separate nights. The exposures were then coadded to increase signal to noise. The 10 μm map shows a bright mid-IR source which I identify as AFGL 2136 IRS 1, using the terminology of Kastner et al. (1992). AFGL 2136 increases in brightness at 18 μm and exhibits large scale extended emission filling the entire field. AFGL 2136 is a multiple system in the near-IR, however none of the other components were detected. The 10 μm source is unresolved when compared to a nearby PSF star. As I will discuss in section 6.5, AFGL 2136's spectral index suggests an anomalous extinction law, with a value of total to selective extinction, R, greater than 3.1. High values of R can be caused by increases in grain size (Gorti & Bhatt 1993). Larger, micron-sized grains radiate more efficiently at 18 μm than at shorter wavelengths (Draine & Lee 1984). If the dust around AFGL 2136 contains a significant population of large grains, this could explain why the object shows extended emission at 18 μm, but not at 10 μm.

AFGL IRS1 shows a strong silicate absorption feature at 9.7 μm with an optical depth $\tau_{9.7\mu m} = 5.1$ (Willner et al. 1982). Assuming a ratio of $A_\nu/\tau_{9.7\mu m} \simeq 8$ (Kastner et al. 1992), the optical extinction to AFGL 2136 may be as much as 41 magnitudes. A possible m_R=15, optical counterpart to AFGL 2136 was noted by Lebofsky & Kleinmann (1976), but this source is offset by ~6″ from the position of AFGL 2136; additional deep optical imaging is needed to confirm any optical counterpart to this heavily extincted source.

6.1.13 BD +40 4124 Complex

Figure 6-18 shows contour maps of the three main sources in this region; BD +40 4124, V 1318 Cyg N/S, and LkHα 224. A new mid-IR source to the SE of BD +40 4124 is detected at 10 and 18 μm. This source is located within 2″ of two near-IR sources; Hillenbrand #19, and Hillenbrand #20 (= Palla #22) (Hillenbrand et al. 1995; Palla et al. 1995). Careful measurement of the offsets with respect to the centroid of BD +40 4124, places the source 5.4″ south, and 14.5″ east of the primary. Using the Hillenbrand et al. (1995) astrometry, this places the object at α(2000)~ 20:20:29.54, δ(2000) ~41:21:45.9. This is closest to Hillenbrand #20, which is the fainter of the two objects in the near-IR. Hillenbrand et al. (1995) suggest that this object may be a T Tauri star.

BD +40 4124 appears slightly extended at 18 μm when compared to a near-by PSF star. The extended emission is concentrated along the position angle 65-90 degrees and the source appears noticeably less extended at a position angle perpendicular to this axis. I show in Figure 6-6 profiles across the source at the two position angles and a comparison of the profile with a PSF star. Millan-Gabet (1999) notes that BD +40 4124 has a 0.72″ companion in the near-IR (he does not cite a position angle). I do not detect this source at either 10 or 18 μm in either raw or deconvolved images.

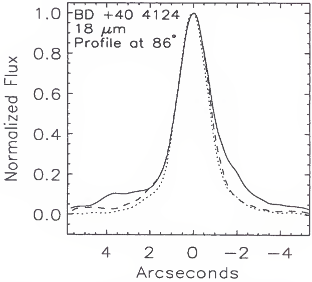

Figure 6-6: The profile of BD +40 4124 at 18 μm. Profile along position angle 86 degrees (solid line) compared to that of the point source, PPM 60925 (dotted line) and a profile along a position angle of 176 degrees, perpendicular to the angle of greatest extension (dashed line).

V 1318 Cyg is a triple system in the near-IR, however, a third, central member is not detected in the mid-IR (Aspin et al. 1994a). The southern source of this system is the brighter object in both the near and mid-IR, while the northern object becomes brighter at optical wavelengths (Aspin et al. 1994b). Neither V 1318 Cyg N/S or LkHα 224 are resolved when compared to a point source at either 10 or 18 μm. LkHα

224 does appear to show very faint, 3σ level, extended emission to the northeast, but this emission is only at the ~1% level when compared to the peak flux.

6.2 Photometry

Multi-aperture photometry was performed on the entire data set to ascertain how much of the mid-IR emission arises from the primary targets and other sources within the fields. Apertures were chosen to encompass at least 90% of the encircled energy at the respective wavelengths, taking into account the predicted PSF for the obscured aperture of each telescope configuration. Massey & Davis (1992) suggest that apertures should be chosen that are 4-5 times the FWHM of a stellar image. Assuming all mid-IR observations are close to diffraction limited at 10 μm and certainly diffraction limited at 18 μm, I find that the selected apertures agree well with Massey & Davis's criteria.

Uncertainties in mid-IR fluxes are always dominated by the effects of atmospheric transmission. Variations in atmospheric transmission are estimated at 10% for broad filters centered near 10 μm and 15% for longer wavelength filters such as the OSCIR 18.2 μm filter (van der Bliek et al. 1996). Narrow band observations are expected to be almost unaffected by variations in the atmospheric transmission; the above authors found variations of less than 1%. As discussed in Chapter 5, I find small variations for all narrow filters, except the M and 9.8 μm filters for which I estimate uncertainties of 15% and 10% respectively. I adopt uncertainties of 5% for all other narrow band filters.

Additional uncertainties include variations in fluxes due to positioning of the aperture, and statistical errors. Repeated measurements have show that these uncertainties are less than 1%.

Table 6-1: OSCIR and Literature Photometry

Name	V Mag	L Mag	N Jy	N Tot Jy	18 Jy	18 Tot Jy	12 Jy	25 Jy	1.3 mm Jy
LkHα 198 S	14.2	4.5	9.64	11.54	22.53	27.30	37.72	95.89	0.40
LkHα 198 N	...	4.5	1.63	11.54	5.14	27.30	37.72	95.89	0.40
LkHα 198-MM	...	...	0.01	0.01	...	...	...	...	0.25
V 376 Cas	15.6	4.1	19.56	21.04	33.88	37.34	34.21	88.16	0.23
RNO 1	14.2	7.7	0.52	0.52	0.95	1.01	2.50	22.4	...
RNO 1B[b]	18.7	6.4	1.24	2.05	1.51	5.37	[a]	...	0.79
RNO 1C[b]	...	6.5	0.78	2.05	2.33	5.37	[a]	...	0.58
XY Per A	9.8	5.2	2.19	3.91	1.69	3.23	3.93	4.04	...
XY Per B	10.7	...	1.73	3.91	1.54	3.23	3.93	4.04	...
AB Aur	7.05	3.5	20.65	22.89	25.68	26.97	28.95	49.78	0.43
HD 259431	8.7	4.5	6.08	8.50	6.18	10.31	12.78	20.38	...
LkHα 25	12.8	7.7	2.36	2.51	3.83	3.65	5.21	7.17	...
HD 97048	8.4	4.8	5.32	61.12	15.55	16.17	12.88	40.99	0.70
HD 97048 N	14.4[c]	...	1.20	1.45	...	...	...	...	...
HD 100546	6.7	4.0	45.73	56.06	124.97	134.50	65.78	242.60	0.69
DK Cha	18.7	2.9	32.48	36.93	54.27	55.81	39.30	85.60	0.50
V 921 Sco	11.7	2.4	27.52	48.26	15.96	25.00	124.21	313.45	0.27
KK Oph	11.5	4.1	8.75	9.77	10.65	10.40	10.00	9.56	0.05
MWC 297	12.3	1.2	98.27	120.70	93.74	116.43	159.00	224.00	0.11
AFGL 2136	15.0[d]	6.8	104.35	122.10	250.50	498.68	154.80	573.80	1.68
AS 310	12.5	7.4	2.83	11.82	15.05	47.97	51.46	97.60	0.20
BD +40 4124	10.6	5.0	5.38	7.78	15.67	168.65	[f]	...	4.00
BD +40 SE	...	...	0.09	7.78	0.12	168.65	...	...	...
LkHα 224[e]	14.1	4.9	8.20	31.93	10.82	71.96	[f]	...	4.00
V 1318 Cyg N[d]	18.6	7.0	2.63	31.93	6.23	71.96	65.29	109.18	4.00
V 1318 Cyg S[d]	19.2	5.2	17.02	31.93	50.50	71.96	65.29	109.18	4.00
LkHα 234	12.2	5.5	3.09	5.18	3.59	11.46	31.16	96.66	0.92
MWC 1080	11.5	3.1	13.20	17.10	11.77	14.76	22.78	25.13	0.54

V, L, IRAS, and millimeter photometry cited in the following references: Allen (1973), Aspin et al. (1994a), Berrilli et al. (1987, 1992), Breger (1974), Cohen (1972, 1973a, 1973b, 1974), Fouque et al. (1992), Fabricius & Markarov (2000), Hajjar & Bastien (2000), Hamann & Persson (1992), Henning et al. (1998), Herbst & Shevchenko (1999), Hillenbrand et al. (1992, 1995), Hughes et al. (1991), Kastner & Weintraub (1996), Kenyon et al. (1993), Lebofsky & Kleinmann (1976), Osterloh & Beckwith (1995), Perryman et al. (1997), Prusti et al. (1994), Rydgren & Vrba (1987), Staude & Neckel (1991), Thé et al. (1986), Weaver & Jones (1992), Whitelock et al. (1991).

[a] IRAS PSC position does not coincide with either of these objects, and probably pertains to a deeply embedded far-IR source.

[b] Other diffuse sources are present in 10 and 18 μm fields.

[c] I magnitude from Cambrésy et al. (1998).

[d] R magnitude of tentative optical counterpart (Lebofsky & Kleinmann 1976).

[e] LkHα 224, V 1318 Cyg N/S, and BD +40 4124 all in same mm beam.

[f] IRAS beam contains LkHα 224, V 1318 Cyg N/S, and BD +404124, V 1318 Cyg dominates the flux, but due to source confusion IRAS fluxes cannot be derived for the other sources.

I show in Table 6-1 the observed, uncorrected fluxes for the entire data set. Often, the sum of the fluxes for the components of a system do not exactly equal the total flux within the field. This is due to variations in the background, which may be non zero in areas of the image and very faint diffuse emission. In all cases the discrepancies are less than 2% and the fluxes agree within the uncertainties discussed above.

6.3 Color Corrections

Wide bandpass fluxes should be corrected for the spectral shape of the observed object. This color correction must be applied because the spectral shapes of the flux calibration star and the science object are different. The calibration star's SED peaks at short (optical) wavelengths characteristic of 3000-10000 K temperatures, while the science object's SED peaks at cool, 200 K temperatures in the mid-IR. Subsequently, integrating over the different spectral shapes will produce slightly different flux densities. Thus, the monochromatic flux depends on the spectral shapes of the observed source and the calibration star. The spectral shape of the science object must be known or assumed in order to compute the color correction. Color corrections for the wide OSCIR N filter assume a modified blackbody ($F_\nu = \tau\, B_\nu(T)$) for the SED of the science object and calculate a correction factor based upon the ratios of the monochromatic blackbody flux, and the bandpass integrated blackbody flux.

First, an effective wavelength is defined which corresponds to the wavelength of a photon possessing the average energy in the bandpass. The average energy is calculated as follows:

$$E_{av} = \frac{\Delta\nu}{\int (\frac{c}{\lambda^2}) * \frac{\lambda}{hc} * T_{Fil}(\lambda) * T_{Atm}(\lambda) d\lambda} \tag{6-1}$$

where E_{av} is the average photon energy in the bandpass, $\Delta\nu$ is the effective bandwidth, T_{Fil} and T_{Atm} are the filter and atmospheric transmission respectively, and h is the Planck constant. The effective wavelength is then defined as:

$$\lambda_{eff} = \frac{h * c}{E_{av}} \tag{6-2}$$

For the OSCIR N filter, λ_{eff}=10.46 μm.

The color correction factor assumes that ratio of the instrumental flux of the program object to that for the calibration star should equal the ratio of the number of photons at the wavelength of interest; $\frac{N_p}{N_*} = \frac{N_\gamma^p}{N_\gamma^*}$; N_p and N_* are the observed counts for the program star, and calibration star respectively, and N_γ^p and N_γ^* are the number of photons for the program star and calibration star respectively. For a particular wavelength, and temperature, T^p of the program star, N_γ^p and N_γ^* may be defined as follows:

$$N_\gamma^p = \frac{F_{\nu 0}^p}{B_{\nu 0}(T^p)} \int Q_{sys}^p \frac{B_\nu(T^p)}{h\nu} d\nu \tag{6-3}$$

$$N_\gamma^* = \int Q_{sys}^* \frac{F_\nu^*}{h\nu} d\nu \tag{6-4}$$

Where $F_{\nu 0}$ is the monochromatic flux, $B_{\nu 0}$ is the monochromatic flux of a blackbody at frequency ν, and Q_{sys} is the system quantum efficiency. Inserting these formulae into the ratio above, and solving for N_γ^p we have:

$$\frac{F_{\nu 0}^p}{B_{\nu 0}(T^p)} \int Q_{sys}^p \frac{B_\nu(T^p)}{h\nu} d\nu = \frac{N^p}{N_*} \int Q_{sys}^* \frac{F_\nu^*}{h\nu} d\nu \tag{6-5}$$

For a bandpass averaged flux density of the calibration star, $\bar{F}_\nu^*$;

$$\bar{F}_\nu^* = \frac{\int Q_{sys}^* \frac{F_\nu^*}{h\nu} d\nu}{\int Q_{sys}^* \frac{1}{h\nu} d\nu} \tag{6-6}$$

$$\therefore \int Q_{sys}^* \frac{F_\nu^*}{h\nu} d\nu = \bar{F}^* \int Q_{sys}^* \frac{1}{h\nu} d\nu \tag{6-7}$$

Finally, solving for the monochromatic flux of the program star we get:

$$F_{\nu 0}^p = N^p \frac{\bar{F}^*}{N^*} \frac{\int Q_{sys}^* B_{\nu 0}(T^p)/h\nu \, d\nu}{\int Q_{sys}^p B_\nu(T^p)/h\nu \, d\nu} \tag{6-8}$$

N^p is simply the observed counts of the program stars, and $\frac{\bar{F}^*}{N^*}$ is the calibration factor derived from observations of the flux calibration star. The remainder of the equation, $\frac{\int Q^*_{sys} B_{\nu 0}(T^p)/h\nu \, d\nu}{\int Q^p_{sys} B_\nu(T^p)/h\nu \, d\nu}$ is the color correction factor.

Table 6-2: Color Corrected N Band Flux Densities

Name	F_ν(Jy)	Name	F_ν(Jy)
LkHα 198 N	1.44	MWC 297	101.07
LkHα 198 S	9.02	AFGL 2136	97.27
V 376 Cas	19.13	AS 310	2.21
RNO 1	0.50	BD +40 4124	4.91
RNO 1B	1.26	BD +40 SE	0.09
RNO 1C	0.70	LkHα 224	8.25
XY Per A	2.26	V 1318 Cyg N	2.46
XY Per B	1.75	V 1318 Cyg S	15.27
AB Aur	23.25	LkHα 234	3.14
HD 259431	6.62	LkHα 234 NW	0.48
LkHα 25	2.74	MWC 1080	13.62
HD 97048	5.60	MWC 1080 A	9.66
DK Cha	36.73	MWC 1080 B	3.03
V 921 Sco	28.49	MWC 1080 East	0.57
KK Oph	9.98		

Hanner et al. (1984) found that for a broad 10 μm filter, corrections to the observed flux can be as much as 20%. I have used a simple MATHCAD program developed by Dr. Robert Piña to calculate color-correction factors for all N band photometry cited below. The program takes as input the uncorrected OSCIR broad-band N, and 18 μm fluxes of the program star. Using these two fluxes and a power law for the extinction law, it first estimates a temperature (T^p) for the object. The method for calculating the temperature from the two fluxes will be discussed in detail in Chapter 7. The program then calculates the ratio of the monochromatic blackbody flux at the effective wavelength to the bandpass integrated blackbody flux and solves for the color-correction factor (Equation 6.8). I list in Table 6-2 the color corrected N band flux densities for each object. I find that most corrections were 3% or less, five objects had corrections of order 10% (RNO 1C, HD 97048, AFGL 2136, V 1318 N and S), AS 310 had a correction of order 22%, and the very embedded companion to LkHα 234 had a large, 34% correction. All corrections to narrow band flux densities were negligible, and less than 1%.

6.4 Origin of IR Excess

Mid-IR imaging has revealed that more than half of the sample listed in Table 4-2 (11/21 objects) possesses extended mid-IR emission or embedded companions that contribute significantly to the mid-IR flux. Three additional sources (RNO 1C, HD 100546, BD +40 4124), appear extended when compared to the PSF of a mid-IR point source, and KK Oph has a known close companion that is marginally resolved in my mid-IR image (Figures 6-1, 6-2, 6-6, 6-4). The contribution of extended emission and embedded companions to the mid-IR emission ranges from 12% to 73% for the resolved sources (excluding HD 97048, HD 100546, KK Oph, and BD +40 4124).

I show below in Table 6-3 the percentage of the total emission that originates outside an aperture enclosing the primary star in the fields surveyed. Primary stars in this case are considered the brightest objects in the field and are in all cases the brighter object at optical wavelengths. For MWC 1080 the flux excess is shown for an aperture enclosing the unresolved binary and for an aperture enclosing only component A of the binary. In column three I also indicate whether the excess originates in companions (c), or extended emission (e).

Flux excesses were comparable at 10 and 18 μm for most objects except RNO 1B, which has numerous companions at 18 μm, AFGL 2136, which was not resolved at 10 μm, and LkHα 234, whose companion dominates the flux at $\lambda > 12$ μm. On average 40% of the mid-IR flux in the fields originates in companions or extended emission. The contributions from embedded companions and dusty envelopes average ~18% and ~22% respectively. The excess flux is dominated by emission from large-scale dust envelopes for the stars HD 259431, V 921 Sco, MWC 297, AS 310, and

AFGL 2136. For all other objects the excess flux is dominated by emission from embedded companions. Embedded companions had been considered previously as the source of some of the IR excess, however, observations by Li et al. (1994) showed that the emission from companions makes a negligible contribution to the total near-IR flux. Li et al. also found that Hillenbrand Group II objects tended to have extended emission more frequently than Group I objects in the near-IR. I find the opposite trend in the mid-IR; of the seven objects with large-scale extended emission (HD 259431, V 921 Sco, MWC 297, AS 310, AFGL 2136, LkHα 234, MWC 1080) only two fall into the Group II class. Of the 10 objects in Table 6-3 which have companion stars, only three fall into Hillenbrand's Group II class. Despite the expectation that Group II objects should be more enshrouded in dust and show more evidence of dusty envelopes and dust related phenomena, the opposite appears to be true in this small sample.

Table 6-3: Percentage of Mid-IR Flux External to Primary Star

Name	N %	18%	Note	Name	N%	18%	Note
LkHα 198 S	14	19	c	AFGL 2136	...	50	e
RNO 1B	40	72	ce	AS 310	76	69	ce
XY Per A	44	48	c	V 1318 Cyg S	13	11	c
HD 259431	28	40	e	LkHα 234	40	69	ce
V 921 Sco	50	65	ce	MWC 1080	23	20	ce
MWC 297	19	20	ce	MWC 1080 A	42	43	ce

Columns two and three show the percentage of the mid-IR emission at 10 and 18 μm that originates outside an aperture which sould contain 90% of the flux of a point source. Column four indicated whether the mid-IR emission originates in embedded companions (c), or extended emission (e).

Clearly much of the mid-IR emission previously attributed to disk processes originates in external sources. The new photometry changes the evolutionary class of seven objects, and I classify for the first time an additional seven objects. I have detected new mid-IR companions near the stars LkHα 198, RNO 1B, HD 97048, V 921 Sco, LkHα 234, MWC 1080, MWC 297, AS 310, and BD +40 4124. Several other objects in the sample were known binaries for which I show spatially resolved mid-IR photometry for the first time. Positions and separations of these companions and previously known IR companions are listed in Table 6-7. As I will discuss in Chapters 7 and 8, for some objects, HD 259431, AS 310, and V 921 Sco, there is strong evidence that transiently heated grains, such as PAHs, are responsible for much of the mid-IR emission. I note that for most of my sample the total mid-IR fluxes within the OSCIR field of view are less than the IRAS fluxes for similar passbands. This suggests that yet more objects and/or extended emission are detected by IRAS, yet lie outside the OSCIR field of view. These regions need to be thoroughly mapped to determine the origin of all the emission detected by IRAS.

6.5 Mid-IR SEDs

Mid-IR SEDs have been compiled for select objects for which extensive narrow band observations were obtained. I present here the first high-spatial-resolution SEDs for XY Per A, XY Per B, DK Cha, V921 Sco, V 1318 Cyg N and V 1318 Cyg S. Mid-IR photometry for these objects is shown in Tables 6-4 and 6-1. Additional SEDs for HD 259431, AS 310, LkHα 234, and MWC 1080 are discussed in detail in Chapter 8.

6.5.1 XY Per A/B

My 4-18 μm observations resolve this binary system and show that the western component dominates the emission until 4 μm when the eastern component becomes the brighter object (Figure 6-7). The system is composed of an A2 II star (the western component) and a B6 V star (the eastern component) both of which are suspected to be variables (Melnikov & Ezhkova 2000). The system as a whole varies by as much as 1 magnitude at optical wavelengths (Melnikov & Ezhkova 2000).

The eastern component continues to be the brighter source in the near-IR; Pirzkal et al. (1997) states that the pair are of nearly equal brightness at 2.2 μm, but cites a position angle indicating that the eastern component is the primary. However, at optical wavelengths the western component is the brighter object (Fabricius & Makarov 2000). The pattern of being optically dimmer, yet brighter in the near-IR and dimmer in the mid-IR is somewhat puzzling. It is possible that an emission feature enhances the flux of the eastern component in the 2-4 μm regime. The system is known to exhibit 3.29 μm PAH emission (Brooke et al. 1993), but it is unknown in which of the components the emission originates. Alternatively, variability might explain why the eastern component appeared brighter in the 2-4 μm regime at the time of the observations.

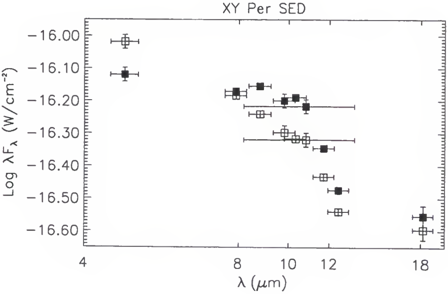

Figure 6-7: SEDs for the A (filled square) and B (open square) components of the XY Per system. Error bars on the abscissa indicate the width of the filters, error bars on the ordinate axis are comparable to the size of the data points.

The mid-IR SED of XY Per A shows a large feature centered around 9.8 μm which I attribute to silicate emission while the SED of XY Per B is relatively smooth. A similar feature is seen in an SED of the system as a whole (Cohen 1973a). Hanner et al. (1998) do not detect this feature, but claim to have detected a 11.2 μm emission feature which they attribute to PAH grains. The 11.2 μm feature does not show up in the mid-IR SEDs of either XY Per A or XY Per B, probably due to the lower spectral resolution. In addition, Hanner et al.'s spectroscopy utilized a 3.4″ aperture which included emission from both components of the system, thus it is unknown in which object the 11.2 μm feature originates.

6.5.2 DK Cha

This heavily embedded object ($A_v \sim$ 11-17) shows a silicate absorption feature in its SED (Figure 6-8) in agreement with IRAS spectra (Figure 6-9) (Graham & Chen 1991a). DK Cha exhibits large variations in color indicating up to 8 magnitudes of variability in extinction; possibly due to orbiting dust clouds (Hughes et al. 1991). Since the extinction towards DK Cha is very poorly known I have not dereddened the mid-IR observations. Graham & Chen (1991a) note that DK Cha exhibits variability in the near-IR of up to 0.8 magnitudes. My N band photometry also indicates some variability; I find an N magnitude of 0.16, compared to Graham & Chen's N magnitude of -0.20. More extensive high spatial resolution observations are needed of this object to encompass the full wavelength range of its mid-IR SED and to confirm any mid-IR variability.

6.5.3 V 921 Sco

V 921 Sco's observed SED (Figure 6-11) appears relatively flat. However, IRAS spectra (Figure 6-10) show strong emission from PAH grains at 7.7, 8.6, and 11.3 μm as well as an emission feature at 12.8 μm due to [Ne II] (Jourdain de Muizon et al. 1990). Recent higher spectral resolution ISO spectra also show these features (Van Kerckhoven et al. 2000). However, my low resolution mid-IR SED does not show these features. Because this region contains another bright mid-IR source to the northeast of V921 Sco, it is possible that the PAH feature originates in this object rather than the primary. It is essential to obtain spatially resolved spectroscopy of

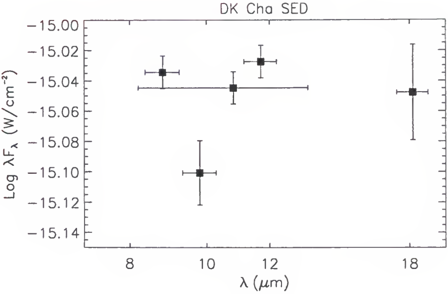

Figure 6-8: Mid-IR SED of DK Cha. Error bars on the abscissa indicate the width of the filters, error bars on the ordinate axis are uncertainties in mid-IR fluxes which range from 5% to 15%.

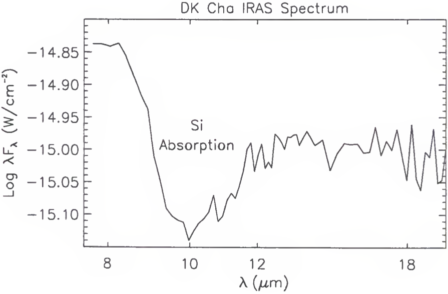

Figure 6-9: IRAS spectrum of DK Cha showing the silicate absorption feature.

all sources in this field to determine which object is the source of the PAH emission.

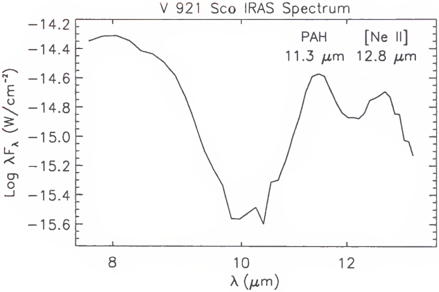

Figure 6-10: IRAS spectrum of V 921 Sco showing the 11.3 μm PAH feature.

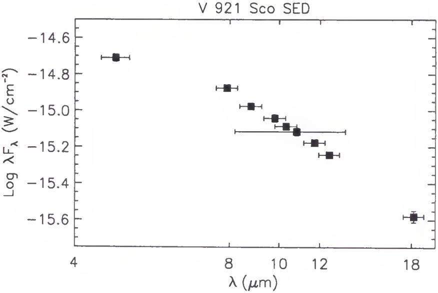

Figure 6-11: Mid-IR SED of V 921 Sco. Error bars on the abscissa indicate the width of the filters, error bars on the ordinate axis are comparable to the size of the data points.

6.5.4 V 1318 Cyg N/S

I show the first spatially resolved mid-IR SEDs of the two components of V 1318 Cyg (Figure 6-12). Both ISO and ground-based observations indicate a

10 μm absorption feature for this system (van den Ancker et al. 2000b; Aspin et al. 1994a). My photometry of the two sources indicates that both objects possess this feature. The feature is of comparable strength in both sources, but the central wavelength appears to be slightly shifted. In the brighter mid-IR source, V 1318 S, the deepest absorption occurs within the 10.3 μm filter, while in V 1318 Cyg N, it occurs within the 9.8 μm filter. V 1318 Cyg S is the more luminous and more embedded of the two objects. Laboratory experiments have shown that increases in particle size or changes in chemical composition can shift the silicate feature to longer wavelengths (Hanner et al. 1994b; Lynch & Mazuk 2000). It is possible that the two objects have somewhat different grain environments, possibly influenced by their respective evolutionary stages. Mid-IR spectroscopy of the two components is essential to confirm this feature in their SEDs. Finally, I find a large offset between my N band photometry and that of Aspin et al. (1994a) for V 1318 Cyg S (0.63 and -0.7 magnitudes respectively). Strom et al. (1972) also show discrepant N band magnitudes (-0.2 and 0.4). I tentatively suggest that these discrepant measurements could be due to mid-IR variability. V 1318 Cyg is known to be an optical variable, but the nature of its variability in the infrared has not yet been explored (Ibragimov et al. 1988).

Table 6-4: Narrow Band Photometry

	Flux Density (Jy)						
Name	M	7.9	8.8	9.8	10.3	11.7	12.5
XY Per A	1.215	1.778	2.054	2.064	2.220	1.761	1.399
XY Per B	1.533	1.768	1.686	1.648	1.657	1.436	1.201
HD 100546	...	...	...	...	...	56.662	...
DK Cha	...	...	27.100	25.905	...	36.619	...
V 921 Sco	31.166	34.928	30.937	29.612	28.067	25.951	23.832
V 1318 Cyg N	...	3.351	2.062	2.095	2.340	3.556	5.507
V 1318 Cyg S	...	22.796	18.462	14.708	14.536	22.691	37.030

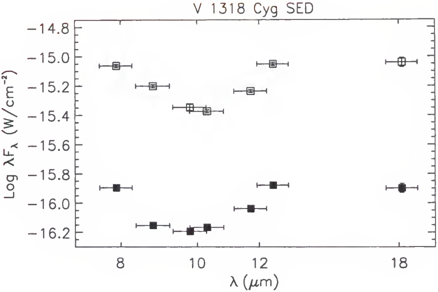

Figure 6-12: Mid-IR SEDs for the north (filled squares) and south (open squares) components of the V 1318 Cyg system. Error bars on the abscissa indicate the width of the filters, error bars on the ordinate axis are comparable to the size of the data points.

6.6 Spectral Indices

As discussed previously, both Lada and Hillenbrand have devised a classification scheme for pre-main-sequence stars which is based upon the slope of their SEDs. Lada's classification system was originally based upon observations of T Tauri stars, while Hillenbrand's was established specifically to classify Herbig star SEDs. These indices divide the objects into evolutionary classes which are related to the source of their infrared emission. Specifically, Group II objects are expected to have flat indices, $\alpha \sim 0$, and large infrared excesses due to dusty envelopes. These objects are believed to be the youngest and most embedded. Group I objects are expected to be more evolved, to have lost most of their dust envelopes, and to have declining indices, $\alpha \sim 0.65$ due to dusty circumstellar disks. The most evolved objects, Group III sources, have little if any IR excesses due to free-free emission from cool gas left after the disk has dissipated. I have compiled 3 μm fluxes from the literature for each object in my data set. Using these fluxes, and my own 10 μm photometry, I have calculated the Hillenbrand spectral indices from the dereddened 3 and 10 μm fluxes. Indices were calculated for 27 objects, including the core of MWC 1080, and its separate components, MWC 1080 A, and MWC 1080 B. Uncertainties in the spectral indices were estimated to be ±0.05, much smaller than the width of the bins, based upon 5% uncertainties in the L fluxes and 10% uncertainties in the 10 μm fluxes. Table 6-5 shows the indices for the entire data set and Figure 6-13 shows a histogram of the indices divided into bins of 0.25.

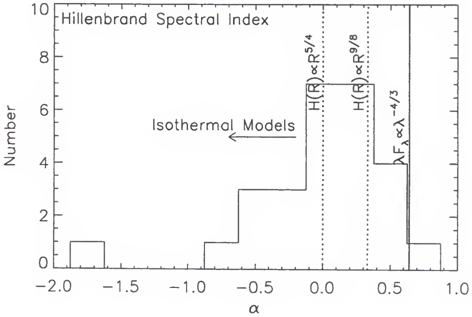

Figure 6-13: Histogram of Hillenbrand spectral indices for the 27 object sample. The solid vertical line marks the index expected from a optically thick, geometrically-thin disk. The dashed vertical lines show the indices expected from flared disks with two different scale heights in the model of Kenyon & Hartmann (1987). Isothermal dust distributions are expected to have negative indices as marked by the arrow.

The primary peak of the histogram occurs at $\alpha \approx 0.25$ and a wide shoulder is located at $\alpha \approx$-0.4. The slope predicted for a flat, optically thick disk is indicated by a vertical line. The unusually cool object, AFGL 2136, has an extremely steep index, and lies far to the left of all other objects. The location of this object suggests that the extinction law may be anomalous. I adopted the Kastner et al. (1992) relationship for extinction and optical depth, $A_v/\tau_{9.7\mu m} \simeq 8.0$; smaller values than this would create an even more extreme spectral index. However, Rieke & Lebofsky (1985) have shown that $A_v/\tau_{9.7\mu m}$ can be as much as 24 assuming a ratio of total to selective extinction, R=3.1. In addition, there is some indication that R may be larger in dense, dusty, star forming regions (Mathis 1990; Gorti & Bhatt 1993). Either of these effects would move AFGL 2136's spectral index closer to the indices of other Group II objects in the distribution.

Table 6-5: Hillenbrand Spectral Indices

Name	$\alpha_{3/N}$	$\alpha_{N/18}$	SED Shape
LkHα 198 N	0.88	-0.22	min
LkHα 198 S	0.11	-0.09	min
V 376 Cas	0.00	0.02	flat
RNO 1	0.13	0.01	...
RNO 1B	0.30	0.24	fall
RNO 1C	0.45	-0.15	min
XY Per A	0.53	0.36	fall
XY Per B	0.63	0.30	fall
AB Aur	0.23	0.14	fall
HD 259431	0.36	0.24	fall
LkHα 25	-0.48	0.07	...
HD 97048	0.26	-0.23	min
HD 100546	-0.36	-0.21	rise
DK Cha	0.19	0.06	...
V 921 Sco	0.47	0.50	fall
KK Oph	0.38	0.17	fall
MWC 297	0.37	0.28	fall
AFGL 2136	-1.73	0.31	...
AS 310	-0.52	-0.46	rise
BD +40 4124	0.24	-0.20	min
LkHα 224	0.15	0.26	fall
V 1318 Cyg N	-0.23	-0.07	rise
V 1318 Cyg S	-0.32	-0.16	rise
LkHα 234	0.16	0.19	fall
MWC 1080	0.54	0.33	fall
MWC 1080 A	0.56	0.29	fall
MWC 1080 B	-0.06	0.18	...

Using a broad qualitative description of the Hillenbrand classes, all negative index and flat index sources would fall into Hillenbrand's Group II, and all positive index sources would be classified as Group I, which should have indices similar to that expected from a geometrically-thin disk. I show in Table 6-6 the new Hillenbrand classes for seven objects for which these indices had never before been derived. I also determined contradictory classes for seven objects that were previously classified in the Hillenbrand system. Five of these objects are members of binary systems, which when resolved exhibit different SED slopes than the unresolved system.

Table 6-6: New or Changed Hillenbrand Groups

Name	Group	Name	Group
LkHα 198 N	I	DK Cha	I
LkHα 198 S	I	AFGL 2136	II
RNO 1	I	AS 310	II
RNO 1B	I	V 1318 Cyg N	II
RNO 1C	I	V 1318 Cyg S	II
XY Per A	I	MWC 1080 A	I
XY Per B	I	MWC 1080 B	II

Almost all objects in my sample show substantially flatter slopes than expected from the simple thin disk model. However, the dominant peak of this distribution is very suggestively near the values expected from flared disks in the model proposed by Kenyon & Hartmann (1987). I mark on Figure 6-13 the indices expected from flared disks with two different scale heights. The temperature distribution of a flared disk depends upon both an internal temperature distribution, and the degree of flaring. Assuming an internal temperature distribution similar to that of a flat disk, T(R)$\propto$ $R^{-3/4}$, the disk surface height is characterized by H(R)$\propto$R$^{9/8}$. Disks with temperature distributions that decrease less rapidly, such as T$\propto$ $R^{-1/2}$ have larger degrees of flaring, and the disk surface height is H(R)$\propto$R$^{5/4}$. Temperature distributions that decrease slower than T$\propto$R$^{-1/2}$ imply isothermal dust distributions, such as a spherical dust envelope. Kenyon & Hartmann have shown that disk inclination will also contribute to the SED slope to a small degree; the mid to far-IR flux is expected to be diminished for disks at large inclination angles. However, disk flaring should be the dominant factor defining the spectral index.

These spectral indices can constrain disk models of the IR excess. The classical disk model, which is characterized by zero flaring, and $\lambda F_\lambda \propto \lambda^{-4/3}$, can be excluded since it lies outside the broad peak of the spectral indices distribution. Assuming the mid-IR emission originates in a flared disk, the photometry can constrain the scale height of this model. The broad histogram peak encompasses both the $R^{5/4}$ and $R^{9/8}$ scale heights and suggests that the degree of disk flaring lies between these two models.

Objects with negative indices have SEDs that are rising towards long wavelengths, indicating increasing fluxes. No correlation is found with millimeter flux; these objects include non-detections, such as LkHα 25, as well as bright millimeter sources such as AFGL 2136. Negative index sources also include some of the oldest and youngest objects for which there are age estimates. Two interpretations of these SEDs are possible; these objects could have a deficit of near-IR emission due to disk clearing, alternatively, they could possess an excess of 10 μm flux due to a dust envelope. This problem can be explored by calculating the 10 to 18 μm spectral indices. If an object exhibits a slope that continues to rise towards 18 μm it seems likely that the origin of the emission lies in a cool dusty envelope. When these indices are analyzed in conjunction with the 3 to 10 μm index, a rough idea of the form of the entire near to mid-IR SED is obtained. I show below in Table 6-5 the 3 to 10 μm and 10 to 18 μm spectral indices.

Most of the objects in my sample exhibit three main SED shapes; the SED falls consistently from 3 to 18 μm, the SED rises consistently from 3 to 18 μm, and the SED shows a minima at 10 μm. I note in Table 6-5 which shape the SED exhibits for each object.

The majority of objects, all classified as Group I, show a falling SED which could be attributed to a flared disk. No correlation is found with either millimeter flux or age.

Five objects, all classified as Group I, show a minima at 10 μm. If these objects had been classified on the basis of their N/18 μm indices they would be identified as Group II sources. Since only BD +40 4124 and HD 97048 have age estimates no correlation can be examined between age and the SED minima. Both BD +40 4124 and RNO 1C show extended emission at 18 μm on a scale of a few arcseconds. If this minima is interpreted as disk clearing, high-spatial-resolution imaging might show additional structure, such as a minima in the flux distribution.

All objects showing rising SEDs fall into the Group II class. These objects include V 1318 Cyg, and AFGL 2136 which have the largest millimeter fluxes in the sample, and also AS 310, which has a moderate millimeter flux. The fact that all of these sources are millimeter detections indicates that this set of objects possesses additional cool material at large distances from the star. Although Group II objects are believed to be less evolved than Group I objects, age does not appear to be correlated with SED shape in this set of objects; HD 100546 shows a rising SED, yet it is one of the oldest objects in the sample, while AFGL 2136 may be the youngest object in the sample.

Six objects, V 376 Cas, RNO 1, LkHα 25, DK Cha, AFGL 2136, and MWC 1080B, show ambiguous or unusual SEDs. V 376 Cas exhibits a flat SED throughout the 3 to 18 μm regime; this object could be enclosed within an opaque spherical shell of dust thereby hiding any flux variations. RNO 1 and DK Cha exhibit SEDs which fall to 10 μm then are flat to 18 μm. If classified by their N/18 μm indices these objects would fall into the Group II class rather than Group I. These SEDs could be interpreted as objects with flared disks enclosed within an optically thin envelope of cooler dust that provides the 18 μm flux. AFGL 2136 shows an SED that peaks at 10 μm, and then falls to 18 μm. As explained previously, the extinction towards this object is very uncertain, and there is some evidence for an anomalous extinction law with R>3.1. The SED, uncorrected for reddening, shows a steep rise from 3 μm to 10 μm and then flattens somewhat, but continues to rise towards 18 μm. However, since AFGL 2136 is reddened by at least 41 magnitudes of extinction, the form of the extinction law can greatly alter the shape of its SED; until a better estimate of the extinction in this region is available, it is not possible to interpret the SED of AFGL 2136.

MWC 1080B shows an SED that is flat between 3 and 10 μm, and then falls towards 18 μm. The MWC 1080 A/B system is known to include a close, eclipsing binary. Many researchers have shown that a close binary can truncate a dust distribution and disperse any material exterior to its orbit. I suggest that MWC 1080B may possess an optically thin dust envelope that is truncated by the companion. Since the period of the eclipsing binary is only 2.9 days, a high-spatial-resolution variability study, utilizing adaptive optics could easily determine which of this pair of objects possesses the eclipsing binary companion and resolve this question. The SED of LkHα 25 is difficult to interpret. It exhibits a rising SED, which flattens out between 10 and 18 μm. This object is not detected in millimeter continuum surveys (Henning et al. 1998), and unlike other Group II objects may be devoid of material in the outer regions of its circumstellar environment. Fuente et al. (1998) suggest that it may be located within a cavity in its local circumstellar environment created by the progressive dispersal of gas. Fuente et al. propose an older evolutionary class for LkHα 25, based upon their millimeter observations.

I find that the Hillenbrand 3/10 μm spectral index, determined from low-resolution photometry does not clearly determine the geometry or evolutionary stage of Herbig star environments. There is no clear correlation between evolutionary class determined from the 3/10 μm index and age of the star. However, an examination of the shape of the SED between 3 μm and 18 μm provides additional information concerning the geometry of the dust in Herbig star environments and gives clues as to their evolutionary stages.

High-spatial-resolution imaging reveals the architecture of the circumstellar environments and results in the reclassification of several objects. Newly determined spectral indices appear to exclude the classical optically thick, geometrically-thin disk model, but may constrain the scale heights of more realistic models, such as the flared disk models. The new spectral indices which are derived from photometry which excludes non-disk sources of emission, support the proposal that at least some of the unresolved mid-IR emission, may still originate in a disk. However, imaging clearly shows that the circumstellar environments can also include large-scale envelopes and embedded companions which were not resolved in previous studies.

6.7 Embedded Companions

Most researchers agree that pre-main-sequence stars have a higher percentage of multiple or binary systems than main sequence stars (Ghez et al. 1997; Leinert et al. 1993). Some authors estimate that the degree of multiplicity among T Tauri systems is at least twice that for main sequence stars (Leinert et al. 1997; Ghez et al. 1993a). However, the actual percentage of systems with companions is controversial. Studies of T Tauri stars have found that between 40% and 60% of objects have companions within a given radial distance (Ghez et al. 1993b; Leinert et al. 1993). The frequency of companions may vary with the age of the systems, and with the wavelength of the observations; some very young companions will be invisible at optical wavelengths and bright in the infrared. Ghez et al. (1997) suggest that the frequency of infrared companions may be slightly higher than found in optical surveys.

A few small studies have been conducted on samples of Herbig stars. Leinert et al. (1997) examined the binary frequency within 3600 AU of a small sample of Herbig stars; they find a binary frequency of up to ~42%, while the expected frequency for companions around main sequence stars within the same radial distance is ~18% (Duquennoy & Mayor 1991). A study of T Tauri stars, using similar instrumentation and examining the same range of separations also found a binary fraction of up to 42% (Leinert et al. 1993). Herbig star systems exhibit a large excess of companions

Figure 6-14: Surface brightness of LkHα 198, LkHα 198 mm, V 376 Cas, and RNO 1. Lowest contour is 3σ. Contour levels are as follows: LkHα 198 N: 3, 10, 20, 100, 1000, 2000σ ($1\sigma \approx 2.1$ mJy arcsec^{-2}), LkHα 198 18 μm: 3, 10, 100, 500σ ($1\sigma \approx 14$ mJy arcsec^{-2}), LkHα 198 mm N: 3, 4, 100, 300σ ($1\sigma \approx 1.97$ mJy arcsec^{-2}), V376 Cas N: 3, 10, 100, 1000σ ($1\sigma \approx 2.5$ mJy arcsec^{-2}), V 376 Cas 18μm: 3, 10, 100, 500σ ($1\sigma \approx 18.2$ mJy arcsec^{-2}), RNO 1B N: 3, 6, 10, 100, 200σ ($1\sigma \approx 3.0$ mJy arcsec^{-2}), RNO 1B 18μm: 3, 5, 10, 30σ ($1\sigma \approx 10.4$ mJy arcsec^{-2}) All images Gaussian smoothed by 3 pixels.

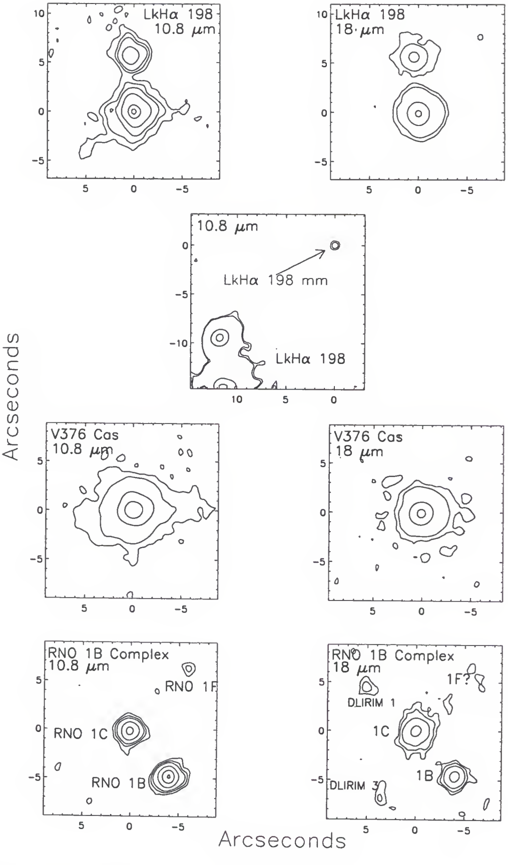

Figure 6-14: Surface brightness of LkHα 198, LkHα 198 mm, V376 Cas, and RNO 1

Figure 6-15: Same as Figure 6-14 for RNO 1, XY Per, AB Aur, and HD 259431. RNO 1 N: 3, 10, 50, 100σ (1σ $\approx$2.3 mJy arcsec^{-2}), RNO 1 18μm:3 , 5, 10σ (1σ $\approx$20.7 mJy arcsec^{-2}), XY Per N:3 , 10, 25, 100, 200, 250, 300σ (1σ $\approx$3.1 mJy arcsec^{-2}), XY Per 18 μm: 3, 10, 25, 30, 35σ (1σ $\approx$18 mJy arcsec^{-2}), AB Aur N: 3, 10, 100, 1000, 3000σ (1σ $\approx$2.6 mJy arcsec^{-2}), AB Aur 18 μm: 3, 10, 100, 500σ (1σ $\approx$8.7 mJy arcsec^{-2}), HD 259431 N: 3, 10, 20, 100, 1000, 2000σ (1σ $\approx$1.5 mJy arcsec^{-2}), HD 259431 18μm: 3, 5, 10, 25, 100, 200σ (1σ $\approx$7.2 mJy arcsec^{-2}) RNO 1, XY Per, AB Aur, HD 259431 smoothed by 3, 2, 3, 3 pixels respectively.

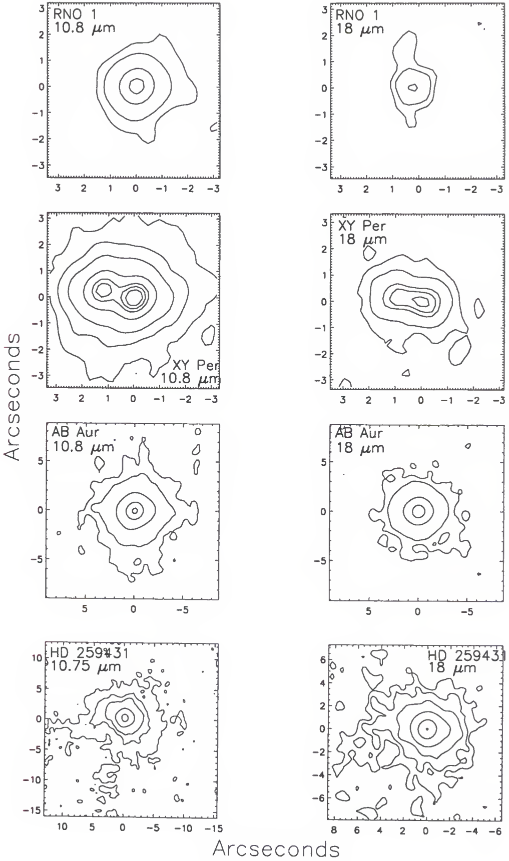

Figure 6-15: Same as Figure 6-14 for RNO 1, XY Per, AB Aur, and HD 259431.
RNO 1

Figure 6-16: Same as Figure 6-15 for LkHα 25, HD 97048, HD 97048 N, and HD 100546. LkHα 25 N: 3, 10, 100, 500σ (1σ $\approx$1.3 mJy arcsec^{-2}, LkHα 25 18 μm: σ 3, 10, 50, 75σ (1σ $\approx$12.2 mJy arcsec^{-2}), HD 97048 N: 3, 10, 100, 300σ (1σ $\approx$6.2 mJy arcsec^{-2}), HD 97048 18 μm: 3, 10, 20, 50, 100σ (1σ $\approx$49 mJy arcsec^{-2}), HD 97048N N: 3, 10, 50, 80σ (1σ $\approx$5.9 mJy arcsec^{-2}), HD 100546 N: 3, 10, 200, 1000σ (1σ $\approx$5.5 mJy arcsec^{-2}), HD 100546 18 μm 3, 10, 100, 500σ 1σ $\approx$30.7 mJy arcsec^{-2}). All images smoothed by 3 pixels.

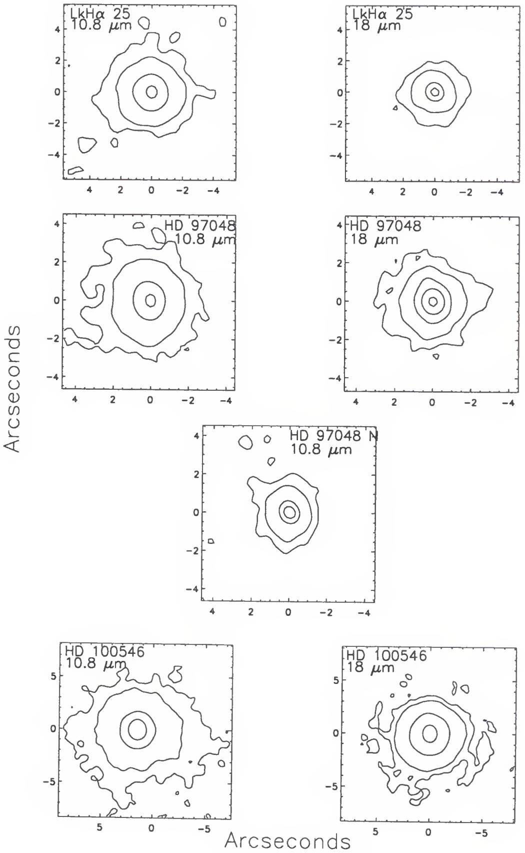

Figure 6-16: Same as Figure 6-15 for LkHα 25, HD 97048, HD 97048 N, and HD 100546

Figure 6-17: Same as Figure 6-16 for DK Cha, V921 Sco, KK Oph, and MWC 297. DK Cha N:3, 10, 100, 1000σ ($1\sigma \approx$3.9 mJy arcsec^{-2}), DK Cha 18 μm: 3, 10, 100, 400 ($1\sigma \approx$25.3 mJy arcsec^{-2}), V 921 Sco N: 3, 10, 20, 30, 40, 100, 1000σ ($1\sigma \approx$3.5 mJy arcsec^{-2}), V 921 Sco 18μm: 3, 6, 10, 25, 50, 100σ ($1\sigma \approx$12.4 mJy arcsec^{-2}), KK Oph N: 3, 5, 10, 25, 50, 100, 300σ ($1\sigma \approx$12.0 mJy arcsec^{-2}), KK Oph 18 μm: 3, 5, 10, 15, 20, 50σ ($1\sigma \approx$37.4 mJy arcsec^{-2}), MWC 297 N: 3, 10, 15, 30, 100, 1000 ($1\sigma \approx$2.8 mJy arcsec^{-2}) MWC 297 18 μm: 3, 10, 20, 100, 500σ ($1\sigma \approx$13.8 mJy arcsec^{-2}). All images smoothed by 3 pixels except HD 97048 at 18 μm, HD 97048 N, and HD 100546 at N, which were smoothed by 5, 0, and 5 pixels respectively

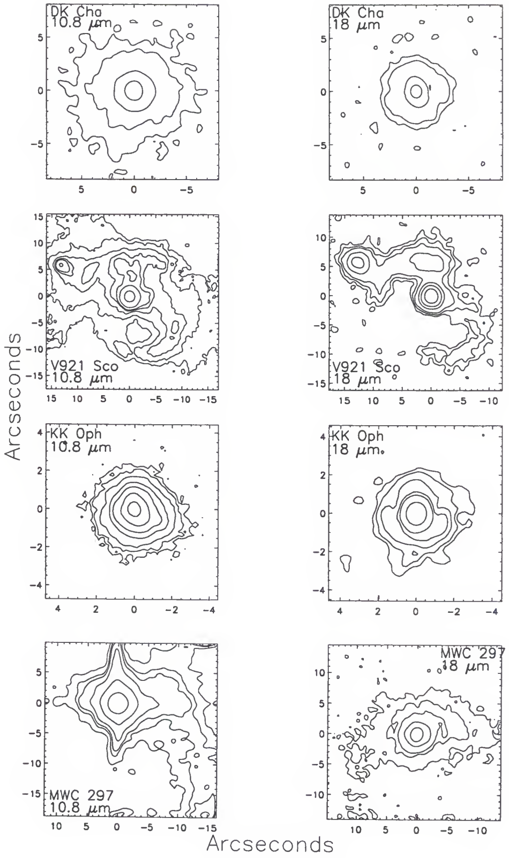

Figure 6-17: Same as Figure 6-16 for DK Cha, V921 Sco, KK Oph, and MWC 297

Figure 6-18: Same as Figure 6-17 for AFGL 2136, AS 310, BD +40 4124, and V 1318 Cyg. AFGL 2136 N: 3, 10, 30, 100, 500, 1000σ ($1\sigma \approx$5.1 mJy arcsec^{-2}), AFGL 2136 18 μm: 3, 5, 7, 10, 50, 500σ ($1\sigma \approx$73 mJy arcsec^{-2}), BD +40 4124 N: 3, 5, 10, 20, 30, 50, 100σ ($1\sigma \approx$2.2 mJy arcsec^{-2}), BD +40 4124 18 μm: 3, 10, 20, 30, 50, 100σ ($1\sigma \approx$9.8 mJy arcsec^{-2}), V 1318 Cyg N: 3, 4, 10, 100, 1000σ ($1\sigma \approx$2 mJy arcsec^{-2}), V 1318 Cyg 18μm: 3, 5, 10, 15, 50, 100σ ($1\sigma \approx$11 mJy arcsec^{-2}). All images smoothed by 3 pixels, except AFGL 2136 at 18 μm and AS 310 Sco at 18 μm which were smoothed by 5 pixels.

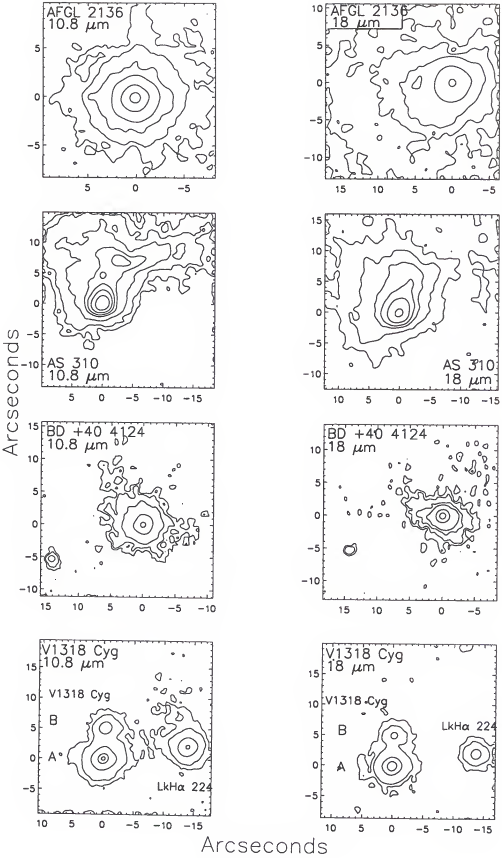

Figure 6-18: Same as Figure 6-17 for AFGL 2136, AS 310, BD +40 4124, and V 1318 Cyg

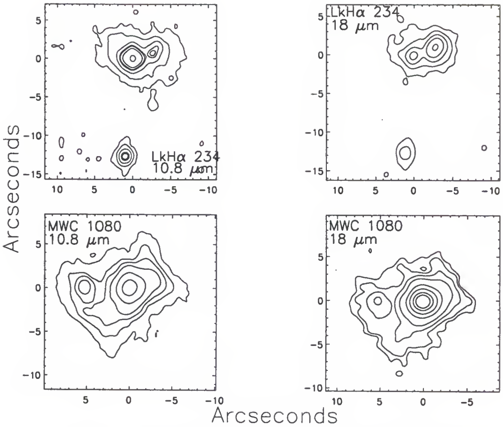

Figure 6-19: Same as Figure 6-18 for LkHα 234 and MWC 1080. LkHα 234 N: 3, 10, 25, 50, 60, 100, 500σ (1σ $\approx$2.3 mJy arcsec^{-2}), LkHα 234 18μm: 3, 10, 25, 50, 100σ (1σ $\approx$10.8 mJy arcsec^{-2}, MWC 1080 N: 3, 6, 9, 15, 60, 600σ (1σ $\approx$6 mJy arcsec^{-2}), MWC 1080 18μm: 3, 5, 10, 20, 50, 100, 500, 1000σ (1σ $\approx$4.6 mJy arcsec^{-2}) All images smoothed by 3 pixels.

with respect to main sequence stars and their binary fraction may be similar to or higher than that of T Tauri stars (Pirzkal et al. 1997; Leinert et al. 1997; Martín 1994).

Most T Tauri star studies have examined separations of up to 13″ or a few thousand AU, for these nearby systems (Ghez et al. 1993b; Leinert et al. 1993). However, since Herbig stars tend to be much more distant than T Tauri stars, a study limited to small separations will not detect close companion stars since they will not be resolved. The distribution of distances in my sample peaks at around 1000 pc, while T Tauri studies focus on objects with ~150 pc. Since my sample is almost a factor of seven times more distant, I propose to measure the companion frequency within a region seven times larger than that used in T Tauri studies; i.e. ~12,000 AU.

In the 21 fields surveyed, 11 objects show other mid-IR sources within the same field (Figures 6-14 - 6-19). I show in Table 6-7 the locations of all mid-IR companions. Of the remaining ten objects, HD 97048 has a T Tauri companion within 35″ and HD 259431, and AFGL 2136 are binary or multiple systems at optical or near-IR wavelengths. Ten of the multiple systems have mid-IR companions within 12,000 AU. HD 97048's mid-IR companion is at a distance of 6300 AU, so the number of systems with mid-IR companions within 12,000 AU is 11/21 or ~52%. BD +40 4124 and HD 259431 have optical and near-IR companions at 2480 AU and 720 AU respectively (Millan-Gabet 1999); including these two objects raises the companion frequency to 62%. This fraction is somewhat larger than that found by Leinert et al.

Table 6-7: Embedded Companions

Name	PA	r($''$)	r(AU)	Note
LkHα 198 N	4	5.8	5800	
RNO 1C	41	6.2	4960	Measured with respect to RNO 1B
RNO 1F	350	11.3	9040	Measured with respect to RNO 1B
DLIRIM 1	45	12.9	10320	Measured with respect to RNO 1B
DLIRIM 3	107	8.0	6400	Measured with respect to RNO 1B
XY Per B	75	1.2	420	
HD 97048 N	0:	35:	6300	Approximate; object in chop beam.
V921 Sco B	66	14.5	7250	
KK Oph B	248:	1.5:	240	Marginally resolved at 10 μm.
MWC 297 B	218	24.4	6100	Edge of field.
AS 310 N	1	4.1	10250	
V 1318 Cyg N	356	5.1	5100	
BD +40 4124 SE	110	15.4	15400	T Tauri (Hillenbrand et al. 1995)
LkHα 234 S	175	12.6	12600	
LkHα 234 SW	206	6.5	6500	
LkHα 234 NW	292	3.0	3000	
MWC 1080 East	89	5.2	13000	
MWC 1080 B	269	0.8	1875	Core binary, w.r.t. brighter, A component

(1997), however he only studied separations of up to 3600 AU. If I limit my sample to objects with companions within 3600 AU, I find a binary fraction of ~24% which still exceeds that expected from main sequence stars (18%) (Duquennoy & Mayor 1991). However, I am undoubtedly not detecting close companions with separations near the diffraction limit for the IRTF (0.7″). Leinert et al. (1997) may find a larger fraction since he utilized speckle imaging techniques which can resolve companions as close as 0.1″. In summary, I find a companion frequency in my sample that exceeds that expected from main sequence A and B stars and may be as much as 62%. A more complete study of the Herbig star binary fraction could be accomplished with the new 8 meter Gemini telescopes, which are equipped with adaptive optics instruments and could thus resolve companions with very small radial separations.

6.8 Mid-IR Colors and YSO Classes

Limited work has been done concerning the mid-IR colors of main sequence stars. Within the next two years, one of the major goals of the Space Infrared Telescope Facility (SIRTF) project is to better define a mid-IR color sequence for stars of all types. The first research in this field was undertaken by Johnson (1966; 1964) who established V-N colors for giant stars, and a limited range of supergiants and main sequence stars. A plot of Johnson's V-N colors for main sequence stars is shown below in Figure 6-20.

Later research utilized the IRAS all sky survey to establish V-12 μm and V-25 μm colors for the entire spectral sequence (Cohen et al. 1987; Walker & Cohen 1988) see Figure 6-21.

Many authors have studied the distribution of different classes of objects in IRAS mid-IR color-color diagrams (Walker et al. 1989; Weintraub 1990; Ivezíc & Elitzur 2000; Gregorio-Hetem et al. 1992). In particular, it is possible to separate young stellar objects (YSOs) from all other types of IRAS sources by their mid

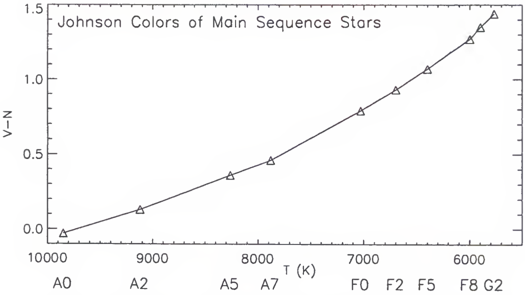

Figure 6-20: Johnson mid-IR colors for main sequence stars (Johnson 1966).

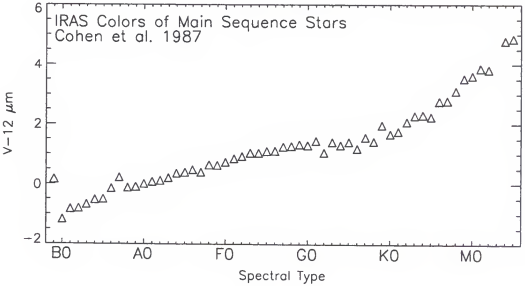

Figure 6-21: IRAS colors for main sequence stars (Cohen et al. 1987).

and far-IR colors. Several authors have defined a "T-Tauri" color space such that $0.0 \lesssim [25/12] \lesssim 0.6$ and $-0.3 \lesssim [60/25] \lesssim 0.5$ (Weintraub 1990; Harris et al. 1988; Beichman et al. 1986). This location also include members of other YSO classes such as the Herbig Ae/Be stars and the FU Orionis stars. Hillenbrand et al. (1992) finds that the three Herbig star evolutionary groups occupy different regions in a plot of V-12 μm color excess versus temperature. She finds that Group II objects have larger V-12 μm color excesses than Group I objects. Hillenbrand attributes this to larger amounts of dust and the younger evolutionary state of the Group II objects.

I examine below the mid-IR colors of 26 objects in my data set and compare them to the IRAS colors of main sequence stars. Waters et al. (1987) have shown that for G0-A0 stars the difference between the IRAS(V-N) and Johnson(V-N) colors is small, <0.05, for most stars and less than the measurement uncertainties. The transformation from Johnson N to the IRAS 12 μm system requires a correction of only 0.01 magnitudes. Since the OSCIR N filter is similar to Johnson N and the uncertainties in the OSCIR N fluxes are greater than any conversion factor, it should be reasonable to compare OSCIR N colors for my set of pre-main-sequence stars to the expected IRAS 12 μm colors of main sequence stars. As a check, I obtained the IRAS filter transmission curves, and integrated over the portion of the 12 μm filter which is coincident with the OSCIR N filter. I find a zero magnitude flux that is within 0.01 of the OSCIR N magnitude. All N band fluxes except the measurement for HD 97048 N, for which there is no 18 μm data, have been color corrected. Table 6-8 lists the color corrected fluxes for each object as well as the V-N and V-18 colors.

Table 6-8: Mid-IR Colors

Name	N	V-N	N-18	Name	N	V-N	N-18
LkHα 198 S	1.29	7.91	2.10	V921 Sco	0.11	7.87	0.52
V 376 Cas	0.59	12.11	1.79	KK Oph	1.30	7.50	1.22
RNO 1	4.51	6.09	1.84	MWC 297	-1.22	10.62	1.09
RNO 1B	3.22	6.28	1.19	AFGL 2136	-3.16	-22.84	1.13
XY Per A	2.94	4.57	0.89	AS 310	2.90	6.15	3.23
XY Per B	3.22	5.15	1.05	BD +40 4124	2.06	5.54	1.68
AB Aur	0.50	6.05	1.40	LkHα 224	1.50	9.60	1.46
HD 259431	1.81	5.29	1.13	V 1318 Cyg N	2.59	8.69	2.06
LkHα 25	2.59	5.21	1.41	V 1318 Cyg S	0.60	11.27	2.34
HD 97048	2.01	5.19	2.37	LkHα 234	2.55	6.75	1.31
HD 97048 N	3.44	5.15	...	MWC 1080	0.85	5.75	0.95
HD 100546	-0.23	6.52	2.43	MWC 1080A	1.23	5.69	1.17
DK Cha	-0.70	13.93	1.54	MWC 1080B	2.48	6.78	1.47

I plot in Figure 6-22 the color excess (V-N)-$(V\text{-}12)_0$, where $(V\text{-}12)_0$ is the color of a main sequence star, as a function of spectral type for the sample in Table 6-8. Table 6-8 shows the bandpass-corrected N fluxes, as well as the V-N colors, and N-18 colors. The method of calculating the bandpass correction was described in section 6.2. These fluxes were also corrected for extinction, using the values listed in Table 4-2 and the Rieke & Lebofsky (1985) interstellar extinction curve.

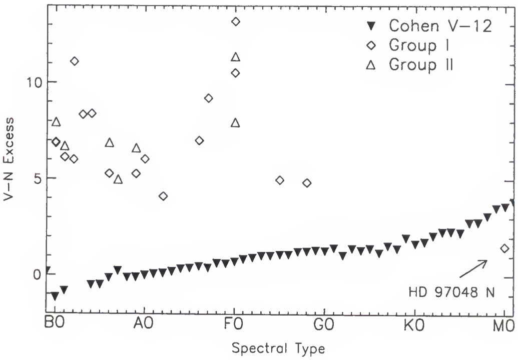

Figure 6-22: V-N color excess for 26 objects in the sample. Filled triangles show the location of the Cohen V-12 μm main sequence. Diamonds show the location of Hillenbrand Group I sources, and open triangles are Hillenbrand Group II sources.

The V-12 colors of main sequence stars are tabulated in Cohen et al. (1987) and plotted as filled triangles in Figure 6-22. For HD 97048 N, which is identified as a T Tauri star in Cambrésy et al. (1998), the exact spectral type is unknown and I assume an M0 type. Cambrésy et al. suggest a spectral type of M0 and $A_v \sim 5.8$ based upon the properties of the Chamaeleon star forming region. MWC 1080's spectral type is also uncertain, and the spectral types of the components of its binary system are unknown. Cohen & Kuhi (1979) suggested a spectral type of B0V for the system, and I assume a type of B0V for each component as well as for the unresolved system. Finally, DK Cha, V1318 Cyg S, and V 1318 Cyg N are classified as A-F; I assume a mid spectral class of F0V for each of these objects.

The T Tauri star, HD 97048 N, shows a discrepant color compared with all other objects, and falls below the Cohen V-12 main sequence. If its spectral class is G-K rather than M0, it would fall on Cohen's V-12 main sequence. Alternatively, if the extinction estimate is inaccurate, it could lie above the main sequence rather than below. The unusually cool object AFGL 2136, lies off the plot, far below the Cohen V-12 main sequence. The optical counterpart to this object may be incorrectly identified; the suggested counterpart is more than 6″ offset from the infrared position. The true counterpart may be far fainter than the 15th magnitude star cited in Lebofsky & Kleinmann (1976). In addition, as I discussed in section 6.5, AFGL 2136 may exhibit an unusual extinction law due to the presence of large grains. A fainter optical magnitude and/or a larger value of total to selective extinction would produce more realistic colors, moving AFGL 2136 into the color space occupied by the other Herbig stars.

I find that Group I and II objects occupy the same color space, unlike a similar sample shown in Hillenbrand et al. (1992). Hillenbrand et al. plotted IRAS colors rather than small aperture N photometry; the IRAS colors were very likely contaminated by emission from companions, extended envelopes, and other sources within the same large IRAS beam. This effect is illustrated clearly in the cases of MWC 1080 and V 921 Sco. MWC 1080B shows colors that are redder than for the combined system. The IRAS 12 μm flux of V 921 Sco is an overestimate by at least a factor of three due to the presence of a bright companion and extended emission. Thus, a color excess derived from IRAS fluxes will cause the source to appear redder than in a smaller aperture.

In summary, I find that the V-12 color excess does not discriminate between different evolutionary classes of Herbig stars because the large IRAS beams include emission from multiple sources. Small aperture V-N photometry shows no correlation between Hillenbrand Group and location within a plot of color versus spectral type. This type of plot does point out problems with extinction estimates and possible misidentification of optical counterparts. The extinction and V magnitudes of HD 97048 N and AFGL 2136 should be re-examined so that better estimates of their colors can be obtained.

CHAPTER 7
COLOR TEMPERATURES AND OPTICAL DEPTHS

I have calculated the 10/18 μm temperatures (T) and emission optical depths (τ) for the dust around my sample objects by applying the standard solution of the radiative transfer equation for thermal emission under the condition of uniform opacity and temperature. Mid-IR emission from the stellar photospheres is considered to be negligible since all objects are early type stars. Including foreground "screen" extinction one may write for observations at two frequencies:

$$F_{\nu_1} = \Omega(1 - e^{-\tau_{\nu_1}})B_{\nu_1}(T)e^{-\tau_{\nu 1ism}} \tag{7-1}$$

$$F_{\nu_2} = \Omega(1 - e^{-\tau_{\nu_2}})B_{\nu_2}(T)e^{-\tau_{\nu 2ism}} \tag{7-2}$$

Where F_ν is the observed flux density at frequency ν, Ω the solid angle, τ_ν the emission optical depth of the circumstellar material, $B_\nu(T)$ the Planck function at frequency ν and temperature T, and $\tau_{\nu ism}$ the optical depth due to the intervening interstellar medium. I correct for interstellar extinction using tabulations from Rieke & Lebofsky (1985) and Mathis (1990), and a ratio of total to selective extinction $R=\frac{A_V}{E(B-V)}=3.1$. I assume an extinction A_V, for each object, as listed in Table 4-2.

I adopt a circumstellar grain emission efficiency, $Q(\lambda) \propto \lambda^{-1}$. The emission optical depth, $\tau(\lambda)$, then becomes proportional to λ^{-1}, because $\tau(\lambda) = \pi a^2 Q(\lambda) N L$, where a is the grain radius, N is the number density, and L is the path length. I note that the environments of Herbig stars are most likely regions of grain growth, with grain sizes larger than those in the interstellar medium and that an circumstellar extinction law of this nature may be more appropriate for larger grains than a law based upon the measurements of the interstellar medium (Lynch & Mazuk 2000).

An IDL code was developed to simultaneously solve for temperature and optical depth given the above criteria. The code uses an initial estimate of the temperature and optical depth and then uses the relationship shown above between flux and temperature to iterate a solution. A Newton-Rapheson iteration was utilized. Since the observed flux depends both on the source size and the emission optical depth, τ cannot be determined for unresolved sources. For these objects the observed PSF provides only an upper limit to the source size. However, a lower limit to the source size can be obtained by assuming the source is an optically thick blackbody; $F_\nu=\Omega B_\nu(T)$, and simultaneously solving for Ω and T.

For resolved sources, with extended emission, temperature and optical depth maps were created. In these cases, the two input images were cross-convolved with appropriate PSF stars to achieve the same spatial resolution. The 1σ level was determined for each convolved image and temperatures and optical depths were then calculated from the flux ratios for each pixel which was at least 3σ above the noise. The IDL code for these calculations may be found in the Appendix.

I show in Table 7-1 color temperatures for the unresolved sources, and the minimum source size in AU for the blackbody limit. A detailed discussion of the temperature and optical depth maps of the four resolved sources, HD 259431, AS 310, LkHα 234, and MWC 1080 is reserved for Chapter 8.

7.1 Color Temperatures of Unresolved Sources

I have calculated 10/18 μm color temperatures of all unresolved sources, including binary components, for which 10 and 18 μm fluxes were obtained. I include in these calculations KK Oph, although its binary companion was resolved, and BD +40 4124, although it exhibits marginally resolved extended emission. The contributions to the fluxes from the companion and extended emission of these two objects are negligible and have no effect on the temperature determination. I list in Table 7-1 the color temperatures as well as the blackbody limiting sizes.

Table 7-1: N/18 μm Temperatures of Unresolved Sources

Name	T (K)	a(AU)	Name	T(K)	a(AU)
LkHα 198 N	168	25	HD 97048	179	11
LkHα 198 S	187	40	DK Cha	226	14
V 376 Cas	212	38	KK Oph	265	4
RNO 1	206	9	BD +40 4124	220	28
RNO 1B	248	8	BD +40 SE	237	3
XY Per A	314	2	LkHα 224	239	28
XY Per B	289	3	V 1318 Cyg N	187	35
AB Aur	252	6	V 1318 Cyg S	172	122
LkHα 25	238	13			

With one exception, V 1318 Cyg S, all the sources in Table 7-1 have smaller blackbody sizes than expected from a circumstellar disk (a few hundred AU). In these cases, the dust must be optically thin, yet the thermal emission is not resolved, either due to the faintness of the emission, or the distances of the sources. No correlation is found between evolutionary class and temperature; these objects include both Group I and Group II sources. However, the four coolest objects in the sample, LkHα 198 N/S, and V 1318 Cyg N/S are both binary systems associated with molecular outflows.

The minimum extent of the dust of V 1318 Cyg S, derived from the blackbody approximation to the 10 and 18 μm fluxes, is 122 AU, equivalent to the size observed for some circumstellar disks, such as HR 4796, which has a diameter of 200 AU at 18 μm (Jayawardhana et al. 1998). The large blackbody size of V 1318 Cyg S may be due to the presence of additional cool dust, which V 1318 Cyg N is lacking. An analysis of the 3 to 18 μm SEDs of V 1318 Cyg N and S shows that at wavelengths longer than 10 μm the SED of V 1318 Cyg S continues to rise, implying emission from cooler dust at longer wavelengths, while the SED of V 1318 Cyg Nbecomes flat. Possibly V 1318 Cyg S is the younger of the two objects and remains somewhat more embedded. This system is known to be an irregular large amplitude (ΔV=8.55) variable in the optical (Herbst & Shevchenko 1999), but it is not known which of the pair of objects dominates the variability. Since variability is associated with youth, it would be very interesting to know if V 1318 Cyg south is the origin of the variability.

7.2 Narrow Band Colors

Multifilter imaging was obtained for the sources XY Per, DK Cha, and V 1318 Cyg, and narrow-band colors were calculated throughout the mid-IR regime. Here I discuss the results of these calculations and their relationship to spectral features.

The binary system, XY Per A/B shows color temperatures that reflect the shape of its mid-IR SED. The brighter object in the mid-IR, XY Per A, dominates the temperature distribution at all wavelengths except, 4.8 μm and 7.9 μm. I find 7.9/18 μm color temperatures of 322 K and 332 K for the A and B components respectively. The components are of nearly equal flux at 7.9 μm, but XY Per A is slightly brighter at 18 μm. The M/9.8 μm temperatures reflect the fact that the B component is the brighter object; I find temperatures of 459 K and 533 K for the A and B components respectively. XY Per A appears to show a silicate feature peaking at 10.3 μm in its mid-IR SED. I find 10.3/18 μm color temperatures of 316 K and 284 K for the A and B components; the higher temperature of A is likely due to the silicate emission feature.

DK Cha shows a temperature of 214 K from the 9.8 and 18 μm fluxes, and a slightly higher temperature of 241 K from the 8.8 and 18 μm fluxes. This is in agreement with the observation of a silicate absorption feature in this objects SED (Figure 6-8).

Multifilter temperature calculations show no unusual features for either V 1318 Cyg N or V 1318 Cyg S. Both objects show a silicate feature in their mid-IR SEDs (Figure 6-12) and exhibit temperature minima at wavelengths coinciding with the silicate feature. I find that they show nearly identical temperatures for any two chosen flux ratios. The lowest calculated temperature is 160 K, for the 9.8/12.5 μm flux ratio. The highest temperature is 290 K, for the 7.9/12.5 μm flux ratio. The maximum blackbody size occurs for the 10.3/18 μm ratio. Here I find a temperature of 172 K, and blackbody sizes of 45 AU and 135 AU for V 1318 Cyg N and V 1318 Cyg S respectively.

7.3 Temperature and Optical Depth of Resolved Sources

Temperatures and optical depths were determined using the technique discussed in Chapter 7. η Sgr was used for PSF convolution for the V 921 Sco maps and α Lyr, and α Her were used similarly for the MWC 297 maps. All calculations included a correction for extinction by the interstellar medium, (A_v), which is tabulated in Table 4-2.

7.3.1 RNO 1C

RNO 1C is resolved at 18 μm and a source size can be estimated by quadrature subtraction of the PSF. I measure an 18 μm FWHM for an unresolved point source of $\sim 1.32''$ and an 18 μm FWHM for RNO 1C of $1.61''$. Quadrature subtraction yields an 18 μm source size of $0.91''$. The 10 to 18 μm flux ratio, in conjunction with the source size, yields an intrinsic source temperature of 177 K, and emission optical depth at 10.8 μm of 0.002. At the distance of RNO 1C, $0.91''$ is equivalent to 728 AU. This object is especially interesting because it is classified as an FU Orionis type Herbig star. These objects are believed to possess active accretion disks; if this emission arises in a circumstellar disk, it would be one of the largest disks measured in the infrared.

7.3.2 HD 100546

Using the optically thin approximation for the 10 and 18 μm fluxes of HD 100546, I find a 10/18 μm color temperature of 186 K. Since HD 100546 is not resolved at 10 and 18 μm, the source size is unknown, and τ cannot be determined at these wavelengths. The blackbody approximation yields a lower limit to the source size of 17 AU. However, if we assume the 11.7 μm emission is resolved, the source size can be estimated by quadrature subtraction of the PSF; $(\mathrm{FWHM}^2_{source}\text{-}\mathrm{FWHM}^2_{PSF})^{1/2}$. Using this method, I obtain an intrinsic source size of 0.6″, or ~60 AU. Assuming optically thin emission and the above source size, I find an emission optical depth at 9.7 μm of 0.38. Recent adaptive optics imaging by Pantin et al. (2000) and 0.65 μm imaging with the HST (Grady et al. 2001) have resolved a circumstellar disk around this relatively nearby (103 pc) object. Pantin et al. find a disk diameter of 200 AU at 2.2 μm, with the dust density peaking ~40 AU from the star. The location of the peak density compares well to the radius of the mid-IR source (30 AU) which might be expected since the mid-IR flux is dominated by thermal emission from dust grains.

7.3.3 V921 Sco

The temperature maps of V 921 Sco show very similar structure regardless of wavelength. A bright, hot source dominates the temperature distribution. A cool diffuse source lies almost directly north, and an arc of diffuse emission terminating in a second warm source stretches from the north to the east. I show below the 7.9/18 μm, 9.8/18 μm, and 12.5/18 μm color temperature and emission optical depth maps which reveal new information about this region. V 921 Sco shows a much hotter core temperature at all wavelengths than any other source in this survey. Peak temperature of the core source in the 7.9/18 μm map (Figure 7-1) is 475 K. This map shows evidence for the presence of transiently heated grains. The temperature of the diffuse source increases radially from the 300 K centroid. The primary source also shows an external shell of hot grains. I speculate that this region may be enveloped in a soup of transiently heated grains that shifts the temperature distribution to hotter values. The optical depth map shows similar structure, with a peak $\tau_{7.9\mu m}$ ≈0.0002 associated with the primary source.

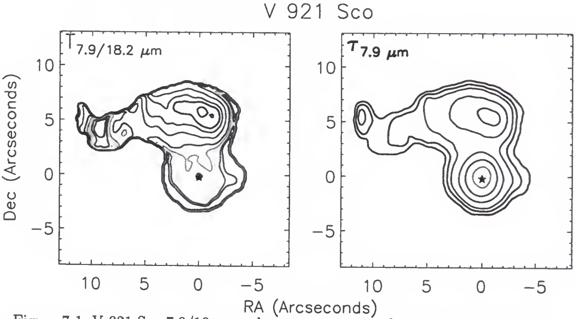

Figure 7-1: V 921 Sco 7.9/18 μm color-temperature and optical depth maps. Position of the central star is marked (*star*). Temperature contours are 305, 320, 335, 365, 410, 440, 455, 470, 485 K. Optical depth contours are 1×10^6, 5×10^6, 1×10^5, 2.5×10^5, 5×10^5, 1×10^4, 1.5×10^4, 5×10^4, 1×10^3.

The 9.8/18 μm map (Figure 7-2) shows a more normal temperature distribution. The primary source peaks at 540 K and the temperature decreases radially. A lobe of warm dust also stretches west of the primary towards a 400 K hotspot. The diffuse source exhibits a double-lobed temperature structure which has a peak temperature of 160 K. The entire source appears to be partially enveloped in the warm dust surrounding the primary. The 9.8 μm optical depth map shows that the peak optical depth (0.0004) is now associated with the double-lobed diffuse source. The warm western lobe of emission seen in the temperature map shows a local optical depth minima of 0.00001.

Finally, I show the 12.5/18 μm temperature and optical depth maps in Figure 7-3. The peak temperature of this map is offset from the location of the star by several pixels and a cool central structure (390 K) is surrounded by warmer (430

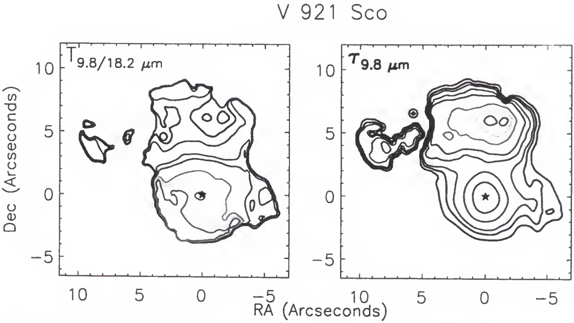

Figure 7-2: V 921 Sco 9.8/18 μm color-temperature and optical depth maps. Position of the central star is marked (*star*). Temperature contours are 170, 185, 210, 300, 350, 470, 500, 530 K. Optical depth contours are 1×10^6, 5×10^6, 1×10^5, 2.5×10^5, 5×10^5, 1.5×10^4, 2.5×10^4, 3.5×10^4.

K) emission near the core of the primary source. The northern diffuse source again shows an elongated 150 K core, and an arm of 200 K emission stretches towards the east. The optical depth centroid does coincide with the position of the primary, but the peak optical depth (0.0007) has shifted to the diffuse source.

In summary, I find that the temperature associated with the primary source peaks in the 9.8/18 μm color temperature map, and is lowest in the 12.5/18 μm map. This object exhibits the warmest mid-IR color temperatures of any in the sample. The temperature trend suggests the presence of a continuum of warm transiently heated grains to maintain such high temperatures throughout the mid-IR regime. ISO spectroscopy, does not resolve the north diffuse source or the primary, but does show very strong 7.7 and 11.3 μm emission features (Kerckhoven et al. 2000). The northern diffuse source is probably associated with a heavily embedded pre-main-sequence star. This object shows the highest optical depth and coolest temperatures in the 9.8 and 12.5 μm optical depth maps. This source is very diffuse and faint at 10

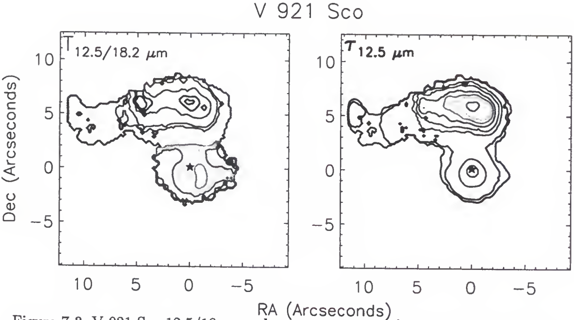

Figure 7-3: V 921 Sco 12.5/18 μm color-temperature and optical depth maps. Position of the central star is marked (*star*). Temperature contours are 145, 150, 160, 190, 205, 405, 425, 450, 550 K. Optical depth contours are 5×10^6, 1×10^5, 5×10^5, 1×10^4, 2×10^4, 3×10^4,4×10^4, 6×10^4.

μm but becomes bright and point-like at 18 μm, suggesting the presence of a silicate absorption feature. The sharp increase in temperature of this object at 7.9 μm, also suggests the presence of a 7.7 μm PAH feature.

7.3.4 MWC 297

This unusual object exhibits two warm lobes (340 K, 460 K) of emission at a position angle of 50 degrees surrounding a cooler (270 K) central source. Assuming a distance of 250 pc for MWC 297 (from Hipparcos astrometry) these lobes are at radii of 560 and 910 AU. An arm of warm, 250 K emission extends 13″ towards the west and southwest towards the companion star, which is off the field of view. In the surface brightness maps, the arc of 10 μm emission can be seen to extend to the companion star on the edge of the frame. This arm of emission is intriguingly similar to the structure observed around MWC 1080. In MWC 1080's case it is likely that the interactions between multiple companion stars, and the primary, disrupted the dust envelope and produced tidal arms of thermal emission. MWC 297 appears to possess only one distant companion at the end of the arm of emission. However MWC 297 exhibits x-ray flares which are not normally associated with early type stars (Hamaguchi et al. 2000). The previous authors note that the flare spectral signature strongly resembles that of the late type pre-main-sequence stars, the T Tauri stars. MWC 297 may possess a close T Tauri companion which is yet unresolved; such an object might explain the arc of emission, and the x-ray activity.

MWC 297's optical depth map shows a boxy shaped morphology, with contours of higher optical depth perpendicular to the warm temperature lobes. The peak optical depth is 0.003 and more tenuous fingers stretch along the warm western arm. The locations of the optical depth contours and warm temperature lobes suggest lobular structure, such as a warm outflow bisected by a higher optical depth structure, however no similar structure is seen in the surface brightness maps (Figure 6-17).

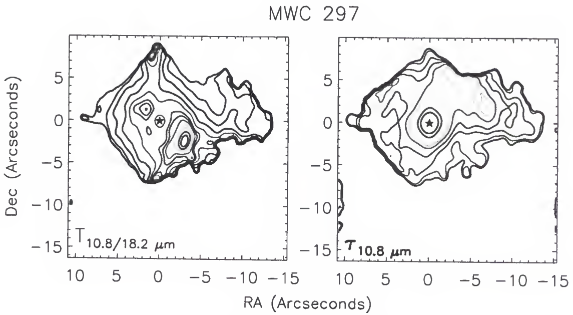

Figure 7-4: MWC 297 10.8/18 μm color-temperature (*left*) and optical depth (*right*) maps of MWC 297. Position of the central star is marked (*star*). Temperature contours are at intervals of 30 K from 160 to 310 K, and then at levels of 325, 340, 370, 400, and 430 K. Optical depth contours are 5×10^6, 1×10^5, 2.5×10^5, 5×10^5, 1×10^4, 1.5×10^4, 5×10^4, 1×10^3.

7.3.5 AFGL 2136

Because AFGL 2136 is not resolved at 10 μm, a color temperature map cannot be constructed. However, the object shows large scale extended emission at 18 μm. As discussed previously, this could be evidence of large grains which emit more efficiently at 18 μm than at 10 μm. I find a color temperature of 154 K from the ratio of the 10 and 18 μm fluxes assuming an optically thin approximation. The blackbody limiting size corresponds to a diameter of 1000 AU. However, it is obvious that most of the 18 μm flux does not originate in a disk of this size, but extends at least 33″, or 66,000 AU in my image. Taking the ratio of the fluxes within a 5.5″ aperture, I find a color temperature of 197 K in the optically thin limit, and a blackbody size of 400 AU. Assuming a source size of 5.5″, I find an optical depth at 9.7 μm of 0.005. Deep narrow-band imaging is needed of this source to better trace the temperature distribution and estimate a true source size.

Temperature and optical depth calculations for the sample objects help restrict the source sizes of unresolved objects, and indicate different evolutionary states for binary systems. Maps of the temperature variations within the dust around these objects suggest the presence of transiently heated grains, as well as larger silicate grains and reveal structure that is not seen in the surface brightness maps. Additional narrow-band observations are needed of AFGL 2136, RNO 1C and MWC 297, to study the variation of temperature with wavelength and search for spectral features associated with PAH or silicate grains.

CHAPTER 8
CORE SOURCES

Here I discuss in detail the results for the four sources for which I have the most extensive data; HD 259431, AS 310, LkHα 234, and MWC 1080. Observations were made spanning the 4-18 μm range for all objects, and multiple observations over a period of four years were conducted for MWC 1080 at both the IRTF and Keck telescopes. The astrophysical parameters for all four objects are listed in Table 4-2. All stars are Hillenbrand Group I, whose SEDs are well modeled by emission from a optically thick, geometrically-thin circumstellar disk. The aspects of each source were summarized in Chapter 4.

8.1 Mid-IR Morphology

I have detected extended emission from warm dust grains around each of the four objects. Contour maps of the surface brightness at 10 and 18 μm are presented in Figure 6-15, 6-18, and 6-19. I discuss the mid-IR morphology of each source below.

8.1.1 HD 259431

The 10 μm contour map of HD 259431 (Figure 6-15) shows extended emission which is concentrated along PA$\approx$60 degrees as well as fainter fingers of emission extending southeast. Extended emission is seen in all filters (4-18 μm) but is brightest at 10 μm. The 10 μm emission extends to a radius of $\sim$6$''$ from the bright central source. Assuming a distance of 800 pc to HD 259431, this emission extends 4800 AU. An estimate of dust temperature as a function of distance from a star, may be derived assuming thermal equilibrium, and some knowledge of absorption efficiency,

Q_{ab}. The Planck-averaged efficiency is:

$$\langle Q(T,a)\rangle = \frac{\int B_\nu(T) Q_{\nu,a} d\nu}{\int B_\nu(T) d\nu} \propto T^n \tag{8-1}$$

Where B_ν (T) is the Planck function at frequency ν and temperature T. The monochromatic efficiency in the infrared, $Q_{\nu,a} \propto \nu^n$, where we assume n is approximately 1 (Lynch & Mazuk 2000) (other values may be more appropriate at longer wavelengths). Equating energy absorbed with energy emitted, using $\langle Q_{ab}\rangle \propto T_*$ and $\langle Q_{em}\rangle \propto T_d$ we solve for distance as a function of dust temperature:

$$\frac{L_* \pi a^2}{4\pi r^2}\langle Q_{ab}\rangle = \sigma T_d^4 \langle Q_{em}\rangle 4\pi a^2 \tag{8-2}$$

$$r = \left[\frac{L_*}{16\pi\sigma T_d^4}\frac{T_*}{T_d}\right]^{1/2} \tag{8-3}$$

where L_* is stellar luminosity, T_* is stellar temperature, T_d is dust temperature, a is dust grain radius, and r is distance from star. Assuming values for a B1 V star $L_* \approx 16000\, L_\odot$, $T_* \approx 24200$ (Gray 1992), and a mid-IR dust temperature of 300 K, we find that dust can be heated to ~980 AU compared to the observed radial extent of 2400 AU. Since the radial distance of the observed flux exceeds that expected from grains in thermal equilibrium, we suggest that the dust around HD 259431 may include a significant fraction of small, transiently heated grains. As mentioned previously, IRAS data showing the strong 11.3 μm PAH feature supports this conclusion (Figure 3-4).

8.1.2 AS 310

AS 310 exhibits large-scale extended emission at all mid-IR wavelengths. At 10 μm this emission extends north and west from the central star (Figure 6-18). I detect a companion 4.7″ north of AS 310 (see Table 8-3) at a position angle of ~1 degree. I estimate uncertainties on the position angle measurements of approximately a degree. I identify this object with the near-IR source AS 310-C located at PA≈2.9, separation ≈4.9″ (Ageorges et al. 1997). An additional elongated source of diffuse emission is located ~8″ to the northwest of the companion which may be associated with an extended radio source detected by Cohen et al. (1982). However this source is not correlated with any emission at near-IR or optical wavelengths. The 0.7 μm map (Figure 8-1) shows objects which coincide with both mid-IR and near-IR sources. The brightest R band source is coincident with the AS 310 mid-IR primary. Source B of Ageorges et al. (1997), which is located at position angle ~121 degrees rather than the 153.9 cited in the above paper, coincides with a source in the R band map, but is not detected at 10 μm. The extended nebulosity to the north of the primary star in the R band map is approximately coincident with the northern 10 μm companion and source C of Ageorges et al.. Deeper R band imaging might reveal the northern source and provide a better comparison to the 10 μm image. These maps, in conjunction with the larger scale near-IR imaging of Testi et al. (1998) indicate that AS 310 is a member of a rich cluster.

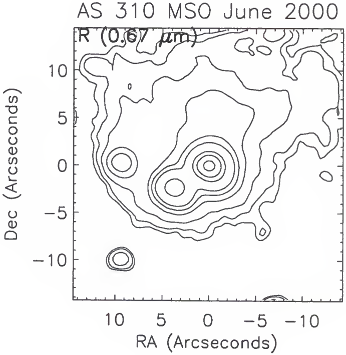

Figure 8-1: R band image of AS 310 from the MSO 74 inch.

8.1.3 LkHα 234

LkHα 234 was previously observed in the mid-IR by Cabrit et al. (1994) who detected a bright companion to the northwest of the primary (LkHα 234-NW) and a fainter source 12″ to the south (LkHα 234-S). We also detect these three sources (Figure 8-2), as well as a fourth source (LkHα 234-SW) associated with a water maser (Tofani et al. 1995).

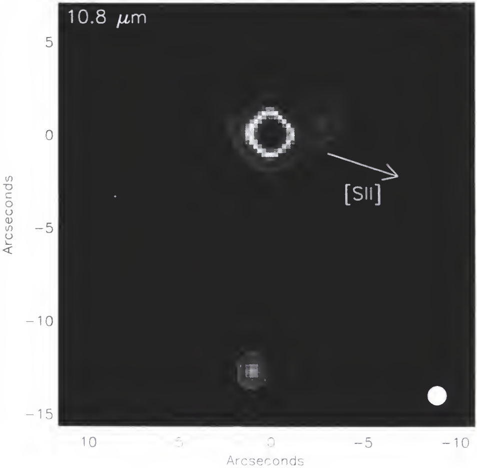

Figure 8-2: N band image of LkHα 234. CO outflows are marked (Mitchell & Mathews 1994), as well as the positions of 2 jets seen in H_2 and [SII] (Ray et al. 1990). X marks the location of water masers (Tofani et al. 1995; Cabrit et al. 1997), and + is the location of a radio continuum source (Skinner, Brown & Stewart 1993). The small white circle in the lower right indicates the FWHM of the PSF as measured from a nearby star.

The northwest companion coincides with a radio continuum source (Skinner, Brown & Stewart 1993), as well as a CO outflow oriented at position angle of 45 degrees (Mitchell & Matthews 1994). In addition two H_2O masers are located within 1″ of this source (Tofani et al. 1995). Figure 8-2 shows the placement of the maser sources, CO outflow, radio continuum source, and H_2 and [SII] jets. The mid-infrared observations show additional extended emission associated with this source. In particular I detect structures suggestive of a circumstellar disk. The M band map shows a central bright source with lobe-like extensions on both sides. At 7.9 μm the central source disappears and only two lobes can be seen (Figure 8-3). The 9.8 and 10.3 μm maps show emission at the location of the central M band source and the right lobe only. At longer wavelengths (11.7, 12.5, and 18 μm) the lobe structure disappears and only a bright elongated source is present. The position of the peak flux at 11.7, 12.5, and 18 μm is located near the location of the right "lobe" detected at M, 7.9, 9.8, and 10.3 μm. At 18 μm the flux density of this source exceeds that of the primary star. The N-band map of this structure appears to be dominated by the longer wavelength 11-12 μm flux and exhibits a single bright elongated source. I list position angles and separations for the centroid of this structure, as well as total fluxes in Table 8-3

Several clues suggest that the mid-IR emission may originate in a heavily embedded early-type star with a circumstellar disk. As I discuss in section 8.1, I find a broad silicate absorption feature at this position. The radio continuum source associated with this object may be produced by an ultra-compact HII region surrounding the young luminous star. The CO outflow, which is oriented perpendicular to the mid-IR "lobes" could be part of a bipolar outflow from the embedded star. Finally, the two nearby water masers indicate the presence of shock fronts which can be formed either in outflows or within a circumstellar disk (Slysh et al. 1999).

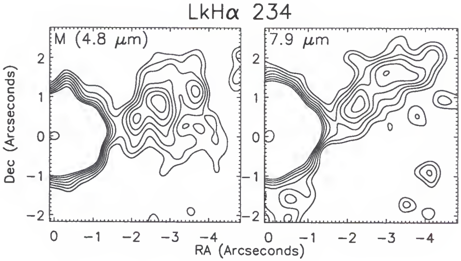

Figure 8-3: LkHα 234 companion. (*Left*) 4.8 μm surface brightness map of disk-like structure around LkHα 234-NW. (*Right*) Same as above, for 7.9 μm.

Higher resolution near-IR and mid-IR imaging of this object could provide the first confirmed detection of a disk around a young Herbig star.

8.1.4 MWC 1080

Mid-IR maps of MWC 1080 from the IRTF and Keck resolve the close binary detected by Leinert, Richichi, & Haas (1997) and reveal the presence of a companion 5.2″ east of the star and extended structure similar to two tidal tails (Figure 6-18, Figure 8-4). The companion at 5.2″ east coincides with a K band source detected by Pirzkal, Spillar & Dyck (1997) and Hillenbrand (1992). Assuming a distance of 2500 pc, the close companion and eastern companion orbit at 1750 AU and 13,000 AU respectively. The short period eclipsing component present within the core binary probably has a distance of less than 1 AU. Estimates of the luminosity of the B component of the core binary from near-IR speckle interferometry observations suggest that it is also a pre-main-sequence Ae/Be star (Leinert, Richichi, & Haas 1997). As I shall show in a future paper, MWC 1080 has several other infrared companions, including two sources visible in the J, H, and K bandpasses at position angles of 77 and 89 degrees and radial distances from the primary of 14.3″ and 10.2″ respectively.

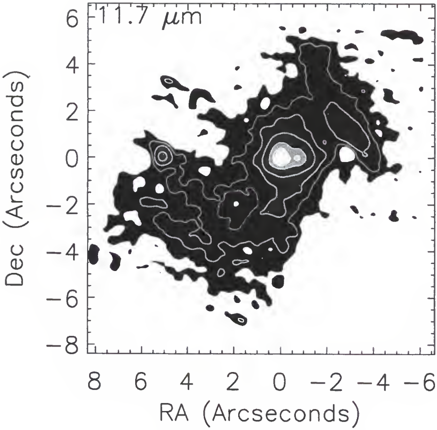

Figure 8-4: Keck 11.7 μm surface brightness of MWC 1080 showing "tidal" arms and resolved binary as well as eastern companion.

Binary, or multiple systems are predicted to form through the fragmentation of a massive circumbinary disk (Bonnell 1998). The interaction between a disk and an inner binary can fragment the disk and induce large scale (1000 AU) spiral structure (Burkert & Bodenheimer 1996). Interactions between the spiral arms may then form a Jeans mass condensation which can collapse to an additional companion which may then evolve to a wider separation through angular momentum transfer. The MWC 1080 system exhibits similar structure, with an inner binary, and an outer companion located at the terminus of one of the tidal arms. However, fragmentation processes are expected to occur early in protostellar evolution and it is uncertain whether structure would endure until the stars become optically visible.

8.2 Photometry

I have conducted multi-aperture photometry on each mid-IR image to measure how much of the mid-IR flux originates from the region around the central star, and from other sources within the field. I measured fluxes for the entire field as well as fluxes within 4″ (18x18 pixel) and 5.8″ (26x26 pixels) square apertures centered on the flux peak. I chose apertures that would enclose at least 90% of the encircled energy at the respective wavelengths taking into account the predicted PSF for the obscured aperture of each telescope configuration. These apertures completely encircle the IRTF diffraction limited airy disk at 10.8 and 18.2 μm respectively. For the higher resolution Keck observations, I measured fluxes within 1x1″ apertures and 2x2″ apertures which were appropriate for the diffraction limits at Keck. At the distances of HD 259431, AS 310, LkHα 234, and MWC 1080, 1″ represents 800, 2500, 1000, and 2500 AU respectively; thus these apertures sample the flux within the region that a circumstellar disk might exist.

I find that for these four objects extended dusty envelopes and embedded companions can account for on average 50% of the mid-IR emission in the regions surrounding these stars. Hillenbrand et al. (1992) estimate lower limits to disk radii of 61, 125, and 142 AU for HD 259431, LkHα 234, and MWC 1080 respectively based upon 20 μm flux measurements. However, I find that the 18 μm flux is not a good indicator of disk radius as much of the emission originates in sources unrelated to circumstellar disks. As I will show in section 8.3, the revised SEDs have spectral indices that are not characteristic of Group I circumstellar disk systems. My photometry results are presented in Tables 8-1, 8-3 and 8-2.

Table 8-1: Multi-aperture Fluxes (Jy)

	HD 259431^{d}		AS 310		LkHα 234		MWC 1080	
Filter	Total	4x4″	Total	4x4″	Total	4x4″	Total	4x4″
K	...	...	...	...	...	...	5.83^{a}	5.43
M	5.73	5.27	...	...	3.24	1.95	14.20^{a}	11.88
N	8.50	6.08	11.82	2.83	5.18	3.09	17.10^{b}	13.20
7.9	6.87	5.04	16.60	1.09	5.42	2.37	15.38	12.28
8.8	8.50	6.60	9.96	1.95	3.50	2.34	17.11	12.95
9.8	7.68	6.78	10.55	3.67	4.50	2.83	13.95	11.86
10.3	8.20	6.49	5.43	3.24	4.09	2.81	16.42	13.23
11.7	9.88	6.09	13.09	2.88	3.88	2.72	21.23	14.24
12.5	10.47	5.49	11.97	2.17	3.69	2.26	22.34	13.00
		5.8x5.8″		5.8x5.8″		5.8x5.8″		5.8x5.8″
18.2	10.31	6.18	47.97	15.05	11.46	3.59	14.76^{b}	11.77
						6x6″		6x6″
20.8^{c}	...	...	...	...	32.30	8.87	14.29	10.68

^{a}M and K observations for MWC 1080 from 1996

^{b}Additional observations
1996: N_{tot}=17.70 Jy, $N_{4x4''}$=13.25 Jy; 18.2_{tot}=13.95Jy, $18.2_{5.8x5.8''}$=11.31 Jy
1995 12 09:N_{tot}=16.16 Jy, $N_{4x4''}$=12.87 Jy
1995 12 10: N_{tot}=15.45 Jy, $N_{4x4''}$=11.56 Jy; 20.8_{tot}=13.88 Jy, $20.8_{6x6''}$=11.08 Jy, and K_{tot}=6.67 Jy, $K_{4x4''}$=5.52 Jy

^{c}20.8 μm observations from 1995 12 09

^{d}N, 18.2 μm observed 09 1997, others 11 1999. Additional observations
1999 11 10: 18.2_{tot}=10.4 Jy, $18.2_{5.8x5.8''}$=6.18 Jy
1999 11 12: N_{tot}=7.80 Jy, $N_{4x4''}$=6.44 Jy

8.3 Variability

The observations of MWC 1080 span a four year period and can be examined for mid-IR variability. A comparison of IRTF photometry of the unresolved MWC 1080 core source with Keck data, which resolves the two stellar components shows that they agree well for the N band filter. I tentatively suggest some variation in narrow-band 11.7 μm fluxes. If one compares the flux ratios of the two core component stars within the N filter for the May 3 observation, one finds that the ratio changes by less than 2% when compared to the same ratio for the May 5 observation. This appears to imply a relatively constant flux within the N bandpass. However, flux ratios computed from the 11.7 μm observations vary by as much as 15% between the May 3, 4, and 5 observations. If this variation was due to clouds, one would expect that the ratio would remain constant from night to night, assuming that the two stars were equally affected by clouds. I suggest that the 11.7 μm bandpass might contain variable emission from the 11.3 μm PAH feature. Wooden (2000) has noted that line variability is seen in this feature in High efficiency Infrared Faint Object Grating Spectrometer (HIFOGS) spectra. MWC 1080 is known to vary on a 2.9 day period in the optical due to the close eclipsing companion (Shevchenko et al. 1994; Grankin et al. 1992). If the 11.3 PAH emission originates close to the star, perhaps the eclipsing companion might be responsible for the observed variability. Time resolved spectroscopy of this feature might help resolve this issue.

Table 8-2: MWC 1080 Positions and Fluxes (mJy) Keck 1999

		MWC 1080 A	MWC 1080 B			MWC 1080 East		
Date	Filter	1x1″	PA	Sep	1x1″	PA	Sep	1x1″
05/03	N	11121	269	0.75	3620			
	11.7	5501	269	0.74	1953			
		2x2″			2x2″			
	18.2	7208	269	0.72	4480	...	...	...
05/04	11.7	7637	270	0.77	2944	89	5.1	400
05/05	N	9455	267	0.75	3030	87	5.1	548
	11.7	8652	268	0.76	2814	89	5.1	559
	12.5	8973	267	0.76	2648	87	5.1	697
		2x2″			2x2″			
	18.2	10178	270	0.75	4236			

Turning to the eastern companion, MWC 1080 E, I find variation in its flux density among the IRTF observations. While the broad-band N fluxes agree well for the primary star among the four IRTF data sets, the eastern companion is seen to decrease in flux by 20% between the 1996 and 1997 observations. Some support for the variability of this object is seen in near-IR observations. Pirzkal, Spillar, & Dyck (1997) list a K band companion of MWC 1080 at PA=87 degrees, separation=4.69″ that coincides within 0.4″ of the position of MWC 1080 east. Our own K band maps (unpublished) show only one star, MWC 1080 east, within 10 degrees of this position, thus we suggest that Pirzkal et al.'s object may be identified as MWC 1080 east. They cite a ΔK magnitude of 6.2, while Hillenbrand (1992 thesis) cites a ΔK magnitude of 3.1 for MWC 1080 east; this leads to a variation of 3.1 magnitudes at K. The FU Orionis class of pre-main-sequence stars are known to vary with similar large amplitudes. Additional high resolution near-IR and mid-IR observations are needed of MWC 1080 to confirm the suggested variability in this system.

8.4 Spectral Energy Distributions

I have compiled extensive infrared to radio fluxes for HD 259431, AS 310, LkHα 234 and MWC 1080 from the literature. Fluxes were chosen from the literature based upon two criteria: beam sizes and zero magnitude fluxes for the filter system must be cited in the literature, and, if duplicate observations exist, observations with the smallest beam sizes were selected. Using the literature fluxes (Table 8-4) and my own small aperture photometry (Tables 8-1, 8-3, 8-2), I have constructed revised SEDs for the four Ae/Be stars and their companions (Figures 8-5–8-8). These SEDs do not account for the known variability of the sources; some Ae/Be stars are known to be variable by nearly a magnitude at IR wavelengths (Davies et al. 1990; Cohen & Schwartz 1976), and beam sizes vary across the wavelength range. I have dereddened the observed SEDs using the extinctions listed in Table 4-2 and calculated revised 3-10 μm indices from published 3 μm data and the mid-IR OSCIR fluxes (Table 6). The new spectral indices are not in accordance with those expected from a standard optically thick, geometrically-thin disk model. These SEDs may be more characteristic of flared disk models, or envelope+disk models. Flared disks will intercept a larger percentage of the stellar radiation than flat disks and the IR spectrum will fall off less steeply than that of a flat disk. Flared disks will exhibit SEDs of slopes $\lambda F_\lambda \propto \lambda^{-2/3}$ (Kenyon & Hartmann 1987). Viewing angle may also influence the observed SEDs, but at this time we are not able to estimate such factors.

In Figures 8-5 and 8-6 I show SEDs for HD 259431 and AS 310. The mid-IR region of both objects shows a silicate emission feature. Previous researchers cited an absorption feature or a flat spectrum for HD 259431 (Berrilli et al. 1992; Sitko 1981); this appears to be simply an effect of aperture size. Large apertures induce the appearance of a flat spectrum since they collect emission from the dusty envelope as well as from the circumstellar regions of this star. Previous mid-IR photometry of AS 310 by Cohen (1974) also shows a silicate emission feature, but more recent observations by Berrilli et al. (1992) indicate a blackbody spectrum.

Both objects are notable in that their near-IR and mid-IR spectra show strong emission features attributed to PAH grains (Jourdain de Muizon et al. 1990; Brooke et al. 1992). As shown in section 7.1, the 7.7 μm feature has a strong influence on the temperature distribution in the environment of AS 310.

In Figure 8-7 I show SEDs for all components of the LkHα 234 system. The primary star may show a slight silicate emission feature and its two companions, LkHα 234-NW and LkHα 234-S, show strong silicate absorption. Neither of the companions have been observed previously with sufficient sensitivity or spatial resolution to detect this feature.

In Figure 8-8 I show both a low resolution SED, where the two central stars of MWC 1080 are unresolved, and a high-spatial-resolution SED for each component of

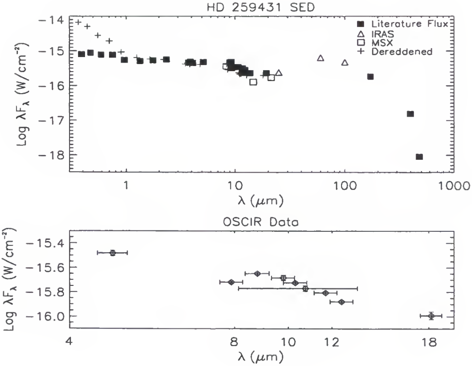

Figure 8-5: Optical to millimeter SED of HD 259431 constructed from data in literature. (*Bottom*) Mid-IR SED of HD 259431 showing possible silicate emission between 8.8 and 9.8 μm. Error bars on the abscissa indicate filter widths, error bars on the ordinate axis are comparable to the size of the data points.

the core binary. Photometry for the components of the close binary was constructed from flux ratios cited in Leinert, Richichi & Hass (1997), Corporan (1998), large aperture literature fluxes for the unresolved pair, and my own OSCIR observations. The V, R I, J, H, and L' magnitudes may include flux from the eastern component of the MWC 1080 system since they were derived from large (>11″) aperture photometry in the literature. A 10 μm silicate emission feature may be present in the SEDs of both the primary and MWC 1080 E.

The SEDs of the two central stars of MWC 1080 appear distinctly different. MWC 1080A exhibits a shallow slope between 0.55 and 3 μm and then a smooth decrease to 18 μm. MWC 1080B's near-IR SED is much flatter, a small rise is seen at 3 μm, however this may be due to contamination of the L' photometry from

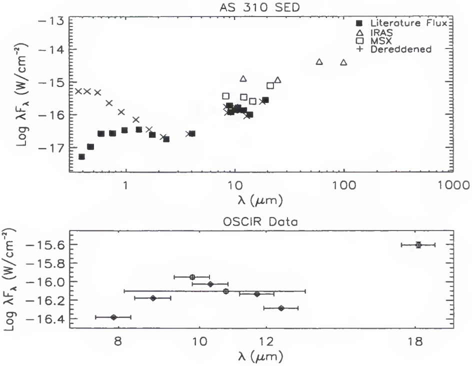

Figure 8-6: Optical to millimeter SED of AS 310 constructed from data in literature. (*Bottom*) Mid-IR SED of AS 310 showing possible silicate emission at ~ 9.8 μm. Error bars on the abscissa indicate filter widths, error bars on the ordinate axis are comparable to the size of the data points.

other stars in the field. Insufficient photometry exists to determine whether either component of the pair has a silicate emission or absorption feature.

The 3/10 μm indices of these stars also show dramatic differences; MWC 1080A has a index ~0.6 and MWC 1080B has a slope ~0.0. Flat indices such as MWC 1080B's have been interpreted as due to a surrounding dust shell, while MWC 1080A's index seems closer to that expected from a circumstellar disk. High spatial resolution 1-3 μm photometry would reveal the true nature of these two stars.

8.5 Color Temperatures and Optical Depths

I have calculated temperatures (T) and emission optical depths (τ) for the dust around HD 259431, AS 310, LkHα 234, and MWC 1080 by applying the method

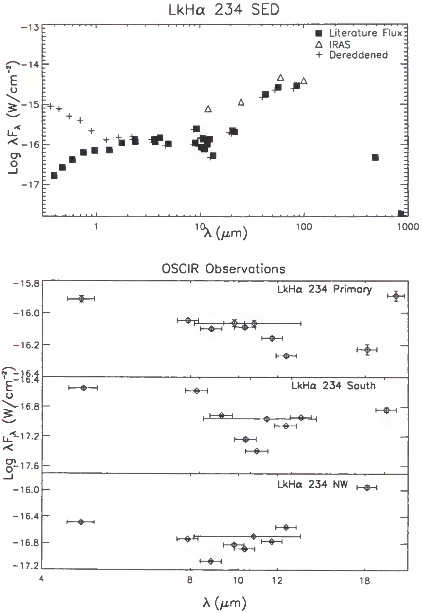

Figure 8-7: (*Top*) Optical to millimeter SED of LkHα 234 constructed from data in literature. (*Bottom*) Mid-IR SEDs of 3 components of the LkHα 234 system. A silicate absorption feature may be present around LkHα 234-S and LkHα 234-NW. Error bars on the abscissa indicate filter widths, error bars on the ordinate axis are comparable to the size of the data points.

described in Chapter 7. I discuss below the mid-IR temperature and optical depth maps derived for HD 259431, AS 310, LkHα 234, and MWC 1080.

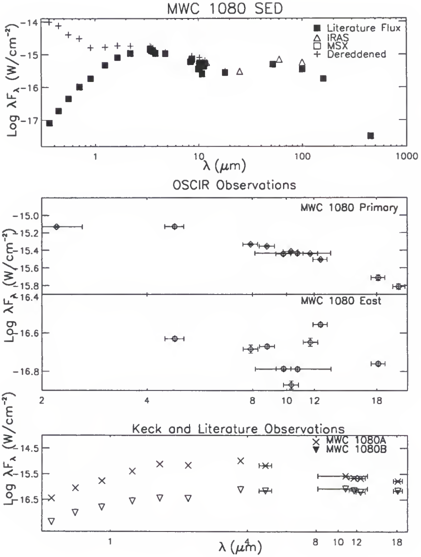

Figure 8-8: (*Top*) Optical to millimeter SED of MWC 1080 constructed from data in literature. (*Middle*) Mid-IR SEDs of the components of the MWC 1080 system. A silicate absorption feature may be present around MWC 1080-E. (*Bottom*) Keck observations of the core binary show different spectral shapes. Error bars on the abscissa indicate filter widths, error bars on the ordinate axis are comparable to the size of the data points.

Table 8-3: Positions and Fluxes (mJy) of Mid-IR Companions

	AS 310-N			LkHα 234-S			LkHα 234-SW			LkHα 234-NW			MWC 1080-E		
Filter	PA(degrees)	Sep (″)	4x4″	PA	Sep	4x4″	PA	Sep	4x4″	PA	Sep	16″ sq	PA	Sep	4x4″
M	...	...	...	176	12.8	450	...	...	...	288	2.8	520	89	5.1	375
N	0.0	4.7	859	175	12.5	394	206	6.5	98	289	3.1	727	89	5.2	584
7.9	...	...	...	175	12.7	687				295	3.2	486	89	5.2	545
8.8				176	12.7	358	...	...	...	296	3.2	250:	88	5.2	627
9.8	...	...	...	175	12.7	190	...	...	...	296	3.1	494	89	5.2	534
10.3	...	...	...	175	12.5	139	...	...	...	291	3.2	452	88	5.2	462
11.7	...	...	...	176	12.7	345	203:	6.6:	36:	291	2.9	664	89	5.2	877
12.5	...	...	...	175	12.6	477	...	...	...	293	3.0	1162	88	5.2	1157
						5.8x5.8″						33″ sq			5.8x5.8″
18.2	...	...	...	175	12.6	875	...	...	...	292	3.1	6777	90	5.3	1052
												36″ sq			
20.8	...	...	...	...	...	...	...	...	...	287	2.8	16960	...	...	...

Table 8-4: Infrared Fluxes in Literature

	HD 259431			AS 310			LkHα 234			MWC 1080		
λ	Mag	beam (″)	ref	Mag	beam (″)	ref	Mag	beam (″)	ref	Mag	beam (″)	ref
1.23	...	...	...	10.34	15	8	...	...	...	...	...	...
1.25	7.43	26	1	...	...	...	9.5	6	11	7.39	...	19
1.63	...	...	...	10.03	15	8	...	...	...	...	...	...
1.65	6.6	26	1	...	...	...	8.22	6	11	5.94	...	19
2.19	...	...	...	9.48	15	8	...	...	...	...	...	...
2.2	5.65	11	2	...	...	...	7.18	6	11	4.75	12	17
3.4	...	...	...	...	...	...	5.86	6	11	...	...	...
3.5	4.5	11	3	...	...	...	...	...	...	3.17	12	17
3.65	4.3	11	3	...	...	...	...	...	...	3.1	26	3
3.79	...	...	...	7.39	15	8	...	...	...	...	...	...
3.85	4.27	11	2	...	...	...	5.48	11	2	3.13	11	2
4.6	...	...	...	...	...	...	5.26	11	16	...	...	...
4.8	3.5	11	3	...	...	...	...	...	...	2.42	12	17
4.9	3.0	11	3	...	...	...	...	...	...	...	...	...
8.38	...	...	...	2.63	15	8	...	...	...	...	...	...
8.4	1.8	11	3	...	...	...	3.28	11	16	1.34	12	17
8.6	2.1	11	3	3.2	11	9	...	...	...	1.1	11	9
8.65	1.65	11	2	...	...	...	2.83	11	2	1.02	11	2
9.6	...	...	...	...	...	...	3.15	11	16	...	...	...
9.69	...	...	...	2.45	15	8	...	...	...	...	...	...
9.97	1.57	11	2	...	...	...	2.54	11	2	0.77	11	2
10	...	...	...	2.45	11	9	2.5	4	11	...	...	...
10.2	...	...	...	...	...	...	3.05	11	16	0.88	...	19
10.8	1.6	11	3	...	...	...	...	...	...	1.45	26	3
10.99	1.39	11	2	...	...	...	2.43	11	2	0.82	11	2
11.0	1.7	11	3	...	...	...	2.51	11	16	...	...	...
11.1	...	...	...	...	...	...	...	...	...	0.81	12	17
11.3	1.55	11	3	2.2	11	9	...	...	...	0.7	11	9
11.55	1.37	11	2	...	...	...	2.19	11	2	0.49	11	2
12.5	...	...	...	...	...	...	2.38	11	16	...	...	...
12.8	1.2	11	3	...	...	...	...	...	...	...	...	...
12.89	...	...	...	1.86	15	8	...	...	...	...	...	...
18	0.1	11	3	-0.1	11	9	...	...	...	-0.3	11	9
19.3	...	...	...	...	...	...	-0.13	11	16	...	...	...
20	...	...	...	...	...	...	11.4	4	11	...	...	...

Table 8-4–continued

	HD 259431			AS 310			LkHα 234			MWC 1080		
λ	F_ν (Jy)	beam ($''$)	ref	F_ν (Jy)	beam ($''$)	ref	F_ν (Jy)	beam ($''$)	ref	F_ν (Jy)	beam ($''$)	ref
40	...	...	...	...	...	...	200	34	12	...	...	...
52	...	...	...	...	...	...	...	...	...	87	37	18
53	...	...	...	...	...	...	390	34	12	...	...	...
80	...	...	...	...	...	...	650	34	12	...	...	...
100	...	...	...	...	...	...	...	...	...	118	37	18
160	82	53	6	...	...	...	...	...	...	97	37	19
370	16	53	6	...	...	...	...	...	...	...	...	...
450	1.13	18	5	...	...	...	60	18	14	4.92	18	5
600	...	...	...	...	...	...	...	...	...	1.61	18	5
750	...	...	...	...	...	...	...	...	...	0.74	18	5
800	...	...	...	...	...	...	4.2	17	14	0.64	17	5
850	...	...	...	...	...	...	3.4	18	14	0.66	18	5
1100	...	...	...	...	...	...	...	...	...	0.25	19	5
1300	...	...	...	0.199	23	10	0.9	9x6	13	0.24	20	5
13000	...	...	...	0.071	44	20	8.0e-3	44	20	...	...	...
36000	1.35e-4	...	7	...	...	...	1.3e-3	0.3	7	1.8e-4	1	7
60000	...	...	...	...	...	...	1.3e-3	...	15	...	...	...
						IRAS						
12	12.8	30	4	51.5	74	4	31.2	60	4	22.8	30	4
25	20.4	30	4	97.6	54	4	95.6	60	4	25.1	30	4
60	128.5	72	4	831.1	90	4	937.3	90	4	141.2	72	4
100	159.2	90	4	1320.2	90	4	1238.0	150	4	191.7	90	4

Fluxes for long wavelength $\lambda \geq 20$ μm data are cited in Jy. PHOTOMETRY REFERENCES.–(1) Dzhakusheva et al. 1988. (2) Berrilli et al. 1987. (3) Cohen 1973. (4) Weaver et al. 1992. (5) Mannings 1994. (6) Casey 1991. (7) Skinner al. 1993. (8) Berrilli et al. 1992. (9) Cohen 1974. (10) Henning et al. 1994. (11) Harvey et al. 1984. (12) Bechis et al. 1978. (13) Henning et al. 1998. (14) Jenness et al. 1995. (15) Cabrit & Bertout 1992. (16) Cohen & Schwartz 1983. (17) Cohen & Schwartz 1976. (18) Harvey et al. 1979. (19) Milkey et al. 1973. (20) Bertout & Thum 1982.

8.5.1 HD 259431

HD 259431 exhibits a strong 11.3 μm PAH line in IRAS spectra. I calculated color temperatures based upon the 11.7 and 18.2 μm fluxes. As Figure 8-9 shows, the warm dusty nebula declines in temperature radially from an elongated central core. The temperature peaks at ~331 K and the average temperature within a 5.8x5.8$''$ aperture is 270 K. The optical depth within the same aperture is 0.00003. The temperature map shows an elongated lobe southeast of the primary, while the optical depth map shows only a central peak. The emission extends ~6″ from the primary. As discussed in section 4.1 the extent of the emission implies the presence of small transiently heated grains.

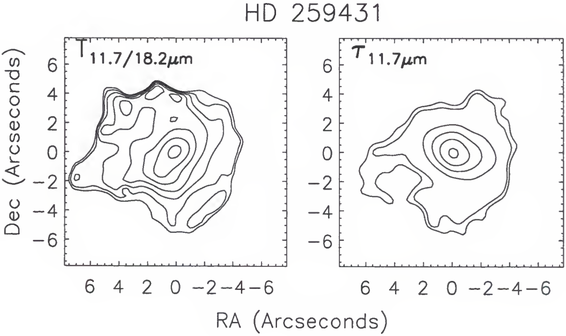

Figure 8-9: HD 259431 11.7/18.2 μm color temperature and optical depth maps. Peak temperature is 331 K and ranges from 200 to 320 K in intervals of 20 K. Peak optical depth is 7.8×10^{-5}; contour intervals are 8×10^{-6}, 1×10^{-5}, and then at intervals of 1.5×10^{-5} to a maximum of 7×10^{-5}.

8.5.2 AS 310

I find that color temperature maps of AS 310 show inverse temperature gradients when temperatures are calculated from bandpasses which include the 7.7 μm PAH emission (Figure 8-10). The 7.9/18.2 μm color temperature map shows that temperatures increase radially away from the position of the central star. Temperatures in the vicinity of the central star range from 175-185 K and then increase to 325-345 K at peak 10″ northwest of the nebula. A color temperature map calculated from the 9.8 and 18 μm observations does not show this inverse temperature gradient;

temperature peaks on the central star at ~213 K and then decreases radially. The average temperature within a 5.8×5.8″ aperture centered on the flux peak is 190 K. Two additional temperature peaks are seen at about 10″ north and 9″ northwest with temperatures of 180-240 and 180-220 K respectively. I speculate that these may be related to embedded sources heating the dust cloud. I offer two possible explanations for the observed color temperature maps. The grains that produce the PAH emission may be destroyed near the luminous primary star but survive further out in the nebula where they emit non-equilibrium radiation which results in the high temperatures. Alternatively, there could be a continuous population of the PAH grains ranging from near the star to large radial distances, but silicate emission may be dominating the flux at locations near the star, and PAH grains dominating the flux at large radial distances. Narrow band CVF imaging, centered on the 7.7 μm PAH feature might help resolve this issue by directly tracing the distribution of the PAH grains.

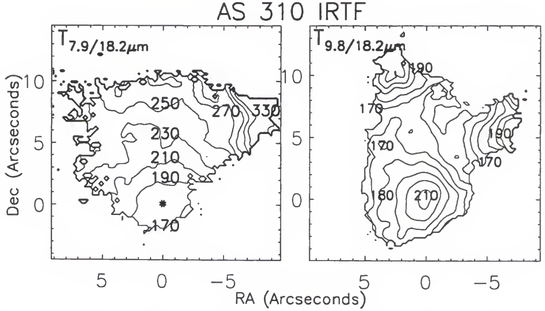

Figure 8-10: AS 310 7.9/18.2 μm and 9.8/18.2 μm color temperature maps. (*Left*) Temperature ranges from 170 to 330 K in intervals of 20 K. (*Right*) Temperature ranges from 150 to 210 K in intervals of 10 K.

8.5.3 LkHα 234

Color temperature maps of LkHα 234 do not show evidence of strong 7.7 μm PAH emission (Figure 8-11). The 9.8/18 μm map shows complex hot structure associated with the primary, and cooler (135-145 K) material at the position of the northwest companion, as well as a warm southern source (175-230 K). The optical depth maps shows that the highest mid-IR optical depths are associated with the companion. I find a 9.8 μm optical depth of 0.37 within a 5.8x5.8″ aperture centered on the northwest source and a maximum τ of 0.0001 for the primary. This supports observations that the NW companion is more heavily embedded than the primary and associated with more dusty material. The optical depth within an aperture enclosing the southern source is ~ 0.00002.

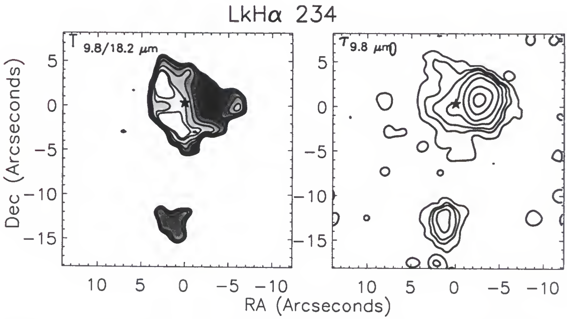

Figure 8-11: LkHα 234 9.8/18.2 μm color temperature and optical depth maps. Contours are overlaid on grey scale for clarity; where lighter colors indicate higher temperatures. Temperature ranges from 130 to 270 K at intervals of 130, 150, 170, 200, 230, 260, and 270 K. The temperature at the position of the flux peak, indicated by the star, is ~264 K. The southern source has a color temperature ~170 K. Optical depth is at intervals of 1×10^{-6}, 1×10^{-5}, 2.5×10^{-5}, 7.5×10^{-5}, 2.5×10^{-4},1×10^{-3}, and 2.5×10^{-3}. The primary is indicated by a star on the temperature map. The optical depth peak, 0.0037, is coincident with the location of the NW companion.

8.5.4 MWC 1080

High-spatial-resolution imaging from Keck resolves the two core components of MWC 1080 and enables a comparison of their color temperatures. An 11.7/18.2 μm color temperature map shows an elongated lobe of hotter material (350 K) associated with the primary star at a position angle almost directly due north (Figure 8-12). This lobe is embedded within an envelope of cooler material (260-280 K) and outermost knots of hot material. The emission optical depth map shows a peak associated with the companion (τ ~0.00097), and a secondary peak at the position of the primary ($\tau \sim 0.0007$). I conclude that the hottest material is associated with a lobe aligned with the primary. The north-south elongation of this lobe could be due to high optical depth material being present in the E-W plane than the north-south plane. Cooler, higher optical depth material surrounds the secondary star; this object may be more embedded than the primary star. In addition, while the primary star's flux declines sharply towards 18 μm, the secondary star presents a shallower slope, indicating additional flux from cooler material again implying that it is more embedded.

8.6 Summary

I have analyzed mid-IR observations of four Hillenbrand Group I circumstellar disk candidates. All objects have large extended dust envelopes. HD 259431 shows large-scale extended emission beyond that expected for grains in thermal equilibrium. This emission may originate in transiently heated grains who signature appears in IRAS spectra. Up to 30% of the 7-18 μm flux originates in the surrounding dust envelope.

AS 310's mid-IR flux is dominated by emission from a dust envelope and embedded sources. 70% of the flux originates in sources unrelated to disk phenomena. In addition, the mid-IR color temperature suggests a strong contribution from transiently heated grains.

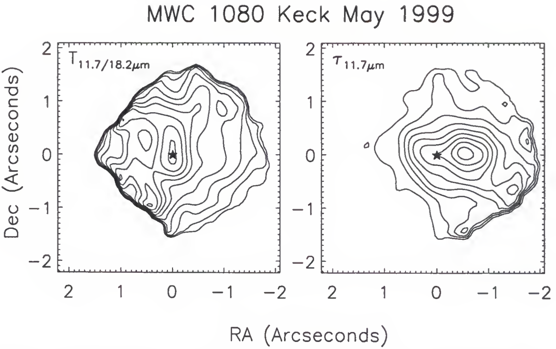

Figure 8-12: MWC 1080 11.7/18.2 μm color temperature and optical depth maps. Peak temperature is 356 K and contours range from 170 to 350 K in intervals of 20 K. Optical depth ranges from 0.0001 to 0.0009 in intervals of 0.0001.

I have discovered a new mid-IR companion to LkHα 234, as well as extended structure around the northwest companion suggestive of a disk. The companion dominates the mid-IR flux at 18 μm, exhibits a silicate absorption feature, and is coincident with the peak 9.8 μm optical depth. These characteristics, and the observations of a CO outflow, and water masers in the vicinity of this source support the suggestion of a disk for the NW companion rather than the primary star.

The core binary of MWC 1080 is resolved in the mid-IR and the system is found to show large-scale structure that may be due to tidal interactions between the multiple components in this system. Mid-IR color temperature and optical depth maps show that warmer material is associated with the A component, while the peak optical depth is associated with the B component. SEDs for each component may indicate different evolutionary stages for the two stars. MWC 1080A's SED appears similar to that expected from a disk, while MWC 1080B's SED may be more characteristic of an object embedded in a dense dusty envelope.

Clearly, the dusty environments of Ae/Be stars are more complicated than previously assumed. High-spatial-resolution long wavelength observations can help resolve some questions concerning the nature of these environments.

CHAPTER 9
SUMMARY AND CONCLUSIONS

This research presents for the first time a high-spatial-resolution mid-IR study of the circumstellar environments of the intermediate mass pre-main-sequence stars, the Herbig stars. Although the mid-IR emission of these objects has long been attributed to emission from a circumstellar disk, until recently no instrumentation was able to probe these regions with sufficient spatial resolution to confirm this geometry.

My research shows that the mid-IR emission of Ae/Be stars is not confined to an optically thick disk, but originates in a number of physical processes. In a survey of 21 fields, I find numerous embedded companions as well as large scale extended emission around seven objects. Over half the sample, 11/21 fields, show significant excesses related to either companions or large-scale extended emission. The contribution of extended emission and companions to the total mid-IR emission ranges from 12% to 73%. The extended emission shows a wide range of morphologies, with only one object, a deeply embedded companion to LkHα 234, possibly showing disk-like structure. Several objects show marginally resolved extended emission on a scale of a few arcseconds. HST imaging of one such object, HD 100546, shows that it possesses a circumstellar disk that may be the origin of the extended emission. For most of the resolved objects the excess flux is dominated by emission from embedded companions. However, in two cases, AS 310, and AFGL 2136, the extended emission from non-disk sources dominates the mid-IR flux distribution.

Deep 10 and 18 μm imaging of the RNO 1B region has revealed several 18 μm sources that are associated with near-IR polarimetric peaks. One of these objects may be coincident with an IRAS far-IR peak that powers a strong outflow as well as maser emission that is aligned in a disk-like geometry. This complex and dynamic region also includes two FU Orionis stars, one of which is resolved at 18 μm and has a source size of 730 AU. If this emission arises in a circumstellar disk, it would be one of the largest disks measured in the infrared.

High-spatial-resolution imaging of the MWC 1080 system conducted with the Keck telescope resolves the core binary and shows structure which could be tidal in nature. This system possesses at least four members in the mid-IR and several more in the near-IR. Interaction between the companions may have produced the tidal arms structure.

I calculated new spectral indices of the mid-IR sources, using small aperture photometry, which excluded emission from companions or envelopes. This new photometry changes the Hillenbrand evolutionary class for seven objects, and I derive evolutionary classes for the first time for six objects. There is no clear correlation between evolutionary class determined from the 3/10 μm index and age of the star. However, an examination of the shape of the SED between 3 and 18 μm suggests possible dust geometries and gives clues as to the evolutionary stage of the objects.

The spectral indices of most of the sample are much flatter than expected from a geometrically-thin, optically thick circumstellar disk. A histogram of the 3/10 μm spectral indices indicates that they peak outside the regime expected for the classical disk model. However, the broad peak does encompass the spectral indices expected from flared disk models. The width of the peak can be used to constrain the scale height of a flared disk. My small sample indicates that the scale height for a flared disk probably lies between the two canonical values of $R^{9/8}$ and $R^{5/4}$.

Mid-IR SEDs were determined for the first time for several objects, including the separate components of several binary systems. The SEDs of V 1318 Cyg N and S confirm the presence of a silicate absorption feature seen in low spatial resolution ISO spectroscopy. I show that both components of this system possess the feature. I also resolve separate mid-IR SEDs for the XY Per binary system; the primary component is seen to possess a silicate feature while the SED of the companion is featureless. An optical to mid-IR SED was assemble for the first time for the separate components of the MWC 1080 binary system. This SED indicates that one object is substantially more embedded than the other and may be at an earlier evolutionary stage.

V-N colors were derived for all objects in the sample for which optical and mid-IR data was available. A plot of the V-N color excess versus spectral type shows that Group I and Group II objects are well mixed and do not lie in specific color spaces. This observation is in disagreement with Hillenbrand et al. (1992) who find that Group I and II objects occupy different color spaces in a diagram of V-12 μm excess. I find that IRAS colors are probably contaminated by emission from extended envelopes, embedded companions, and other sources within the same large beam. Other authors have also noted that IRAS fluxes may be subject to source confusion due to the large beam size of the instrument (Ábrahám et al. 2000). IRAS fluxes overestimate the true fluxes of several objects in the sample, and cause sources to appear redder than measurements made with small aperture photometry. Two objects, (HD 97048 N, and AFGL 2136), show discrepant V-N colors which may be due to incorrect or anomalous extinction laws.

Mid-IR color temperatures of the the sample help constrain the sizes of the dust emitting regions, and in two cases (HD 100546, RNO 1C), give diameters for the thermal emission that are similar to the extent of circumstellar disks. Color temperature maps of the extended emission suggest the presence of small transiently heated grains as well as larger silicate grains. In particular, the temperature map of AS 310 shows a clear inverse temperature gradient which could be produced by transiently heated grains such as PAHs. The color temperature of V 921 Sco is more difficult to interpret, but also indicates a transiently heated component to the grain population. Optical depth maps of the binary system MWC 1080 A and B indicate that the B component is associated with the most dust, while the color temperature peaks on the A component.

In the 21 fields I surveyed, 11 objects show other mid-IR sources within the same field. Of the remaining objects one has a companion within 35″ and another has a companion at optical wavelengths. I find that 62% of my sample have companions within 12,000 AU. This frequency is almost three times the frequency found for main sequence A and B stars. A more rigorous search for mid-IR companions needs to be conducted to confirm this preliminary estimate.

The origin of the mid-IR emission remains unresolved for nine objects in my sample. I do not find companions or extended emission that contribute significantly to the flux of these objects. The source of the emission must lie too close to the star to be resolved with the instruments used in this research. My observations place limits on disk sizes and constrain models of these sources. While I cannot determine the geometry of the emission of the unresolved sources, the spectral indices suggest that the classical geometrically-thin disk model may be inappropriate. My observations suggest that a flared disk model might better fit the SEDs of these stars. Clearly, the dusty environments of Ae/Be stars are more complicated than previously assumed. High-spatial-resolution observations are essential to reveal the origin of the emission and the geometry of the dust in these environments.

9.1 Suggestions for Future Work

Several avenues of research could complement and augment the mid-IR imaging results presented here. Many of the sources in the sample are new detections or have never been studied outside the mid-IR. In addition some objects show strong evidence that they may possess disks. Followup observations might be able to confirm the presence disks. Finally, detailed circumstellar disk models should be developed and tested against the new observations. I discuss below several critical observations that would expand upon the research discussed above.

9.1.1 Mid-IR Observations

Most of this research was conducted at three meter class observatories with typical resolutions of 0.6″. However, new instrumentation has become available at larger telescopes, such as the Gemini 8 meter and Keck 10 meter telescopes, which can achieve spatial resolutions better than 0.3″, and can therefore image circumstellar regions closer to the central stars. In particular, the objects LkHα 234 NW and RNO 1C, which show attributes associated with disks, should be re-observed with higher spatial resolution and higher signal-to-noise in the mid-IR.

Spatially-resolved mid-IR spectroscopy is also vitally needed for almost all objects in the sample. Little spectroscopy, outside IRAS LRS spectra, for the brightest sources, exists. Ground-based observatories such as Gemini and Keck now possess mid-IR spectrometers and SIRTF instrumentation will also include a a spectrometer with sensitivities exceeding those available at ground-based observatories. Mid-IR spectroscopy can unambiguously identify spectral features associated with different grain chemistries and dust temperatures. Limited spectroscopy conducted with ISO indicates that the shape of the silicate feature may change in different star-forming regions. My diverse sample of objects is well suited to a study of this nature.

9.1.2 SIRTF Observations

With the exception of the IRAS survey, and some observations with the KAO little study has been conducted of the far-IR properties of Herbig stars. The SEDs of many objects appear to peak in the far-IR, yet it is unknown whether this emission can be attributed to a disk or other sources. The far-IR population of regions such as RNO 1B and BD +40 4124 is also poorly known. Some studies with KAO suggest that there may be a large population of embedded objects in these regions that remain undetected at shorter wavelengths. SIRTF, which will be launched in 2002, will have 20″ resolution in the far-IR, and millijansky sensitivity, far exceeding the capabilities of either IRAS or KAO. In addition, SIRTF instrumentation will include a low spectral resolution 50-100 μm spectrometer. This unique capability will help decipher the infrared SEDs of Ae/Be stars and will enable a more accurate comparison to be made between observed SEDs and disk models.

9.1.3 Millimeter Observations

Millimeter observations can provide important diagnostic information concerning the structure, mass, and temperature of the dust in Herbig star environments. Millimeter continuum mapping of Herbig stars can reveal the morphology of the dust, and, since the emission from cold dust is optically thin in the millimeter, these observations will provide an estimate of the dust mass around Ae/Be stars. This parameter is essential to determining whether sufficient mass exists for disks and planets to form and may also be linked to the evolutionary stage of the system. Imaging within spectral features such as CO, could show the locations of outflow phenomena in Herbig star environments. Since outflows are assumed to form perpendicular to the axes of disks, these maps could point to the locations of disks which are not detectable at shorter wavelengths. For example, the Herbig star LkHα 234 is associated with a CO outflow and at least four mid-IR sources (Mitchell & Matthews 1994; Edwards & Snell 1983; Cabrit et al. 1997). My observations, with the University of Florida mid-IR camera, OSCIR, indicate that one of these sources exhibits emission suggestive of a circumstellar dust disk. This hypothesis would be supported if the outflow was found to be perpendicular to the axis of the extended mid-IR emission. Unfortunately, the resolution of the best submillimeter CO map is 14″ and it is unknown which of the mid-IR sources the outflow is associated with. In addition, kinematic maps of CO line emission may be possible for the nearer objects and can reveal dynamical information such as velocity differentials which can indicate rotating disks.

The recent discoveries of extrasolar planets have spurred investigations of pre-main-sequence stars and their environments. Theory suggests that planets form in dusty circumstellar disks around young stars. Many young stars exhibit large excesses of infrared emission that have been attributed to circumstellar disks. The circumstellar environments of Herbig stars remain relatively unexplored, and it is as yet uncertain whether these stars possess the appropriate conditions to form planets. New high-spatial-resolution mid-IR observations reveal that the thermal emission from the environments of many Herbig stars originates in embedded companions and large-scale envelopes. Revised SEDs suggest that some of these objects may also possess disks, but imply a flared geometry for the disks rather than the widely used geometrically-thin disk model. If these objects do possess disks they are too close to the star to be resolved by instrumentation used in this study. My results call for further investigation of these objects with higher spatial resolution, in the infrared and millimeter; further observations have the potential to resolve some of the puzzles of this diverse class of objects.

APPENDIX A
APPENDIX: IDL CODE

A.1 Photometry Tool

Below I show the simple IDL code I developed for interactive photometry of mid-IR images. The code takes as input the image name, and a desired aperture size. It displays the image and requires the user to click where the aperture is desired. The code then calculates a centroid and displays a new window showing the aperture region and the total flux enclosed, in millijanskies. The user can then adjust the aperture location and remeasure the total flux. Upon exiting the code closes all the interactive windows.

```
; NAME:
;
;    APHOT.PRO
;
; PURPOSE:
;A program to do interactive aperture photometry.
;The program display the image, user clicks on desired source.
;The program finds the max, and creates a square aperture around it.
;Then displays it to the screen. It asks if you like the aperture.
;User can input new x1, y1 values and it will redisplay the aperture
;and check if you like the new aperture.
;It will run this loop until you respond other than 'y'.
;
; CALLING SEQUENCE:
;
; aphot, image, width
; INPUTS:
;
;      image  -- name of the array containing image data
;      width  -- width of aperture in pixels
; OPTIONAL INPUT:
; User can modify the aperture location. The program will query
;       whether this is desired, if 'y', new aperture locations are requested.
;
; OUTPUT:
; Prints to the screen x1,x2, y1, y2 the aperture location.
;       Prints to screen the total flux in aperture
;
;    EXTERNAL CALLS
;  Calls routine disp.pro, written by R. Pina.
; REVISION HISTORY:
; June 2000  -- Written by Elisha Polomski UFIAG
```

```
pro aphot,im,width

;size of image
sz=size(im)
x=sz[1]
y=sz[2]

image=im
wins=indgen(20)


i=0
status=''

;display your image
mydisp,image,curr_win=curr_win

;delete this window at the end of the routine
delme=curr_win
cursor,a,b

imfil=mfilter(im,gauss=3)



pk=max(imfil[(a-10):(a+10),(b-10):(b+10)])
loc=where(imfil eq pk)


mx=fltarr(2)
mx[1]=floor(loc/x)

xpk=(float(loc)/float(x)-mx[1])*x

mx[0]=round(xpk)

;Size the aperture around the max
if width/2.0 eq floor(width/2) then begin

;even width
x1=max(mx[0]-(width/2))
x2=max(mx[0]+(width/2)-1)
y1=max(mx[1]-(width/2))
y2=max(mx[1]+(width/2)-1)
endif else begin

;odd width
x1=max(mx[0]-((width-1)/2))
x2=max(mx[0]+((width-1)/2))
y1=max(mx[1]-((width-1)/2))
y2=max(mx[1]+((width-1)/2))
endelse

print,x1,x2,y1,y2,format='(i3,1x,i3,1x,i3,1x,i3)'

while (status ne 'y') do begin
mydisp,image[x1:x2,y1:y2],curr_win=curr_win

tot=total(image[x1:x2,y1:y2])
print,x1,x2,y1,y2,format='(i3,1x,i3,1x,i3,1x,i3)'
print,'Total: ',tot
```

```
wins[i]=curr_win

print,'Good Centering?(y/n)'
read,status

if status eq 'y' then goto, good
i=i+1
print,'New x1?'
read,x1new
print,'New Y1?'
read,y1new

delx=x1-x1new
dely=y1-y1new
y1=y1new
x1=x1new
x2=x2-delx
y2=y2-dely

endwhile

good:
tot=total(image[x1:x2,y1:y2])
print,tot

;get rid of all those windows at end of program
for index=0,i do begin
wdelete,wins[index]
endfor

;delete the first window we brought up
wdelete,delme
end
```

A.2 Color Temperature Code

This code calculates color temperatures and emission optical depths from mid-IR photometry. The user inputs the fluxes in Janskys for two wavelengths, and the optical extinction towards the source. The code assumes a circumstellar extinction law $\propto 1/\lambda$. The code then uses a Newton-Rapheson iteration to solve for the temperature and optical depth, based upon the two observed fluxes, and the extinction law.

```
; NAME:
;
; COLOR
;
; PURPOSE:
;
; Computes the Temp and Tau(circumstellar) for 2 input fluxes.
; The program first calculates the ism attenuation by
; interpolating in a table of Aλ/Av from Rieke+Lebofsky to
; the input wavelengths. Then using the input Av,
; it calculates Aλ at the desired wavelengths.
; Tau ism then is simply tau=Av/1.086.
; Then it assume a planck function and a 1/λ power law
; for the circumstellar extinction and uses the observed fluxes to solve
; for T and Tau, given initial guesses.
; Fλ=Ω*B(T, λ)*(1-exp(τλ))*exp(τism)
; Fλ is the observed flux in Janskies
; omega is the solid angle (radians) [″²]/[(206265²]
;  Since two fluxes are known, there are two equations of the above form.
; The third equation is the relationship between the two circumstellar Tau.
; i.e. Tau1/Tau2=lambda2/lambda1
; All calculations are done in CGS units.
;
; 1 Jy= 1 e -26 W/m^2/Hz
; 1 Jy= 1 e -23 erg/cm^2 s/Hz
; xJy= 3 e-16*x/(lambda^2)    ----lambda in microns----erg/cm^2 s/micron

; Note that for an unresolved source, Tau cannot be solved for.
; The actual source size, omega is not known, only an upper limit,
; for unresolved sources.
;
;
; CALLING SEQUENCE:
;
; color, flux1, flux2, Av, lambda1, lambda2
;
;
;
; INPUTS:
;
; flux1 -- flux at wavelength 1 in Janskys
; flux2 -- flux at wavelength 2 in Janskys
; Av -- optical extinction to the source.
; lambda1 -- wavelength of flux1
; lambda2 -- wavelength of flux2

function newtfunc, VEC

;all units are CGS
common fnus, f1, f2,l1,l2,tau1,tau2
 c=2.998d+10  ; cm sec^-1

;omega=solid angle of a pixel or resolution element
; omega=8.919d-14 ;.0616^2 KECK
;   omega=1.1688d-12   ; (0.223arcsec^2) IRTF
; omega=7.869d-13 ; (0.183 arcsec^2)CTIO

omega2=7.08e-10 ;ctio 30x30 pixels
omega1=2.84e-10 ;ctio 19x19 pixels
; omega=3.76e-10 ; 4 arcsec square
```

```
ism1=exp(-tau1)
ism2=exp(-tau2)
nu1=c/l1
nu2=c/l2

;dont let temperature become negative or too large
  T=VEC[0]>5

;emissivity law goes in denominator of func2-exp(-VEC[1]/emissivity law)
  func1 = omega1*planck(nu1,T)*(1.0 - exp(-VEC[1]))*ism1
  func2 = omega2*planck(nu2,T)*(1.0 - exp(-VEC[1]/(l2/l1)))*ism2

  return,[1.0-func1/f1,1.0-func2/f2]

  end


function planck, nu, T

  h=6.626d-27  ; gm cm^2 sec^-1
  k=1.381d-16  ; gm cm^2 sec^-2 K^-1
  c=2.998d+10  ; cm sec^-1

  return,(2.0*h*nu^3/c^2)/(exp(h*nu/(k*T))-1.0)

  end


pro color, fl1, fl2, abv, la1, la2
common fnus, f1,f2,l1,l2,tau1,tau2
ism=fltarr(2,390)



;l1,l2 in micron,convert to cgs
;f1, f2 convert to erg/cm2 s /hz from Jy
f1=fl1*1e-23
f2=fl2*1e-23
av=abv


;cgs
l1=la1*1e-4
l2=la2*1e-4



;Read in the ism alambda/av into the array ism(2,390)
;file format is microns, alambda/av
openr,1,"/home/callisto0/elwood/idl/ism.dat"
readf,1,ism
close,1

;fit a spline
y2=spl_init(ism[0,*],ism[1,*],/double)
;tau=Alambda/1.086
tau1=(spl_interp(ism[0,*],ism[1,*],y2,l1*1e4))*av/1.086
tau2=(spl_interp(ism[0,*],ism[1,*],y2,l2*1e4))*av/1.086

;initial guesses of temp, tau
  init=[300.0,0.000001]
```

```
;call the IDL routine newton with initial value init and subroutine newtfunc
  res=newton(init,'newtfunc',/double,itmax=1500,step=1)
print,res
end
```

REFERENCES

Ábrahám, P., Leinert, C., Burkert, A., Henning, T. & Lemke, D. 2000, A&A, 354, 965

Ageorges, N., Eckart, A., Monin, J. -. & Menard, F. 1997, A&A, 326, 632

Aitken, D. K. & Roche, P. F. 1981, MNRAS, 196, 39P

Allamandola, L. J., Tielans, A. G. G. M., & Barker, J. R. 1989, ApJS, 71, 733

Allen, D. A. 1973, MNRAS, 161, 145

Allen, D. A., Hyland, A. R., Longmore, A. J., Caswell, J. L., Goss, W. M. & Haynes, R. F. 1977, ApJ, 217, 108

Altenhoff, W. J., Thum, C. & Wendker, H. J. 1994, A&A, 281, 161

Ambartsumian, V. A. 1947, Stellar Evolution and Astrophysics, Erevan, Armenia, SSR, Academy of Science

Appenzeller, I., Oestreicher, R. & Jankovics, I. 1984, A&A, 141, 108

Aspin, C., Sandell, G. & Weintraub, D. A. 1994a, A&A, 282, L25

Aspin, C., Sandell, G., Weintraub, D. & Blanco, P. 1994b, in ASP Conf. Ser. Vol. 62, The Nature and evolutionary Status of Herbig Ae/Be Stars, ed. P. S. Thé, M. R. Pérez, & P. J. van den Heuvel (San Francisco: ASP),ASP Conf. 351

Asselin, L., Ménard, F., Bastien, P., Monin, J. & Rouan, D. 1996, ApJ, 472, 349

Aumann, H. H., Beichman, C. A., Gillett, F. C., de Jong, T., Houck, J. R., Low, F. J., Neugebauer, G., Walker, R. G., Wesselius, P. R. 1984, ApJ, 278, L23

Bachiller, R. 1996, ARA&A, 34, 111

Bastian, U. & Mundt, R. 1979, A&AS, 36, 57

Bastien, P. & Ménard, F. 1990, ApJ, 364, 232

Bechis, K., Harvey, P., Campbell, M., & Hoffman, W. 1978, ApJ, 226, 439

Beckwith, S. V. W. 1994, in Star Formation and Techniques in Infrared and mm-Wave Astronomy, ed. . P. Ray & S. V. W. Beckwith (New York:Springer Verlag), 157

Beckwith, S. V. W. 1999, in The Origin of Stars and Planetary Systems, ed. C. J. Lada & N. D. Kylafis (Dordrecht:Kluwer), 579

Beichman, C., Myers, P., Emerson, J., Harris, S., Mathieu, R., Benson, P., & Jennings, R. 1986, ApJ, 307, 337

Beichman, C. A., Neugebauer, G., Habing, H. J., Clegg, P. E., & Chester, T. J. 1988, Infrared Astronomical Satellite Explanatory Supplement (DC: NASA)

Benedettini, M., Nisini, B., Giannini, T., Lorenzetti, D., Tommasi, E., Saraceno, P. & Smith, H. A. 1998, A&A, 339, 159

Berrilli, F., Corciulo, G., Ingrosso, G., Lorenzetti, D., Nisini, B. & Strafella, F. 1992, ApJ, 398, 254

Berrilli, F., Lorenzetti, D., Saraceno, P., & Strafella, F. 1987, MNRAS, 228, 833

Blades, J. C. & Whittet, D. C. B. 1980, MNRAS, 191, 701

Blondel, P. F. C. & Djie, H. R. E. T. A. 1994, in ASP Conf. Ser. Vol. 62, The Nature and evolutionary Status of Herbig Ae/Be Stars, ed. P. S. Thé, M. R. Pérez, & P. J. van den Heuvel (San Francisco: ASP), 211

Bodenheimer, P. 1995, ARA&A, 33, 199

Böhm, T. & Catala, C. 1994, A&A, 290, 167

Boss, A. P. & Yorke, H. W. 1996, ApJ, 469, 366

Bowers, R., & Deeming, T. 1984, Astrophysics I, Stars (Boston:Jones and Bartlet Inc.)

Breger, M. 1974, ApJ, 188, 53

Brooke, T. Y., Tokunaga, A. T. & Strom, S. E. 1993, AJ, 106, 656

Cabrit, S., Lagage, P., McCaughrean, M. & Olofsson, G. 1997, A&A, 321, 523

Calvet, N., Hartmann, L., Kenyon, S. J. & Whitney, B. A. 1994, ApJ, 434, 330

Cambrésy, L., Copet, E., Epchtein, N., de Batz, B., Borsenberger, J., Fouquè, P., Kimeswenger, S. & Tiphène, D. 1998, A&A, 338, 977

Cantó, J., Rodriguez, L. F., Calvet, N. & Levreault, R. M. 1984, ApJ, 282, 631

Caswell, J. L., Vaile, R. A., Ellingsen, S. P. & Norris, R. P. 1995, MNRAS, 274, 1126

Catala, C. 1988, A&A 193, 222

Catala, C. & Bertout, C. 1990, Evolution in Astrophysics: IUE Astronomy in the Era of New Space Missions, ed. E. J. Rolfe, (Netherlands: ESA Publications Division), 11

Chandrasekhar, S. 1939, An Introduction to the Study of Stellar Structure (Chicago: University of Chicago Press)

Chiang, E. I. & Goldreich, P. 1997, ApJ, 490, 368

Ciardi, D., Akeson, R., van Belle, G. T. & Lada, E. A. 1999, BAAS, 195, 4905

Cohen, M. 1972, ApJ, 173, L61

Cohen, M. 1973a, MNRAS, 161, 97

Cohen, M. 1973b, MNRAS, 161, 105

Cohen, M. 1974, MNRAS, 169, 257

Cohen, M., Bieging, J. H. & Schwartz, P. R. 1982, ApJ, 253, 707

Cohen, M., & Kuhi, L. H. 1979, ApJS, 41, 743

Cohen, M., Schwartz, D. E., & Chokshi, A., & Walker, R. G. 1987, AJ, 93, 1199

Cohen, M., Walker, R. G., Carter, B., Hammersley, P., Kidger, M. & Noguchi, K. 1999, AJ, 117, 1864

Corcoran, M. & Ray, T. P. 1997, A&A, 321, 18

Corcoran, D., Ray, T. P. & Bastien, P. 1995, A&A, 293, 550

Corporan, P. & Lagrange, A. M. 1999, A&AS, 136, 429

Damiani, F., Micela, G., Sciortino, S., & Harnden, F. R., Jr. 1994, ApJ, 436, 807

Deutsch, L. K., Hora, J. L., Butner, H. M., Hoffman, W. F. & Fazio, G. G. 1995, Ap&SS, 224, 89

de Winter, D., Grady, C. A., van den Ancker, M. E., Pérez, M. R., & Eiroa, C. 1999, A&A, 343, 137

de Winter, D. & Thé, P. S. 1990, Ap&SS, 166, 99

Dibai, E. A. 1969, Astrofizika, vol 5, no 2, 249

Di Francesco, J., Evans, N. J., Harvey, P. M., Mundy, L. G. and Butner, H. M. 1994, ApJ, 432, 710

Dinger, A. S. C., Dickinson, D. F., Gottlieb, C. A. & Gottlieb, E. W. 1979, PASP, 91, 830

Draine, B. T., & Lee, H. M. 1984, ApJ, 285, 89

Drew, J. E., Busfield, G., Hoare, M. G., Murdoch, K. A., Nixon, C. A. & Oudmaijer, R. D. 1997, MNRAS, 286, 538

Duquennoy, A. & Mayor, M. 1991, A&A, 248, 485

Elitzur, M. , Hollenbach, D. J. & McKee, C. F. 1989, ApJ, 346, 983

Emerson, D, 1996, Interpreting Astronomical Spectra (NY: John Wiley & Sons Ltd)

Evans, A. 1994, in The Dusty Universe (NY: John Wiley & Sons Ltd)

Evans, N. J. & Di Francesco, J. 1995, Revista Mexicana de Astronomia y Astrofisica Conference Series, 1, 187

Fabricius, C. & Makarov, V. V. 2000, A&A, 356, 141

Feigelson, E. D., Casanova, S., Montmerle, T. & Guibert, J. 1993, ApJ, 416, 623

Fiebig, D., Duschl, W. J., Menten, K. M. & Tscharnuter, W. M. 1996, A&A, 310, 199

Finkenzeller, U., & Mundt, R. 1984, A&AS, 55, 109

Fouque, P., Le Bertre, T., Epchtein, N., Guglielmo, F. & Kerschbaum, F. 1992, A&AS, 93, 151

Fuente, A., Martín-Pintado, J., Bachiller, R., Neri, R., & Palla, F. 1998, A&A, 334, 253

Gaylard, M. J. & Whitelock, P. A. 1988, MNRAS, 235, 123

Georgelin, Y. M., & Georgelin, Y. P. 1970, A&A, 6, 349

Ghez, A. M., McCarthy, D. W., Patience, J. L.& Beck, T. L. 1997, ApJ, 481, 378

Ghez, A. M., Neugebauer, G. & Matthews, K. 1993a, AJ, 106, 2005

Ghez, A. M., Neugebauer, G. & Matthews, K. 1993b, PASP, 105, 951

Gillett, F. C, Forrest, W. J., Merrill, K. M., Capps, R. W., & Soifer, B. T. 1975, ApJ, 200, 609

Gorti, U. & Bhatt, H. C. 1993, A&A, 270, 426

Grady, C. A., Pérez, M. R., Bjorkman, K. S. & Massa, D. 1999, ApJ, 511, 925

Grady, C. A., Perez, M. R., Talavera, A., Bjorkman, K. S., de Winter, D., The, P. -S., Molster, F. J., van den Ancker, M. E., Sitko, M. L., Morrison, N. D., Beaver, M. L., McCollum, B. & Castelaz, M. W. 1996a, A&AS, 120, 15

Grady, C. A., Perez, M. R., Talavera, A., McCollum, B., Rawley, L. A., England, M. N. & Schlegel, M. 1996b, ApJ, 471, L49

Grady, C. A., Perez, M. R., Thé, P. S., Grinin, V. P., de Winter, D., Johnson, S. B. & Talavera, A. 1995, A&A, 302, 472

Grady, C. A., Polomski, E. F., & Gull, T. 2001, AJ, 121, 109

Grady, C. A., Sitko, M. L., Bjorkman, K. S., Perez, M. R., Lynch, D. K., Russell, R. W. & Hanner, M. S. 1997, ApJ, 483, 449

Graham, J. A. & Chen, W. P. 1991a, BAAS, 23, 1374

Graham, J. A. & Chen, W. P. 1991b, AJ, 102, 1405

Gray, D. F. 1992, in The Observation and Analysis of Stellar Photospheres, (Cambridge:Cambridge University Press)

Gregorio-Hetem, J., Lépine, J. R. D., Quast, G. R., Torres, C. A. O., & De La Reza, R. 1992, AJ, 103, 549

Gürtler, J., Schreyer, K., Henning, T., Lemke, D. & Pfau, W. 1999, A&A, 346, 205

Hage, J. I. & Greenberg, J. M. 1990, ApJ, 361, 251

Hajjar, R. & Bastien, P. 2000, ApJ, 531, 494

Hamaguchi, K. , Terada, H. , Bamba, A. & Koyama, K. 2000, ApJ, 532, 1111

Hamann, F. & Persson, S. E. 1992, ApJ, 394, 628

Han, F. F., Mao, R. Q., Lu, J., Wu, Y. F., Sun, J., Wang, J. S., Pei, C. C., Fan, Y., Tang, G. S., & Ji, H. R. 1998, A&AS, 127, 181

Hanner, M. S., Brooke, T. Y., & Tokunaga, A. T. 1994a, ApJ, 433, L97

Hanner, M. S., Brooke, T. Y. & Tokunaga, A. T. 1998, ApJ, 502, 871

Hanner, M. S., Lynch, D. K. & Russell, R. W. 1994b, ApJ, 425, 274

Hanner, M. S., Tokunaga, A. T., Veeder, G. J., & A'Hearn, M. F. 1984, AJ, 89, 162

Harris, S., Clegg, P., & Hughes, J. 1988, MNRAS, 235, 441

Hartmann, L. in Accretion Processes in Star Formation, 1998, (Cambridge:Cambridge University Press)

Hartmann, L., Kenyon, S. J., & Calvet, N. 1993, ApJ, 407, 219

Hauschildt, P. H., Allard, F. & Baron, E. 1999, ApJ, 512, 377

Hayashi, C. 1966, ARA&A, 4, 171

Henning, T., Burkert, A., Launhardt, R., Leinert, C. & Stecklum, B. 1998, A&A, 336, 565

Henning, T., Launhardt, R., Steinacker, J. & Thamm, E. 1994, A&A, 291, 546

Henning, T., Pfau, W., Zinnecker, H. & Prusti, T. 1993, A&A, 276, 129

Herbig, G. H. 1960, ApJS, 4, 337.

Herbst, W., & Shevchenko, V. S. 1999, AJ, 118, 1043

Hillenbrand, L. A. 1992, Ph.D. thesis, University of Massachusetts, Amherst, USA

Hillenbrand, L. A., Meyer, M. R., Strom, S. E. & Skrutskie, M. F. 1995, AJ, 109, 280

Hillenbrand, L. A., Strom, S. E., Vrba, F. J. & Keene, J. 1992, ApJ, 397, 613

Hu, J. Y., Blondel, P. F. C., The, P. S., Tjin A Djie, H. R. E., de Winter, D., Catala, C. & Talavera, A. 1991, A&A, 248, 150

Hubble, E. 1922, ApJ, 56, 162

Hughes, J. D., Emerson, J. P., Zinnecker, H. & Whitelock, P. A. 1989, MNRAS, 236, 117

Hughes, J. D., Hartigan, P., Graham, J. A., Emerson, J. P. & Marang, F. 1991, AJ, 101, 1013

Hunter, D. A. & Massey, P. 1990, AJ, 99, 846

Hunter, D. A., Thronson, H. A & Wilton, C. 1990, AJ, 100, 1915

Hutsemekers, D. & van Drom, E. 1990, A&A, 238, 134

Ibragimov, M. A., Melnikov, S. Y., Chernyshov, A. V. & Shevchenko, V. S. 1988, Astrofizika, 29, 633

Ivezíc, Ž., & Elitzur, M. 2000, ApJ, 534, L93

Jayawardhana, R., Fisher, S., Hartmann, L., Telesco, C., Piña, R. and Fazio, G. 1998, ApJ, 503, L79

Johnson, H. L. 1964, Bol. Obs. Tonantzintla Tacubaya, 3, 305

Johnson, H. L. 1966, ARA&A, 4, 193

Jourdain de Muizon, M., d'Hendecourt, L. B. & Geballe, T. R. 1990, A&A, 227, 526

Kastner, J. H. & Weintraub, D. A. 1996, ApJ, 466, L103

Kastner, J. H., Weintraub, D. A. & Aspin, C. 1992, ApJ, 389, 357

Kastner, J. H., Weintraub, D. A., Snell, R. L., Sandell, G., Aspin, C., Hughes, D. H. & Baas, F. 1994, ApJ, 425, 695

Kenyon, S. J. 1999, in The Origin of Stars and Planetary Systems, ed. C. J. Lada & N. D. Kylafis (Dordrecht:Kluwer), 613

Kenyon, S. J. & Hartmann, L. 1987, ApJ, 323, 714

Kenyon, S. J., Hartmann, L., Gomez, M., Carr, J. S. & Tokunaga, A. 1993, AJ, 105, 1505

Knacke, R. F., Farjado-Acosta, S. B., Telesco, C. M., Hackwell, J. A., Lynch. D. K., & Russell, R. W. 1993, ApJ, 418, 440

Knee, L. B. G. 1992, A&A, 259, 283

Kutner, M. L., Machnik, D. E., Tucker, K. D. & Dickman, R. L. 1980, ApJ, 237, 73

Lada, C. J. 1987,in Star Forming Regions, Proceedings of the 115th Symposium of the International Astronomical Union, ed M. Peimbert, & J. Jugaku (Dordrecht:Kluwer), 1

Lada, C. J., & Adams, F. C. 1992, ApJ, 393, 278

Lagage, P. O., Olofsson, G., Cabrit, S., Cesarsky, C. J., Nordh, L. & Rodriguez Espinosa, J. M. 1993, ApJ, 417, L79

Laor, A., & Draine, B. T. 1993, ApJ, 402, 441

Lebofsky, M. J. & Kleinmann, S. G. 1976, AJ, 81, 534

Léger, A & Peget, J. L. 1984, A&A, 137, L5

Leinert, C., Haas, M. & Lenzen, R. 1991, A&A, 246, 180

Leinert, C., Richichi, A., & Haas, M. 1997, A&A, 318, 472

Leinert, C., Zinnecker, H., Weitzel, N., Christou, J., Ridgway, S. T., Jameson, R., Haas, M. & Lenzen, R. 1993, A&A, 278, 129

Léna, P. 1988, Observational Astrophysics, ed. M. Harwit, R. Kippenhahn, J. Zahn (NY: Springer-Verlag)

Li, W., Evans, N. J., Harvey, P. M. & Colomé, C. 1994, ApJ, 433, 199

Lorenzetti, D., Nisini, B., Berrili, F. & Strafella, F. 1994, in ASP Conf. Ser. Vol. 62, The Nature and evolutionary Status of Herbig Ae/Be Stars, ed. P. S. Thé, M. R. Pérez, & P. J. van den Heuvel (San Francisco: ASP), 189

Lynch, D. K. & Mazuk, S. 2000, in ASP Conf. Ser. 196, Thermal Emission Spectroscopy and Analysis of Dust, Disks, and Regoliths, eds. M. Sitko, A. Sprague, D. Lynch, 127

Malfait, K., Bogaert, E., & Waelkens, C. 1998, A&A, 331, 211

Malfait, K., Waelkens, C., Waters, L. B. F. M., Vandenbussche, B., Huygen, E. & de Graauw, M. S. 1998, A&A, 332, L25

Mannings, V. & Emerson, J. P. 1994, MNRAS, 267, 361

Mannings, V., Koerner & Sargent, A. I. 1997, Nature, 388, 555

Mannings, V., & Sargent, A. I. 1997, ApJ, 490, 792

Mannings, V., & Sargent, A. I. 2000, ApJ, 529, 391

Marcy, G. W., & Butler, R. P. 2000, PASP, 112, 137

Margulis, M., Lada, C. J. & Young, E. T. 1989, ApJ, 345, 906

Marsh, K. A., van Cleve, J. E., Mahoney, M. J., Hayward, T. L. & Houck, J. R. 1995, ApJ, 451, 777

Martín, E. L. 1994, in ASP Conf. Ser. Vol. 62, The Nature and Evolutionary Status of Herbig Ae/Be Stars, ed. P. S. Thé, M. R. Pérez, & P. J. van den Heuvel (San Francisco: ASP), 315

Massey, P., & Davis, L. E., 1992, "Users Guide to Stellar CCD Photometry with IRAF", IRAF Users Manual, NOAO, *http://iraf.noao.edu/iraf/web/docs/photom.html*

Mathis, J. S. 1990, ARA&A, 28, 37

Mathis, J. S., Rumpl, W., & Nordsiek, K. H. 1977, ApJ, 217, 425

McCaughrean, M. & O'Dell, C. 1996, AJ, 111, 1977

Melnikov, S.Y. & Ezhkova, O. V. 2000, Astronomy Letters, 26, 233

Mendoza, V. 1966, ApJ, 143, 1010

Merrill, P. W. 1913, PASP, 25, 118

Merrill, P. W. & Burwell, C. G. 1933, ApJ, 78, 87

Merrill, P. W. & Burwell, C. G. 1950, ApJ, 112, 72

Millan-Gabet, R. 1999, Ph.D. thesis, University of Massachusetts Amherst, USA

Millan-Gabet, R., Schloerb, F. P., Traub, W. A., Malbet, F., Berger, J. P. & Bregman, J. D. 1999, ApJ, 513, L131

Miller, W. C. & Merrill, P. W. 1951, ApJ, 113, 624

Mitchell, G. & Matthews, H. 1994, ApJ, 423, L55

Mookerjea, B., Ghosh, S. K., Karnik, A. D., Rengarajan, T. N., Tandon, S. N. & Verma, R. P. 1999, ApJ, 522, 285

Mouillet, D., Lagrange, A., Beuzit, J. & Renaud, N. 1997, A&A, 324, 1083

Natta, A., Grinin, V. P., Mannings, V. & Ungerechts, H. 1997, ApJ, 491, 885

Natta, A. & Krügel, E. 1995, A&A, 302, 849

Natta, A., Palla, F., Butner, H. M., Evans, N. J. & Harvey, P. M. 1993a, ApJ, 406, 674

Natta, A., Palla, F., Butner, H. M., Evans, N. J. & Harvey, P. M. 1992, ApJ, 391, 805

Natta, A., Prusti, T. & Krügel, E. 1993b, A&A, 275, 527

Neugebauer, G., & Habing, H. J., van Duinen, R., Aumann, H. H., & Baud, B. 1984, ApJ, 278, L1

Osterloh, M. & Beckwith, S. V. W. 1995, ApJ, 439, 288

Palla, F. 1993, in Infrared Astronomy, IV Canary Islands Winter School of Astrophysics, ed. A. Mampaso, M. Prieto, & F. Sánchez (Cambridge: Cambridge Univ. Press), 3

Palla, F. 1999, in The Origin of Stars and Planetary Systems, ed. C. J. Lada & N. D. Kylafis (Dordrecht:Kluwer), 375

Palla, F. & Prusti, T. 1993, A&A, 272, 249

Palla, F. & Stahler, S. W. 1993, ApJ, 418, 414

Palla, F. & Stahler, S. W. 1999, ApJ, 525, 772

Palla, F., Testi, L., Hunter, T. R., Taylor, G. B., Prusti, T., Felli, M., Natta, A. & Stanga, R. M. 1995, A&A, 293, 521

Pantin, E., Waelkens, C., & Lagage, P. O. 2000, A&A, 362, L9

Pégourié, B. & Papoular, R. 1985, A&A, 142, 451

Perryman, M. A. C., Lindegren, L. Kovalevsky, J. Hoeg, E. Bastian, U. Bernacca, P. L. Crz, M. Donati, F. Grenon, M. van Leeuwen, F. van der Marel, H. Mignard, F. Murray, C. A. Le Poole, R. S. Schrijver, H. Turon, C. Arenou, F. Froeschlé, M. Petersen, C. S., 1997, A&A, 323, L49

Persi, P., Ferrari-Toniolo, M., Busso, M., Robberto, M., Scaltriti, F. & Silvestro, G. 1988, AJ, 95, 1167

Pezzuto, S., Strafella, F. & Lorenzetti, D. 1997, ApJ, 485, 290

Pirzkal, N., Spillar, E. J. and Dyck, H. M. 1997, ApJ, 481, 392

Polomski, E., Telesco, C., & Piña, R. 2000, in ASP Conf. Ser. Disks , Planetesimals, and Planets, ed. F. Garzon, C. Eiroa, D. de Winter, & T. J. Mahoney in press

Prusti, T., Natta, A., & Palla, F. 1994, A&A, 292, 593

Puetter, R. C. & Yahil, A. 1999, ASP Conf. Ser. 172 Astronomical Data Analysis Software and Systems VIII, ed. D. Mehringer, R. Plante, & D. Roberts, (San Francisco: ASP), 307

Puget, J. L., & Léger, A. 1989, ARA&A, 27, 161

Ray, T. P., Poetzel, R., Solf, J. & Mundt, R. 1990, ApJ, 357, L45

Rieke, G. H. 1994, in Detection of Light: from the Ultraviolet to the Submillimeter (NY:Cambridge University Press)

Rieke, G. H. & Lebofsky, M. J. 1985, ApJ, 288, 618

Riemann, H.-G., Gürtler, J., Friedemann, C., & Käufl, H. U. 1997, A&A, 326, 271

Rodriguez, L. F., Haschick, A. D., Torrelles, J. M., & Myers, P. C. 1987, A&A, 186, 319

Röser, S. & Bastian, U. 1988, A&AS, 74, 449

Rydgren, A. E. & Vrba, F. J. 1987, PASP, 99, 482

Sargent, A. I. 1994, in Disks & Outflows Around Young Stars, ed. S. Beckwith, J. Staude, A. Quetz, & A. Natta (Dordrecht:Kluwer), 1

Schroeder, D. J., 1987, in Astronomical Optics, (San Diego: Academic Press)

Schwarzschild, M. 1958, Structure and Evolution of the Stars (Princeton:Princeton University Press)

Shakura, N. I., & Sunyaev, R. A. 1973, A&A, 24, 337

Sharpless. S. 1959, ApJS, 4, 257

Shevchenko, V. S., Grankin, K. N., Ibragimov, M. A., Melnikov, S. Yu., Yakubov, S. D. 1993, A&SS 202, 121

Shevchenko, V., Grankin, K., Ibragimov, M. 1994, in ASP Conf. Ser. Vol. 62, The Nature and evolutionary Status of Herbig Ae/Be Stars, ed. P. S. Thé, M. R. Pérez, & P. J. van den Heuvel (San Francisco: ASP), 43

Shu, F. H., Allen, A., Shang, H., Ostriker, E. C., & Li, Z. 1999, in The Origin of Stars and Planetary Systems, ed. C. J. Lada & N. D. Kylafis (Dordrecht:Kluwer), 193

Sitko, M. L., Simon, T. & Meade, M. R. 1984, PASP, 96, 54

Sitko, M. L., Grady, C. A., Lynch, D. K., Russell, R. W. & Hanner, M. S. 1999, ApJ, 510, 408

Skinner, S. L., Brown, A. & Stewart, R. T. 1993, ApJS, 87, 217

Skinner, S. L., & Yamauchi, S. 1996, ApJ, 471, 987

Slysh, V. I., Val'tts, I. E., Migenes, V., Fomalont, E., Hirabayashi, H., Inoue, M. & Umemoto, T. 1999, ApJ, 526, 236

Smith, B. A. & Terrile, R. J. 1984, Science, 226, 1421

Snell, R. L., Dickman, R. L. & Huang, Y. 1990, ApJ, 352, 139

Stahler, S. W., Shu, F. H., Tam, R. E. 1980, ApJ, 242, 226

Staude, H. J., & Elsässer, H. 1993, A&A Rev., 5, 165

Staude, H. J. & Neckel, T. 1991, A&A, 244, L13

Strom, K. M., Strom, S. E., Breger, M., Brooke, A. L., Yost, J., Grasdalen, G. & Carrasco, L. 1972, ApJ, 176, L93

Szymczak, M., Hrynek, G. & Kus, A. J. 2000, A&AS, 143, 269

Testi, L., Palla, F. & Natta, A. 1998, A&AS, 133, 81

Testi, L., Palla, F. & Natta, A. 1999, A&A, 342, 515

Thé, P. S., de Winter, D., & Pérez, M. R. 1994, A&AS, 104, 315

Thé, P. S., Tjin, H. R. E., Steenman, H. & Wesselius, P. R. 1986, A&A, 155, 347

Tout, C. A. & Pringle, J. E. 1995, MNRAS, 272, 528

Towne, D. H. 1967, Wave Phenomena, (NY: Dover Publications)

van den Ancker, M. E., Bouwman, J., Wesselius, P. R., Waters, L. B. F. M., Dougherty, S. M. and van Dishoeck, E. F. 2000a, A&A, 357, 325

van den Ancker, M. E., de Winter, D. & Tjin A Djie, H. R. E. 1998, A&A, 330, 145 van den Ancker, M. E., Wesselius, P. R. & Tielens, A. G. G. M. 2000b, A&A, 355, 194

van der Bliek, N. S., Manfroid, J. & Bouchet, P. 1996, A&AS, 119, 547

Van Kerckhoven, C., Hony, S. Peeters, E., Tielens, A. G. G. M. Allamandola, L. J., Hudgins, D. M., Cox, P. Roelfsema, P. R., Voors, R. H. M. Waelkens, C., Waters, L. B. F. M. & Wesselius, P. R 2000, A&A, 357, 1013

Volk, K. & Cohen, M. 1989, AJ, 98, 931

Walker, H. J. & Cohen, M. 1988, AJ, 95, 180

Walker, H. J., Cohen, M., Volk, K., Wainscoat, R. J., & Schwartz, D. E. 1989, AJ, 98, 2163

Waters, L.B. F. M., Cote, J. & Aumann, H. H. 1987, A&A, 172, 225

Waters, L. B. F. M. & Waelkens, C. 1998, ARA&A, 36, 233

Weaver, W. B. & Jones, G. 1992, ApJS, 78, 239

Weingartner, J. C., & Draine, B. T. 2000, ApJ, submitted

Weintraub, D. A. 1990, ApJS, 74, 575

Weintraub, D.A. & Kastner, J. 1993, ApJ, 411, 767

Weintraub, D. A., Kastner, J. H., Gatley, I. & Merrill, K. M. 1996, ApJ, 468, L45

Weintraub, D. A., Kastner, J. H. & Mahesh, A. 1994, ApJ, 420, L87

Weintraub, D. A., Sandell, G. & Duncan, W. D. 1991, ApJ, 382, 270

Whitelock, P., Feast, M. & Catchpole, R. 1991, MNRAS, 248, 276

Wilner, D. J. 1999, The Physics and Chemistry of the Interstellar Medium, Proceedings of the 3rd Cologne-Zermatt Symposium, held in Zermatt, September 22-25, 1998, Eds. V. Ossenkopf, J. Stutzki, and G. Winnewisser, (GCA-Verlag Herdecke)

Willner, S. P. & Gillett, F. C., Herter, T. L., Jones, B., & Krassner, J. 1982, ApJ, 253, 174

Wooden, D. H. 1994, in ASP Conf. Ser. Vol. 62, The Nature and evolutionary Status of Herbig Ae/Be Stars, ed. P. S. Thé, M. R. Pérez, & P. J. van den Heuvel (San Francisco: ASP), 138

Wouterloot, J. G. A., Brand, J. & Fiegle, K. 1993, A&AS, 98, 589

Yamashita, T., Sato, S., Nagata, T., Gatley, I., Hayashi, S. S. & Fukui, Y. 1989, ApJ, 336, 832

Yamauchi, S., Hamaguchi, K., Koyama, K. & Murakami, H. 1998, PASJ, 50, 465

Yang, J., Umemoto, T., Iwata, T. & Fukui, Y. 1991, ApJ, 373, 137

Yoshida, S., Kogure, T., Nakano, M., Tatematsu, K. & Wiramihardja, S. D. 1991, PASJ, 43, 363

Yoshida, S., Kogure, T., Nakano, M., Tatematsu, K. & Wiramihardja, S. D. 1992, PASJ, 44, 77

Zavagno, A., Cox, P., & Baluteau, J.-P. 1992, A&A, 259, 241

Zinnecker, H. & Preibisch, Th. 1994, A&A, 292, 152

BIOGRAPHICAL SKETCH

Elisha was born in the small fishing village of Scituate, Massachusetts in 1966. The beautiful, rugged coast, and dark skies of Scituate inspired a life-long interest in the natural sciences. At the age of 14 she first acquired a 2.5-inch telescope and began studying astronomy. Since that age it has been her goal to earn a PhD in astronomy. She graduated with a Bachelors degree in Astronomy from Wellesley College in 1988, and went on to work for several years at the University of California, Berkeley. Her work there involved research at several large observatories, including Lick, and Kitt Peak National Observatory, as well space-based research using the EUVE satellite and the HST. After being accepted to graduate studies at the University of Florida, she began working with Dr. Charles Telesco on the study of the environments of young stars. Her research involved lengthy travel to high-altitude observatories in the Andes and Hawai'i. She was later awarded a NASA GSRP for this research, as well as several small research awards and a Dissertation Fellowship from the University of Florida. After her PhD defense she will be working with Dr. Bob Gehrz at the University of Minnesota on a large project concerning SIRTF observations of stars.

I certify that I have read this study and that in my opinion it conforms to acceptable standards of scholarly presentation and is fully adequate, in scope and quality, as a dissertation for the degree of Doctor of Philosophy.

Charles M. Telesco

Charles M. Telesco, Chairman
Professor of Astronomy

I certify that I have read this study and that in my opinion it conforms to acceptable standards of scholarly presentation and is fully adequate, in scope and quality, as a dissertation for the degree of Doctor of Philosophy.

Elizabeth A Lada

Elizabeth A. Lada
Associate Professor of Astronomy

I certify that I have read this study and that in my opinion it conforms to acceptable standards of scholarly presentation and is fully adequate, in scope and quality, as a dissertation for the degree of Doctor of Philosophy.

Stanley F Dermott

Stanley F. Dermott
Professor of Astronomy

I certify that I have read this study and that in my opinion it conforms to acceptable standards of scholarly presentation and is fully adequate, in scope and quality, as a dissertation for the degree of Doctor of Philosophy.

Frederick Hamann

Dr. Fredrick Hamann
Associate Professor of Astronomy

I certify that I have read this study and that in my opinion it conforms to acceptable standards of scholarly presentation and is fully adequate, in scope and quality, as a dissertation for the degree of Doctor of Philosophy.

Martin T. Vala

Martin T. Vala
Professor of Chemistry

This dissertation was submitted to the Graduate Faculty of the Department of Astronomy in the College of Liberal Arts and Sciences and to the Graduate School and was accepted as partial fulfillment of the requirements for the degree of Doctor of Philosophy.

December 2000

Dean, Graduate School